ABSTRACT

Title of dissertation: SILICON AND POLYMER COMPONENTS FOR MICROROBOTS

Aaron Powers Gerratt
Doctor of Philosophy, 2013

Dissertation directed by: Professor Sarah Bergbreiter
Department of Mechanical Engineering

This dissertation presents the characterization and implementation of the first microfabrication process to incorporate high aspect ratio compliant polymer structures in-plane with traditional silicon microelectromechanical systems (MEMS). This discussion begins with *in situ* mechanical characterization of microscale polymer springs using silicon-on-insulator-MEMS (SOI-MEMS). The analysis compares microscale samples that were tested on-chip with macroscale samples tested using a dynamic mechanical analyzer. The results describe the effect of the processing steps on the polymer during fabrication and help to guide the design of mechanisms using polymers.

Characterization of the dielectric breakdown of polymer thin films with thicknesses from 2 to 14 μm between silicon electrodes was also performed. The results demonstrate that there is a strong dependence of the breakdown field on both the electrode gap and shape. The breakdown fields ranged from 250 V/μm to 635 V/μm,

depending on the electrode geometry and gap, approaching 10x the breakdown fields for air gaps of the same size.

These materials were then used to create compliant all-polymer thermal and electrostatic microactuators. All-polymer thermal actuators demonstrated displacements as large at 100 μm and forces as high as 55 μN. A 1 mm long electrostatic dielectric elastomer actuator demonstrated a tip displacement as high as 350 μm at 1.1 kV with a electrical power consumption of 11 μW. The actuators are fabricated with elastomeric materials, so they are very robust and can undergo large strains in both tension and bending and still operate once released.

Finally, the compliant polymer and silicon actuators were combined in an actuated bio-inspired system. Small insects and other animals use a multitude of materials to realize specific functions, including locomotion. By incorporating compliant elastomer structures in-plane with traditional silicon actuators, compact energy storage systems based on elastomer springs for small jumping robots were demonstrated. Results include a 4 mm x 4 mm jumping mechanism that has reached heights of 32 cm, 80x its own height, and an on-chip actuated mechanism that has been used to propel a 1.4 mg projectile over 7 cm.

SILICON AND POLYMER COMPONENTS FOR MICROROBOTS

by

Aaron Powers Gerratt

Dissertation submitted to the Faculty of the Graduate School of the
University of Maryland, College Park in partial fulfillment
of the requirements for the degree of
Doctor of Philosophy
2013

Advisory Committee:
Assistant Professor Sarah Bergbreiter, Chair/Advisor
Associate Professor Pamela Abshire
Professor Don DeVoe
Associate Professor Teng Li
Professor Elisabeth Smela

© Copyright by
Aaron Powers Gerratt
2013

Acknowledgments

There are many individuals who made this work possible and deserve thanks. First and foremost is my advisor, Professor Sarah Bergbreiter, whose guidance and inspiration were critical to the success of the work. I would like to thank my labmates Ivan Penskiy, Dana Vogtmann, Jessica Rajkowski, Mikeal Gateau, Chris Brown, and Wayne Churaman for constant feedback and constructive criticism. Ivan Penskiy was particularly helpful; he was always willing to listen to my ideas and point out their flaws and collaborated with me on several journal and conference publications.

I am in great debt to Professor Rob White at Tufts University who initially introduced me to the world of MEMS. His patience, guidance, and inspiration are what ultimately motivated me to apply to graduate school and focus on MEMS.

There are many professors and students at the University of Maryland who are quite deserving of thanks. I would like to thank Professor Smela and her students Bavani Balakrisnan, Justin Pearse, Timir Datta, and Mark Kujawski for their input related to processing with polymers. Bavani Balakrisnan deserves special recognition for her input while I was developing the dielectric elastomer actuators. I would like to thank Professor Peter Kofinas and his student Adam Behrens for both allowing me to use their dynamic mechanical analyzer and for helping me troubleshoot issues with it. I would like to thank Professor S. K. Gupta for allowing me to access his lab and use his laser cutter. I would like to thank Professor Don DeVoe and his student Jason Felder for the use of and help with their high voltage power supply and Isaac Misiri

for being a sounding board for new ideas to try in the cleanroom. There are also many undergraduate students I have worked with who deserve recognition including Mary Tellers, Ryan Etkins, and Ethan Schaler.

I would like to thank my dissertation committee for their input on my work, which included Professors Pamela Abshire, Donald DeVoe, Teng Li, and Elisabeth Smela.

Finally, I would like to thank the entire staff of the Maryland NanoCenter FabLab including Jim O'Connor, John Abrahms, Jon Hummel, Tom Loughran, and Mark Lecates. Their advice on processing and constant efforts to keep all of the equipment in the cleanroom up and running enabled me to finish this dissertation on time.

Table of Contents

List of Tables vii

List of Figures viii

1 Introduction 1
1.1 Microrobots . . . 2
1.2 Materials for Microrobots . . . 4
1.3 Organization of this Dissertation . . . 7

2 Fabrication with Silicon and Polymers 8
2.1 SOI Fabrication Process and Mechanical Characterization . . . 9
2.1.1 Introduction . . . 9
2.1.2 Fabrication . . . 12
2.1.2.1 Details of the Fabrication Process . . . 12
2.1.2.2 Results of the Fabrication Process . . . 13
2.1.2.3 Affect of the Fabrication Process on PDMS Dimensions 15
2.1.3 DMA and *In situ* Test Procedures . . . 19
2.1.3.1 DMA Test Procedure . . . 19
2.1.3.2 *In situ* Test Procedures . . . 20
2.1.3.2.1 Calibration . . . 23
2.1.3.2.2 *In situ* Stress and Strain . . . 26
2.1.3.2.3 Geometric Coefficient . . . 27
2.1.4 Results . . . 29
2.1.4.1 DMA Characterization . . . 29
2.1.4.2 *In situ* Characterization . . . 34
2.1.4.2.1 Long-term stability . . . 35
2.1.4.2.2 Test Results . . . 36
2.1.5 Discussion . . . 39
2.1.5.1 Comparison of the Macroscale and Microscale Samples 39
2.1.5.2 Implications for PDMS Processing in SOI-MEMS . . 41
2.1.6 Elastomer Adhesion, Ultimate Strain, and Hysteresis . . . 44
2.1.6.1 Silicon-Elastomer Adhesion . . . 44
2.1.6.2 Ultimate Strain Behavior of Processed Elastomer . . 47
2.1.6.3 Hysteresis in Processed Elastomer . . . 48
2.1.7 Conclusions . . . 48
2.2 Dielectric Breakdown of PDMS Thin Films . . . 50
2.2.1 Introduction . . . 50
2.2.2 Design and Fabrication of Test Structures . . . 51
2.2.2.1 Design of Test Structures . . . 52
2.2.2.2 Fabrication of Test Structures . . . 55

2.2.3 Test Procedure and Results . . . 57
2.2.3.1 Test Procedure . . . 57
2.2.3.2 Test Results . . . 57
2.2.4 Discussion . . . 61
2.2.5 Conclusions . . . 67
2.3 Conductive PDMS . . . 67
2.3.1 Carbon Black Filler Particles . . . 68
2.3.2 Characterization of PDMS/carbon . . . 70
2.4 Conclusions . . . 74

3 All-Polymer Actuators 76
3.1 Fabrication . . . 76
3.1.1 Fabrication Process . . . 77
3.1.2 Fabrication Results . . . 80
3.2 All-Polymer Thermal Actuators . . . 83
3.2.1 Thermal Actuator Design . . . 84
3.2.2 Experimental Results . . . 86
3.2.2.1 Thermal Actuator Performance . . . 89
3.2.2.2 Frequency Response . . . 91
3.2.2.3 Robustness . . . 91
3.3 All-Polymer Electrostatic Actuators . . . 92
3.3.1 Analysis of Dielectric Elastomer Actuators . . . 96
3.3.2 Design . . . 101
3.3.3 Actuation Results . . . 105
3.4 Conclusions . . . 112

4 Incorporating Silicone for Jumping Locomotion in Microrobots 113
4.1 Introduction . . . 113
4.2 Jumping Robots . . . 116
4.2.1 Scaling . . . 117
4.2.2 Actuation . . . 120
4.3 Jumping Mechanism . . . 122
4.3.1 Fabrication Process . . . 123
4.3.2 Results . . . 126
4.4 Combining Actuation and Elastomer Mechanisms . . . 129
4.4.1 Actuated Mechanism . . . 130
4.4.2 Results . . . 135
4.5 Discussion . . . 138
4.5.1 Comparison of the two Systems . . . 140
4.6 Conclusions . . . 141

5 Conclusions, Contributions, and Future Work 142
5.1 Conclusions and Contributions 142
5.2 Future Work 147

A Details of the Fabrication Process 150

B Data from the Calibration of the Microscale Devices 156

C MATLAB Code for Image Processing 158

D ANSYS Code 161

Bibliography 164

List of Tables

2.1 Nonlinear coefficient and calculated Young's moduli for macroscale samples. 34
2.2 Nonlinear coefficient and calculated Young's moduli for microscale samples. 38
3.1 Calculation of the material properties used in the FEA analysis . . . 109
A.1 Details of the fabrication process 151

List of Figures

2.1 Cross-section and projection views of the microfabrication process. . . 14
2.2 Trenches etched in silicon that have been refilled with Sylgard 184. . 15
2.3 SEM image of a silicon and elastomer feature. 16
2.4 A schematic showing a cross-section of the wafer during fabrication. . 18
2.5 SEM image of a fabricated test mechanism. 21
2.6 SEM image of a fabricated test mechanism. 22
2.7 FEA model of the DMA test samples. 28
2.8 Stress-strain results for the macroscale PDMS samples cured for 2 hours at 70 °C, 90 °C, and 120 °C. 30
2.9 Stress-strain results for eighteen macroscale PDMS samples from four mixtures cured for 2 hours at 120 °C. 30
2.10 Stress-strain curves for the elongation of the macroscale samples. . . . 34
2.11 Results representing 1,000 strain cycles on microscale samples. 36
2.12 Stress-strain curves for the microscale PDMS samples released for 5 and 8 hours. 37
2.13 Stress-strain curves showing the elongation of the microscale PDMS samples released for 5 hours. 38
2.14 Stress-strain curves showing the elongation of the microscale PDMS samples released for 8 hours. 38
2.15 Stress-strain curves showing the average data for the elongation of the microscale and macroscale PDMS samples. 42
2.16 SEM of the test structure used to measure normal adhesion. 46
2.17 SEM of the test structure used to measure strain characteristics. . . . 46
2.18 Stress-strain curves for Sylgard 184. 46
2.19 Hysteresis curves for Sylgard 184. 49
2.20 Schematic showing cross sections of the fabrication process and the three types of test structures. 53
2.21 SEM images showing the five different electrode styles with 20 μm electrode gaps. 55
2.22 Images of the test structures before and after breakdown. 58
2.23 A voltage versus current curve from a test of an A1 test structure with an 8 μm air gap. 58
2.24 Breakdown of the Type A and B test structures. 60
2.25 Breakdown of the Type C test structures. 61
2.26 SEM image of a series of trenches etched in a silicon wafer showing the scalloping resulting from the DRIE process. 62
2.27 SEM image of scalloping in silicon after a DRIE process. 63
2.28 Change in the breakdown field with respect to air. 66
2.29 Conductivity of the PDMS/carbon as a function of weight percentage of carbon black. 71

2.30 Resistance as a function of time during relaxation for a PDMS/carbon sample. 73
2.31 Stress-strain curves for three types of MRTV-9 samples. 75

3.1 20 µm PDMS and conductive-PDMS features fabricated together in-plane. 77
3.2 Perspective and cross section views of the microfabrication process. 79
3.3 PDMS films with silver and carbon black filler particles. 82
3.4 SEM of chevron heatuator and bilayer thermal actuators. 86
3.5 Schematic of the force-displacement characterization setup. 87
3.6 Overlaid images of hot and cold *(A)* heatuator actuators *(B)* chevron actuators *(C)* bilayer actuator. 88
3.7 Displacement as a function of input power. 90
3.8 Force as a function of input power. 90
3.9 Frequency response of the displacement amplitude during actuation. 92
3.10 A chevron-type actuator in three states. 92
3.11 A microfabricated bidirectional DEA with alternating conductive and dielectric layers. 95
3.12 A DEA without and with a voltage applied. 95
3.13 Schematic showing how applied voltages lead to bidirectional actuation. 104
3.14 The tip of a fabricated DEA with 30 µm traces. 105
3.15 Image of unidirectional displacement of a DEA. 106
3.16 Image of bidirectional displacement of a DEA. 106
3.17 The voltage-displacement curve that corresponds with Figure 3.15. 109

4.1 A schematic of the three phases of the jumping process. 122
4.2 Cross-section and perspective views of the DSP-based fabrication process. 124
4.3 A SEM image of the jumping mechanism. 127
4.4 Screenshots from a video showing the takeoff of the jumping mechanism. 128
4.5 A colored SEM image of the actuated mechanism. 130
4.6 A SEM image of a thermal actuator. 132
4.7 Closeup on the area down in the red box on Figure 4.5. 132
4.8 Image of a fully wirebonded actuated mechanism. 135
4.9 Two images of the system before and after the actuators were sequenced. 136
4.10 A schematic of the test setup. 137

A.1 SEM of the cross section of trenches etched in a silicon wafer demonstrating the trench profile. 154
A.2 SEM of the cross section of trenches etched in a silicon wafer demonstrating the ARDE. 155

B.1 Plot of the calibration data used to determine the capacitance as a function of displacement. 157

B.2 Plot of the calibration data used to determine the flexure spring constant. 157

Chapter 1

Introduction

There have been several seminal papers in the area of microelectronics that have inspired broad areas of research leading to microrobots. Richard Feynman's 1959 "There's Plenty of Room at the Bottom" challenged scientists to investigate miniaturization of motors and reduce the minimum size of features that could be patterned [1]. This came around the same time that the first integrated circuit was demonstrated by Jack Kilby in 1958 and patented in 1959 [2]. Kurt Petersen's 1982 paper "Silicon as a Mechanical Material" helped to define microelectromechanical systems (MEMS) as an active research field [3]. Anita Flynn's 1987 paper "Gnat Robots (and how they will change robotics)" spurred an interest into microrobotics as a research area [4]. Flynn's paper describes how advances in integrated circuits, computer algorithms, and microfabrication have led to visions of a world where tiny robots supplement the everyday lives of humans. While it has been 25 years and such a premonition has not yet come true, such a vision still inspires and motivates.

A brief search of papers on microrobots demonstrates the large range of devices that have been called microrobots. These range from large, centimeter scale robots with integrated power, control, and sensing [5, 6] to small, micrometer or sub-micrometer scale structures which require off-board power and sensing [7, 8, 9, 10].

At both scales there is ongoing work looking at controlling biological organisms, with single bacteria [11, 12] and large moths and cockroaches [13, 14] at two extremes. For the purposes of this dissertation, a microrobot will be defined as a mobile device that has micron-scale features but that is millimeters in size. Additionally, this work does not consider the field of microrobotics which looks at using macroscale robotics to interface with microscale components such as manipulators, though much of the work that will be presented could arguably be applied to that type of microrobotics as well.

The purpose of this dissertation is to bring the current state-of-the-art one step closer to the goal of robust, autonomous, and effective microrobots. There are many different approaches that one can take toward achieving this goal, and determining the appropriate path depends on the intended application. This dissertation approaches the task of creating microrobots by exploring the possibilities that integrating silicon and polymer components allows, while at the same time justifying this approach. It is also important to realize that all of the research completed during the various phases of this dissertation are applied to the more specific field of microrobotics but also contribute to the MEMS field in a general sense.

1.1 Microrobots

One of the most well-known microrobots is the Harvard RoboBee, though it is admittedly on the larger end of the size spectrum of microrobots with a wingspan

of 3 cm (though the other dimensions are considerably smaller) [15]. The manner in which the research on this robot is being executed exemplifies all of the challenges involved in the development of microrobots from the fabrication to control and actuation. There is a large team of scientists and engineering involved in the project, each with their own tasks and goals. Each aspect of the research, be it related to power, actuation, mechanisms, controlling, or sensing for the system, can be considered independently of the others, but without considering each of these ideas in the broader context of the microrobot, the project will not ultimately succeed. This dissertation only discusses the topics of fabrication, actuation, and mechanism design, but will address each of these topics in the context of the entire system.

There are a variety of mobility methods that have been examined for microrobots. Previous works include walking robots [16, 17], flying robots [15, 18], and crawling robots [19]. As the number of different mobility methods and mechanism complexity increases, microfabrication techniques have also had to evolve and be developed to support the complex requirements of these microrobots. Ebefors demonstrated polyimide thermal actuators as part of one of the first millimeter-scale walking microrobots [16]. Hollar's 10 mg silicon microrobot was built using traditional silicon microelectromechanical systems (MEMS) processing to include thick structural layers for high force actuators and thin polysilicon for multi-degree of freedom hinges in robot legs [17]. Wood developed the Smart Composite Microstructures (SCM) process by combining laser micromachined carbon fiber and polymer films to build

millimeter sized compliant mechanisms for a 60 mg robotic insect [20]. To create thin, compliant wings for micro air vehicles, Tanaka combined silicon deep reactive ion etching for mold building with parylene and polyurethane [18].

One of the common themes among all of these approaches is the use of unconventional materials in customized fabrication processes, be it the carbon fiber in the SCM process, the polyimide in the Ebefors process, or parylene and polyurethane in the Tanaka process. This dissertation focuses on the integration of silicone polymer materials into MEMS. These materials are common in microfluidics but are still not commonly used in silicon fabrication for mechanical features.

1.2 Materials for Microrobots

Semiconductors, dielectrics and metals are traditional materials used in the fabrication of MEMS [3]. MEMS processes provide for small feature sizes, batch processing and good integration with microactuators. While these materials and processes have proven to be extremely successful in devices such as inertial sensors [21], inkjet printer heads [22] and micromirrors for display systems [23], they are not well-suited for all MEMS devices including those that require compliant elastic materials [24]. Polymer materials such as polyimide [16, 25], parylene [26] and SU-8 [27] have been integrated with MEMS devices in an attempt to fill the void left by traditional materials. These polymers are attractive because of their mechanical properties, particularly a lower Young's modulus (around 2-4 GPa for polyimide [25],

parylene [26] and SU-8 [27] as opposed to 130-188 GPa for silicon [28]) and increased elasticity. Parylene is deposited with a conformal chemical vapor deposition process that allows for thin, high aspect ratio films. Suzuki demonstrated a low-frequency accelerometer based on parylene springs with a process that achieved spring constants as low as 26.1 mN/m [26]. SU-8 is commonly used because it is photopatternable in a wide range of film thicknesses (<1 μm to >1 mm), but it requires carefully controlled pre- and post-exposure bakes and has large residual stresses [29].

The library of materials available for MEMS processing also includes two-part polymers and room temperature vulcanizing rubbers. These materials are attractive for use in MEMS devices because they have a low Young's modulus, some less than 1 MPa [24] and can achieve maximum recoverable strains as high as 1000% [30]. The most prevalent example of these materials is poly(dimethylsiloxane) (PDMS), which is used widely in microfluidics and imprint lithography [31]. PDMS is not widely accepted as a mechanical material in MEMS devices, mainly because integration with semiconductor processing can be difficult. Lotters used PDMS as a mechanical material to demonstrate triaxial accelerometers using a patchwork process that required manual assembly of each sensor, resulting in variations in the acceleration sensitivity [32]. Tung demonstrated a complex multi-wafer fabrication process that integrated PDMS with comb drive actuators in a silicon-on-insulator device that could achieve multi-axis out-of-plane motion [33].

Work by Bergbreiter manually integrated PDMS into MEMS processes [34].

The PDMS that was used, Sylgard 186, had a Young's modulus on the order of a single MPa and was demonstrated for use in an energy storage and quick-release mechanism for a jumping microrobot. These devices, however, required separate fabrication and assembly of the silicon and elastomer components, which decreased the device yield, could only be used to fabricate relatively large features in the elastomer (approximately 100 μm), and decreased the fabrication time but increased the post-processing assembly time outside of the cleanroom.

This dissertation examines the integration of PDMS into batch silicon microfabrication and focuses on the integration of PDMS and silicon mechanical components for microrobots. This is done by first discussing how these two materials can actually be combined in a batch semiconductor fabrication process. The details of the fabrication are included as well as a detailed analysis of how all of the steps of the fabrication process effect the material properties of the post-processed polymer. Since the devices which will be discussed later are electromechanical devices, the dielectric breakdown of the polymer is discussed at the micron scale. Conductive polymers can are also manufactured by adding conductive filler particles, which is also discussed and characterized. These materials and the fabrication process are then implemented to demonstrate actuators and mechanisms for microrobots.

1.3 Organization of this Dissertation

This dissertation is divided into three major themes: fabrication and characterization, actuators, and actuated mechanisms. The discussion begins with Chapter 2 detailing the fabrication process used throughout the work as well as mechanical and electrical characterization of the polymer. This is followed by Chapter 3 on thermal and electrostatic all-polymer actuators. The characterization is followed by Chapter 4 detailing mechanical components for microrobots. Finally, conclusions are included in Chapter 5.

Chapter 2

Fabrication with Silicon and Polymers

The introduction to this dissertation described some of the potential for using compliant materials such as PDMS for microrobots. Before any new materials can be fully integrated into an electromechanical system, however, they must first be fully understood and characterized. This chapter describes the fabrication process that was implemented throughout this dissertation as well as the mechanical and electrical characterization of the polymers used throughout this dissertation. Section 2.1 of this chapter is based on the publication "*In situ* characterization of PDMS in SOI-MEMS" from volume 24, issue 4 of the Journal of Micromechanics and Microengineering by A. P. Gerratt, I. Penskiy, and S. Bergbreiter, published in 2013. Section 2.1.6 is based on the publication "SOI/Elastomer process for energy storage and rapid release" from volume 20, issue 10 of the Journal of Micromechanics and Microengineering by A. P. Gerratt, I. Penskiy, and S. Bergbreiter, published in 2010. Section 2.2 is based on the publication "Dielectric breakdown of PDMS thin films" in the Journal or Micromechanics and Microengineering by A. P. Gerratt and S. Bergbreiter, published in 2013. Section 2.3 is based on parts of the publication "Microfabrication of compliant all-polymer MEMS thermal actuators" from volume 122 of Sensors and Actuators A: Physical, pages 16 - 22, by A. P. Gerratt and S. Berg-

breiter, published in 2012. All of the work presented in this chapter was completed by Aaron Gerratt with the exception of the design of the electrostatic characterization device in Section 2.1.3.2. The design of this device was based on a device created by co-author Ivan Penskiy and was adapted by Aaron Gerratt for the requirements of this work.

2.1 SOI Fabrication Process and Mechanical Characterization

2.1.1 Introduction

Microelectromechanical systems (MEMS) are traditionally manufactured using materials with moduli on the order of 10s to 100s of GPa such as silicon, oxides, and metals by employing semiconductor microfabrication processes [3]. Recently, however, there has been an increase in research into non-silicon based MEMS, including polymer MEMS [35]. Stiff polymers with moduli on the order of 1 GPa, including parylene and polyimide, have been generally accepted in silicon processing, mainly as flexible substrates and coating or isolation layers [26, 36, 37, 38, 39]. Compliant polymers with moduli on the order of 1 MPa, such as poly(dimethylsiloxane) (PDMS) [40, 41], are enabling the development of microfluidics as they allow for simple and rapid prototyping with soft lithography [42, 43]. There has been some work on integrating PDMS into a silicon chip as a mechanical material [30, 32, 33, 44, 45], but little work has been done on the *in situ* characterization of PDMS.

There are many papers which have reported stress-strain data for PDMS at sizes

approaching the microscale. These works, however, typically characterized millimeter and centimeter scale PDMS thin films by using atomic force microscopy [46] or nanoindentation [47, 48, 49, 50] to apply small strains. Other works used highly sensitive macroscale transducers to measure the applied forces while monitoring strains [51, 52, 53]. Some previous work has looked at characterization by using differential pressure to deform PDMS membranes [54, 55]. The most relevant previous work demonstrated *in situ* dynamic mechanical characterization of PDMS samples at strains up to 14% using a multi-wafer fabrication process to transfer molded PDMS from a silicon wafer to an SOI wafer [56]. Strain in the PDMS was measured indirectly by monitoring the change in diffraction due to a grating patterned on the top of the PDMS sample to infer the strain. These solutions are useful, but either do not truly represent microscale sample sizes or do not account for all of the processing steps that materials are exposed to during an on-chip fabrication run. Additionally, most of these solutions do not capture the non-linear behavior of PDMS at large strains. The goal of this work is to demonstrate *in situ* mechanical characterization of PDMS at strains up to 65% using a test mechanism microfabricated with a silicon-on-insulator (SOI) based fabrication process. The results of this section are important for the design of MEMS which include PDMS as a mechanical material.

This discussion also provides a direct comparison of microscale and macroscale PDMS samples by fitting the results of the tests to linear and non-linear material models. This allows for analysis of the effect of the microfabrication processing steps,

which included exposure to various chemicals and plasmas, on the mechanical behavior of the PDMS. Previous work looked at the effect of different chemical treatments common in microfabrication on the qualitative survival of PDMS for microsystems, but did not examine the effect on mechanical properties [40]. In this work, the macroscale samples will be used to examine the influence of the curing temperature on the stiffness of PDMS and the microscale samples will be used to examine the influence of the release step in buffered hydrofluoric acid on the stiffness of the PDMS. These steps are of particular interest because of their strong potential to dramatically affect the mechanical properties of PDMS.

This fabrication process has been used to integrate PDMS and silicon for energy storage [44, 24] and to quantify the friction between PDMS thin films and silicon [45]. None of these works performed calibrated *in situ* characterization of the stress-strain behavior of PDMS in SOI-MEMS, which is the focus of this section. These calibrated measurements are necessary for designing MEMS devices which include mechanical features fabricated with PDMS [32, 44, 55, 57, 58].

This discussion begins with a description of the fabrication process in Section 2.1.2. The test setup and procedures are described in Section 2.1.3 with results shown in Section 2.1.4. A discussion of the results is presented in Section 2.1.5. Additional characterization of the elastomer adhesion, ultimate strain, and hysteresis is presented in Section 2.1.6. Finally, conclusions and future work are presented in Section 2.1.7.

2.1.2 Fabrication

The (100) SOI wafers used in the process were 100 mm in diameter with a handle layer thickness of 300 μm, a buried oxide (BOX) layer thickness of 4 μm, and a device layer thickness of 20 μm. The device and handle layers were boron doped to resistivities of 0.001-0.005 Ω-cm and 1-20 Ω-cm, respectively. Complete details of the fabrication process can be found in Appendix A, including tool parameters that were used during the fabrication.

2.1.2.1 Details of the Fabrication Process

The microfabrication began with a deep reactive ion etch (DRIE) down to the BOX using a silicon dioxide hard mask deposited at 300 °C in a plasma-enhanced chemical vapor deposition (PECVD) tool, shown in Step 2. The trenches created by the DRIE were then refilled with PDMS, which was cured at 90 °C for 2 hours, shown in Step 3. The excess cured polymer was removed from the wafer leaving a smooth surface, shown in Step 4. A 60 second rinse in a 3:1 solution of n-methylpyrrlidone (NMP) and tetrabutylammonium fluoride (TBAF) was used to remove any residual PDMS particles from the surface of the wafer [59]. A 2 minute soak in 6:1 buffered hydrofluoric acid (BHF) was used to remove the silicon dioxide hard mask.

A second DRIE was performed on the device layer down to the BOX using a 150 °C PECVD silicon dioxide hard mask. This DRIE patterned the silicon around

the previously patterned PDMS features, shown in Step 5. The next step was a DRIE on the handle layer of the wafer down to the BOX using a thick photoresist etch mask, shown in Step 6. The final step was a timed wet etch of the BOX with 18:1 BHF to release the silicon structures followed by a 1 hour soak in 2-propanol, shown in Step 7. Prior to testing, aluminum wedge bonds were added to silicon contact pads to provide a better electrical contact for the tungsten probes used to interface between the silicon chip and the external power supply.

The PDMS characterized in this section was Sylgard 184 from Dow Corning with a base to curing agent mass ratio of 10:1. Sylgard 184 is the focus of this section because it is the most commonly used silicone in MEMS [42, 51]. This process can be used with other silicones, provided they can withstand the processing. The silicones MRTV-9 from Insulcast, Dragon Skin from Smooth-On, and Sylgard 186 from Dow Corning have also been successfully fabricated with the process.

2.1.2.2 Results of the Fabrication Process

The viscosities of Sylgard 184 and Sylgard 186 are 4,575 centipoise and 66,700 centipoise [60], respectively, and both have been refilled in trenches with aspect ratios in excess of 20:1, as shown in Figure 2.2. The highly conformal refill is shown in Figure 2.3 which shows the presence of scallops in both the silicon and PDMS features. The scallops in the PDMS features, however, are actually the negative of the scallops in the silicon, a by-product of the silicon etch process described in more detail in Section

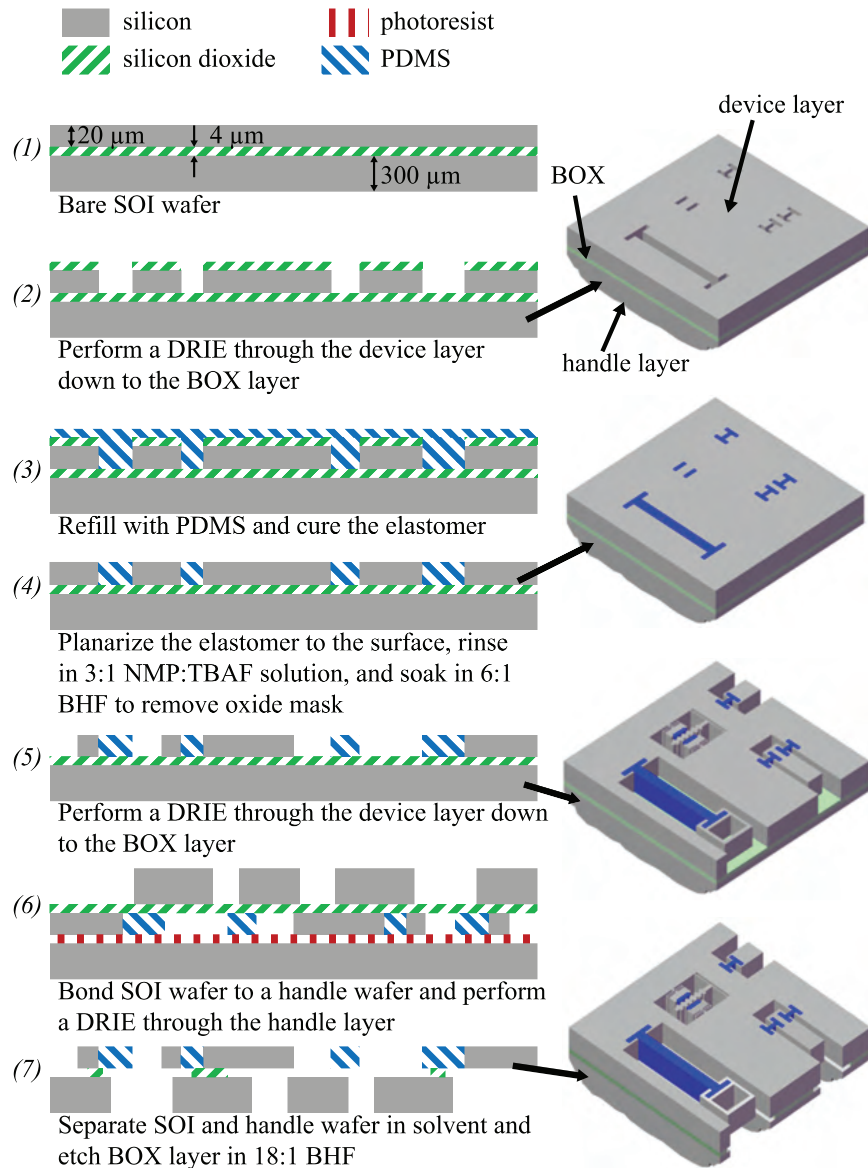

Figure 2.1: Cross-section and projection views of the microfabrication process.

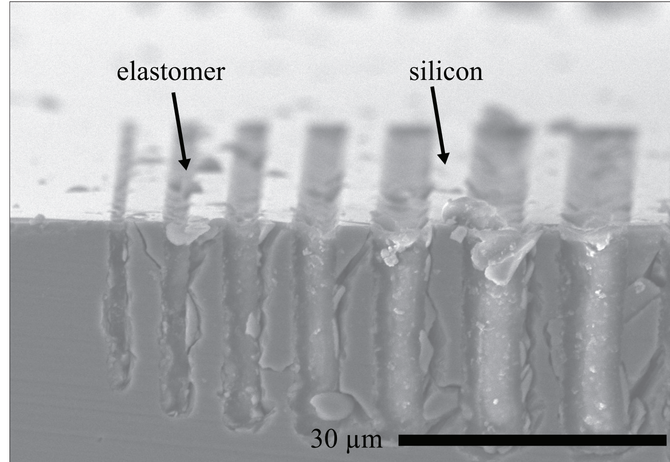

Figure 2.2: Trenches etched in silicon that have been refilled with Sylgard 184.

2.2.4 that was present when the PDMS was poured over the wafer. The PDMS was then cured and the silicon etched away, exposing the scalloped PDMS features. Features from 2 μm to hundreds of micrometers in width have been fabricated at lengths up to several millimeters. The yield for elastomer features less than about 30 μm in width was near 100%. This yield was consistent for features that were fabricated on many different SOI wafers. As the width of the features increased above 30 μm, the yield decreased. Any variations in the surface topography around the elastomer features resulted in a local thinning of the photoresist, especially for wider features where the difference in height was generally more pronounced.

2.1.2.3 Affect of the Fabrication Process on PDMS Dimensions

One important consideration when processing the test results was the dimensions of the PDMS features. The length and cross-sectional area were designed to

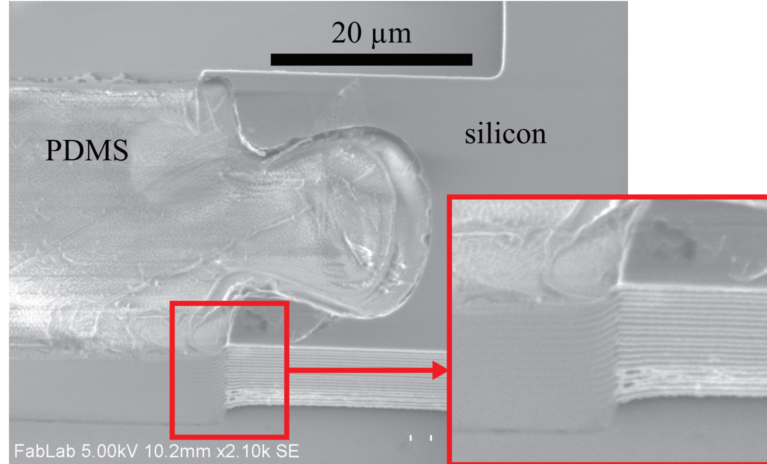

Figure 2.3: SEM image of a silicon and elastomer feature. Note the scalloping is apparent in both the silicon and the PDMS features, signifying the highly conformal refill of the elastomer in the silicon trench.

be consistent on the test features used later in Section 2.1.3 and both were determined from a series of scanning electron microscope (SEM) images. The length was measured to be 30.3 μm (5 measurements, $\sigma = 0.33$). The cross-sectional area was challenging to determine and was affected by two steps in the fabrication: the DRIE in Step 2 and the BHF release in Step 7.

The width of all of the PDMS features used in this work were designed to be 6 μm. The feature patterns were transferred from the photolithography mask to the etch mask on the wafer. Ideally, the DRIE would result in a feature the exact width of the patterned etch mask, however there was some lateral etching that occurred during the DRIE that widened the silicon trenches, shown in Figure 2.4b. The PDMS features were formed by refilling the trenches etched in Step 3 of the fabrication process. The widening was expressed in the PDMS when it filled the

trench, shown in Figure 2.4c. After the PDMS refill, the average feature width was 6.82 μm (18 measurements, $\sigma = 0.27$).

The other step that affected the final width of the PDMS features was the BHF release in Step 7. Devices were released for either 5 or 8 hours in BHF. After the 5 hour release the average width was 4.35 μm (20 measurements, $\sigma = 0.13$). After the 8 hour release the average width was 3.99 μm (6 measurements, $\sigma = 0.08$). This corresponds to a decrease in width of 2.46 μm and 2.82 μm for the 5 and 8 hour releases, respectively, from the pre-release dimension of 6.82 μm due to etching of the polymer by the BHF, shown in Figure 2.4e.

The BHF etch was isotropic, so all exposed surfaces were etched by the same amount, including the top and bottom. The thickness of the device layer of the silicon wafer was measured to be 20.4 μm (4 measurements, $\sigma = 0.06$), but the top and bottom of the PDMS features were also etched, so thicknesses of 17.9 μm and 17.5 μm were used for the 5 and 8 hour released devices, respectively. This did not account for any variations across the surface of the wafer due to the planarization process in Step 4 of the fabrication process.

The 2.46 μm etch of the PDMS over 5 hours and 2.82 μm etch of the PDMS over 8 hours suggests that the etch rate was not constant over time. The etch rate decreased from 0.48 μm per hour during the first 5 hours of the etch to 0.13 μm per hour during the last three hours of the etch. The reason for the change in the etch rate is unknown.

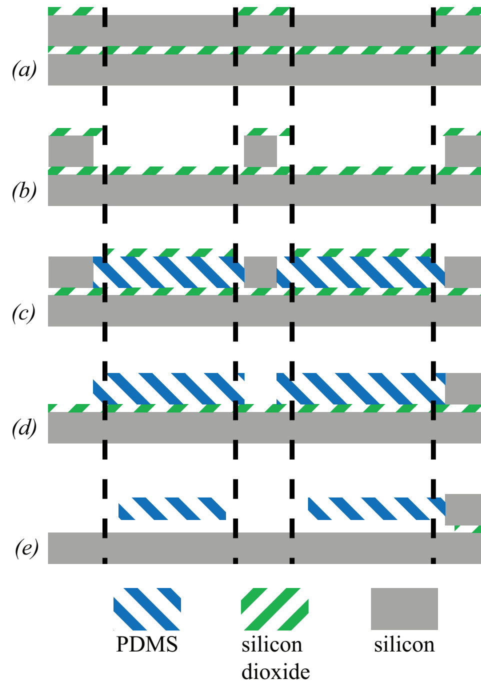

Figure 2.4: A schematic showing a cross-section of the wafer during fabrication to demonstrate the lateral etch of the silicon during the DRIE and isotropic etch of the PDMS during the BHF release. a) the SOI wafer after the first etch mask was patterned b) the wafer after the first DRIE, demonstrating the lateral etch c) the wafer after the second etch mask was patterned d) the wafer after the second DRIE and e) the wafer after the BHF release, demonstrating the etch of the PDMS. The vertical dashed lines show the width of the etch mask from 2.4a. Note: the changes in dimension are not to scale and have been heavily exaggerated to highlight the changes.

2.1.3 DMA and *In situ* Test Procedures

Two types of tests were performed to characterize the mechanical properties of PDMS: macroscale tests with a dynamic mechanical analyzer and microscale *in situ* on-chip tests. This allowed for direct comparison of test results from the macroscale and microscale PDMS samples.

2.1.3.1 DMA Test Procedure

The PDMS manufactured at the macroscale was characterized with a Q800 dynamic mechanical analyzer (DMA) from TA Instruments. The Sylgard 184 base and curing agent of the polymer were mixed by hand, degassed for 10 minutes at 1 Torr, and cured for 2 hours in a polyoxymethylene mold. Three curing temperatures were examined: 70 °C, 90 °C, and 120 °C. Three curing temperatures were used because of the influence of the curing temperature on the resulting stiffness of the PDMS [51, 61, 62].

The DMA tests strained the samples to 10%, 30%, 50%, and 70%, returning to 0% between each level, at a rate of 500% strain per minute. The sample widths were determined by a cutting tool provided by TA Instruments, the lengths were set when loading each sample into the tool, and the thicknesses were determined by the amount of polymer poured into the mold prior to curing. The average sample dimensions were 5.46 mm in width, 9.81 mm in length, and 0.80 mm in thickness

with standard deviations of 0.04 mm, 0.22 mm, and 0.25 mm, respectively. All of the tests were performed at room temperature within 24 hours of the completion of the curing process. For each curing condition at least four samples were tested.

2.1.3.2 *In situ* Test Procedures

The test mechanism for *in situ* characterization, shown in Figure 2.5, included a set of electrostatic comb drive actuators that drove two springs. One was a set of silicon flexures required by the actuators and also used to calibrate the system, shown in Figure 2.5d. Robust silicon flexures were required to maintain lateral stability in the electrostatic actuators and to prevent issues related to stiction during the release. The other spring was the PDMS test sample, shown in Figure 2.5e, which was in parallel with the silicon flexures. The silicon flexures and the PDMS spring were designed to have a similar nominal spring constant so that neither dominated the response of the system.

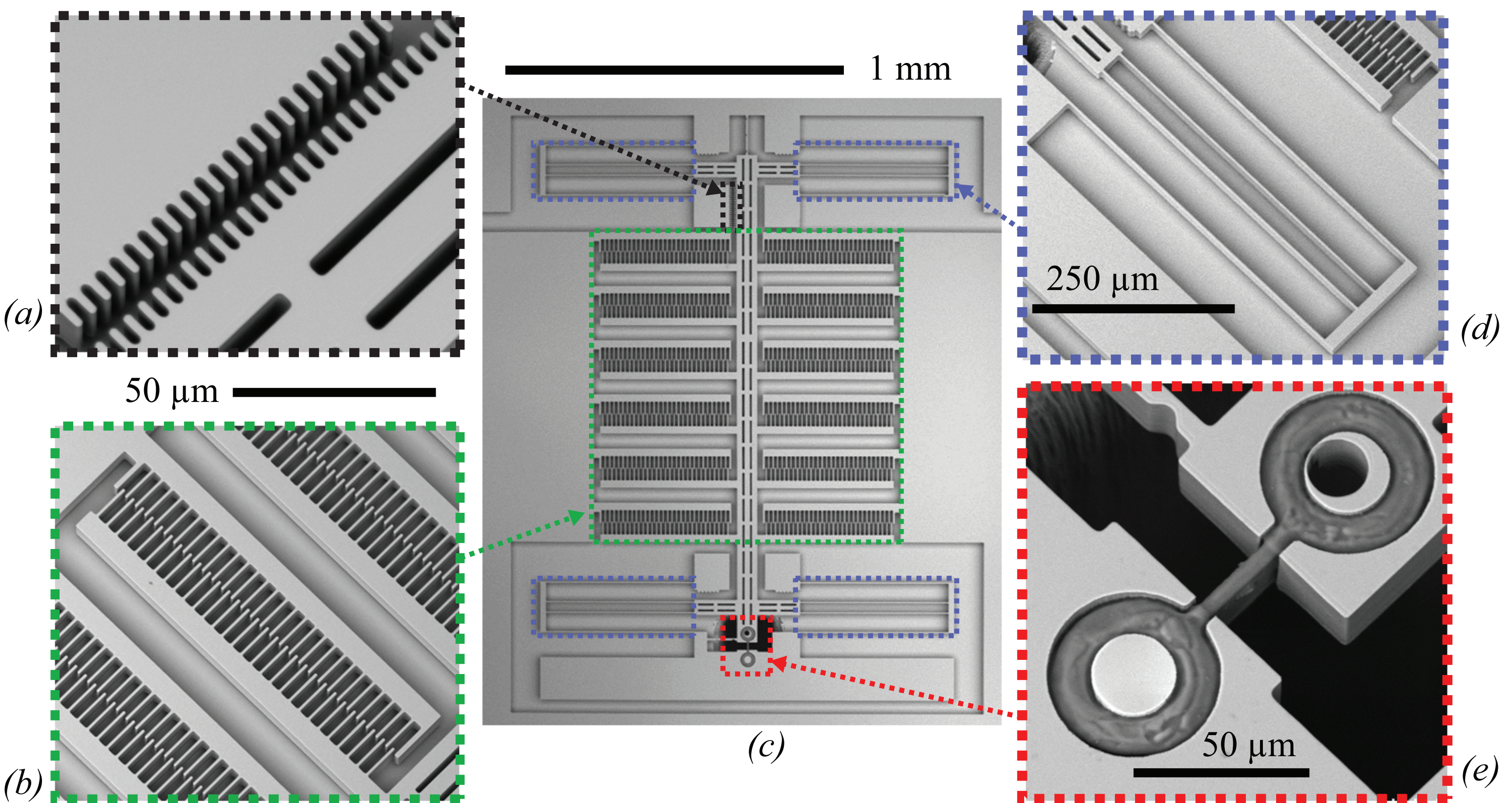

Figure 2.5: SEM image of a fabricated test mechanism. The feature used to measure the displacements is shown in 2.5a. The comb drives are shown in 2.5b. The silicon flexures are shown in 2.5d. A PDMS test sample is shown in 2.5e.

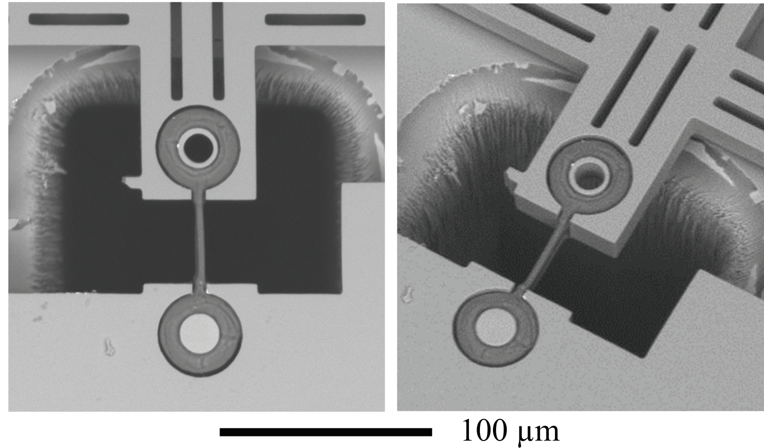

Figure 2.6: SEM image a PDMS spring being strained 65%.

The test mechanism was operated by grounding one set of comb fingers and applying a voltage to the other set of comb fingers. The voltage was ramped from 0 V to the level which corresponded with the maximum displacement, typically 120 V, in 1 V steps. A SEM image of a PDMS spring strained to 65% is shown in Figure 2.6. The step time was not actively controlled, but was roughly 1 s per step, which was determined by the response time of the computer used to capture the images and control the applied voltage.

The PDMS springs were designed to be 30 μm long, 20 μm thick, and 6 μm wide. The fabricated lengths and widths varied slightly from the designed lengths and widths due to lateral etching of the silicon during the DRIE and isotropic etching of the PDMS during the BHF release etch, as was discussed in Section 2.1.2.3.

2.1.3.2.1 Calibration

The variations between each fabricated chip across the wafer and the difference between the designed and manufactured dimensions required that the test mechanisms be calibrated individually. Measuring the force output of MEMS actuators is challenging given the magnitude of the forces. This issue was overcome by using a combined optical and capacitive calibration method.

In order to calculate the force applied to the PDMS spring, the spring constant of the silicon flexures had to be quantified. Once the tests on the PDMS spring were completed, a probe was used to remove the sample while leaving the comb drives and silicon flexures intact. The device could then be calibrated to determine a capacitance coefficient, k_c, and a silicon flexure spring constant coefficient, k_{fl}.

After the PDMS spring was removed, the static equilibrium of the system was maintained by the balance of the electrostatic force in the comb drives, F_{cd}, and the spring force in the silicon flexures, F_{fl}, or $F_{cd} = F_{fl}$. The electrostatic force can be calculated with Equation 2.1:

$$F_{cd} = N\varepsilon\frac{t}{g}V^2 \tag{2.1}$$

where N is the number of fingers on one side of the actuator, ε is the permittivity, t is the thickness of the fingers, g is the gap between the fixed and moving fingers, and V is the applied voltage. Equation 2.1 can be simplified to $F_{cd} = k_{cd}V^2$, where

$k_{cd} = N\varepsilon\frac{t}{g}$ is a constant.

The theoretical capacitance of the actuator can be calculated with Equation 2.2:

$$C = 2N\varepsilon\frac{t}{g}x \tag{2.2}$$

where x is the overlapping area between the fixed and moving fingers. Equation 2.2 can be simplified to $C = k_c x$, where $k_c = 2N\varepsilon\frac{t}{g}$ is a constant. It is clear that $k_{cd} = \frac{1}{2}k_c$, so Equation 2.1 can be written as

$$F_{cd} = \frac{1}{2}k_c V^2. \tag{2.3}$$

Using this equation, the force applied by the actuators is a function of only the applied voltage.

Returning to the equilibrium between the actuator and the silicon flexures, Equation 2.3 and Hooke's Law can be used to show that $\frac{1}{2}k_c V^2 = k_{fl}\Delta x$ where Δx is the comb drive displacement. Solving for the silicon flexure spring constant coefficient k_{fl} shows that

$$k_{fl} = \frac{1}{2}k_c\frac{V^2}{\Delta x}. \tag{2.4}$$

The terms V^2 and Δx can be combined in a single coefficient as $k_{Vx} = \frac{V^2}{\Delta x}$. This simplifies Equation 2.4 to:

$$k_{fl} = \frac{1}{2} k_c k_{Vx}. \tag{2.5}$$

Determining the silicon flexure spring constant allows for isolating the force applied to the silicon flexures from the force applied to the PDMS spring.

In order to determine the force applied to the PDMS springs, two tests were performed to determine the k_c, k_{Vx}, and k_{fl} terms. The k_c term was determined by manually advancing the comb drive with a probe tip while measuring the displacement and capacitance. The constant k_c was the slope of the linear fit of the measured capacitance versus displacement points. The k_{Vx} term was determined by driving the actuators from 0 V to the voltage at the maximum displacement, typically 60 V, in 1 V steps. The constant k_{Vx} was the slope of the linear fit of the measured displacement versus voltage squared points. The constant k_{fl} was then calculated with Equation 2.5. Detailed information on the k_c and k_{Vx} terms is available in Appendix B.

The capacitance of the system was measured using an Analog Devices AD7745/46 Evaluation Board. This board was not useful for measuring exact capacitance values, but was well suited for measuring changes in capacitance. Displacement of the comb drives was monitored using an optical method [63]. Two sets of silicon features were patterned, shown in Figure 2.5a: one set that was anchored to the substrate and one that was on the moving shuttle of the actuator. The features were a series of 2.5 μm silicon teeth separated by 2.5 μm gaps, detailed in Appendix C. The displacements of the two sets were monitored by capturing a photograph at each voltage step. These

images were analyzed using a MATLAB script with the displacement of the teeth as the output. The influence of vibrations of the entire die was reduced by monitoring the displacement of both the moving and fixed features. This was accomplished by subtracting the displacement of the fixed features from the displacement of the moving features.

2.1.3.2.2 ***In situ*** **Stress and Strain**

Prior to the calibration tests which required removing the PDMS springs, the characterization tests of the PDMS samples were performed. The force applied to the PDMS springs was calculated by examining the static equilibrium $F_{cd} = F_{fl} + F_{spr}$, where F_{spr} was component of the force applied to the PDMS spring and F_{fl} was the component of the force applied to the silicon flexures. Solving for the spring force and substituting Equation 2.3 and Hooke's Law shows that

$$F_{spr} = \frac{1}{2}k_c V^2 - k_{fl}\Delta x. \tag{2.6}$$

The terms k_c and k_{fl} were determined during the calibration. The resulting data was the PDMS spring force, F_{spr}, and a displacement, Δx, which were then converted to a stress and a strain by dividing by the cross-sectional area and length of the PDMS spring, respectively, that were calculated in Section 2.1.2.3.

2.1.3.2.3 Geometric Coefficient

The PDMS spring consisted of the central spring and two attachment mechanisms, one on each end, which interfaced the PDMS springs with the silicon device, shown in Figures 2.7 and 2.5e. These PDMS and silicon features were fabricated together and were not assembled, so these attachment mechanisms helped to prevent delamination by mechanically interlocking the silicon and PDMS. These attachment points, however, affected the actual strain achieved in the central test spring because they did not provide a rigid boundary condition, but rather deformed along with the central spring. The displacement measurements were made on the silicon features shown in Figure 2.5a and not the PDMS springs themselves, so the influence of the mechanisms on the strain in the central spring had to be determined.

The effect of the mechanisms on the strain was determined by performing a finite element analysis (FEA) in ANSYS. A three-dimensional model, which represented the devices as they were designed, was created using the SOLID5 element. The Young's modulus and Poisson's ratio of the silicon were set to 160 GPa and 0.29, respectively [28]. The Young's modulus and Poisson's ratio of the PDMS were set to 1.4 MPa and 0.499, respectively [44]. The model was given prescribed displacements from 1 to 20 μm in 1 μm steps. The expected strain from the displacement was then compared to the calculated strain in the center of the PDMS sample at each step.

As the displacement was varied from 1 μm to 20 μm, the strain in the center of the PDMS sample was consistently 93% of the strain that was expected as a result of

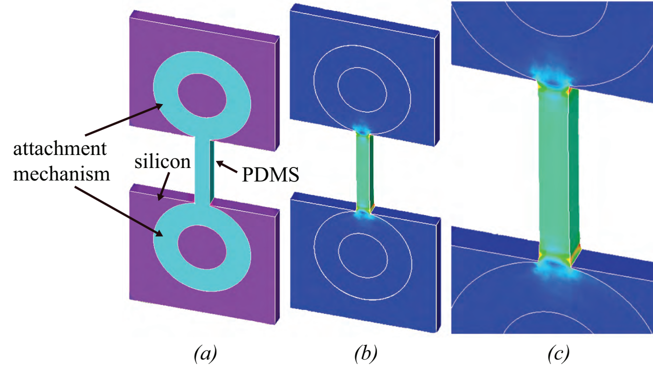

Figure 2.7: a) The undeformed model showing the attachment mechanisms, b) FEA results showing the penetration of the strain into the attachment mechanisms, and c) a closeup of the central spring.

the displacements applied by the model. This discrepancy was consistent for all strain ranges, even when the Young's modulus of the PDMS was increased and decreased, demonstrating the effect was insensitive to variations in strain and Young's modulus. The decreased strain was a result of the work that was done to strain the PDMS in the attachment mechanisms. To compensate for this effect, a coefficient was introduced. Equation 2.7 relates the actual strain, ε_{actual}, to the measured strain, $\varepsilon_{measured}$, with a geometric coefficient η_{geom}.

$$\varepsilon_{actual} = \eta_{geom}\varepsilon_{measured} \tag{2.7}$$

The results of the FEA showed that $\eta_{geom} = 0.93$.

2.1.4 Results

Using the procedures described in Section 2.1.3, tests on both the macroscale and microscale samples were performed in order to characterize the PDMS.

2.1.4.1 DMA Characterization

The results from the macroscale DMA tests are shown in Figure 2.8. The results shown in this figure include at least four samples for each curing temperature, 70 °C, 90 °C, and 120 °C. The multiple samples tested at each curing temperature were from the same PDMS mixtures. In order to evaluate the possibility of variation between mixtures contributing to the change in the stiffness, four separate mixtures were prepared, cured at 120 °C, and tested, with results shown in Figure 2.9. The variation from one PDMS mixture to the next was significantly less than the variation seen when changing the curing temperature, demonstrated in Figures 2.8 and 2.9.

Figures 2.8 and 2.9 show that there was some variation in the maximum strain that was achieved in each cycle. The same test procedure was run on each sample, but strain achieved by the DMA varied slightly. The cause of this is unknown but likely stemmed from the performance of the DMA when testing small samples of compliant materials, such as PDMS.

The data for the elongation of the samples was fit to the uniaxial tension Hooke, Neo-Hookean, and second-order Ogden material models, shown in Equations 2.8, 2.9,

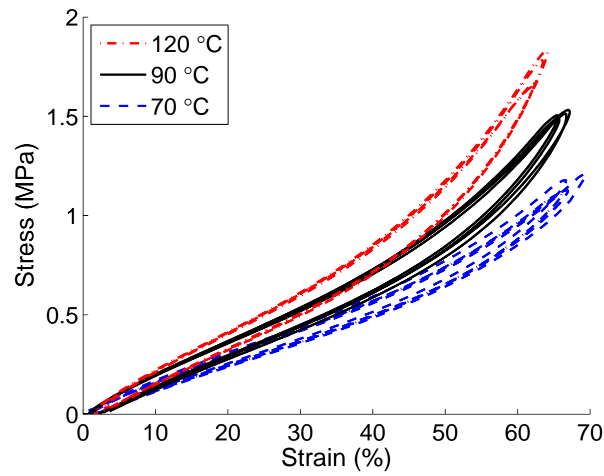

Figure 2.8: Stress-strain results for the macroscale PDMS samples cured for 2 hours at 70 °C, 90 °C, and 120 °C.

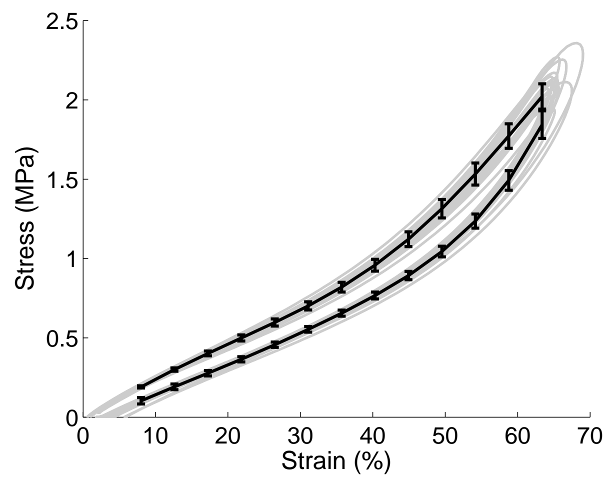

Figure 2.9: Stress-strain results for eighteen macroscale PDMS samples from four mixtures cured for 2 hours at 120 °C. The gray curves represent all eighteen samples and the black line shows the average and standard deviation.

and 2.10, respectively, where λ is the stretch ratio and C_H, C_{NH}, α_i, and μ_i are material constants [64, 65, 66]. It is worth noting that these equations require being fit to the stretch ratio ($\lambda = \varepsilon + 1$), but some of the results provided later are plotted against strain, for clarity. It is interesting to consider the Neo-Hookean and Ogden fits, not only the linear Hooke fit, because of the non-linearity of PDMS at large deformations. Each of these material models has it own pros and cons the Hooke model is simple to implement and fit to, but the Ogden model provides a more accurate description of elastic materials, especially at higher strains. The Hooke model shows that the force in the material is proportional to the applied strain. The Neo-Hookean model is slightly different in that it shows that the stress, not force as in the case of the Hooke model, in the material is proportional to the applied strain. Each of these can provide accurate fits for elastic materials at small strains, but at larger strains other material models such as the Ogden model should be used as they are better at predicting the behavior of elastomers at higher strains.

At large strains, elastomeric materials display phenomenon which leads to the stress in the material increasing at an increasing rate as the strain increases. This can be seen in the DMA results shown in Figure 2.8, especially in the samples cured at 120 °C. As the strain increases above 40%, the stress begins to increase at a higher rate. The Ogden model accurately predicts this material behavior at higher strains [66, 67]. This behavior is a function of the elongation of the polymer chains in the elastomer. When no stress is applied, the chains are tangled and meander through the

bulk. As the chains are strained they start to align with the applied stress. Eventually the chains become fully elongated and there is a transition from a straightening of the chains along the direction of the stress to elongation of the chains themselves by straining the chemical bonds. This transition results in a greater pressure needed to elongate the elastomer, as seen in the upturn in slope of the stress-strain curve at approximately 40%. The Ogden model is based on a strain-energy relationship through which the stress-strain relationship can be derived [68].

$$\sigma_{eng}^{H} = C_H\left(\lambda - 1\right) \tag{2.8}$$

$$\sigma_{eng}^{NH} = 2C_{NH}\left(\lambda - \lambda^{-2}\right) \tag{2.9}$$

$$\sigma_{eng}^{O} = \sum_{i=1}^{2} \mu_i\left(\lambda^{\alpha_i - 1} - \lambda^{-\frac{1}{2}\alpha_i - 1}\right) \tag{2.10}$$

The Hooke and Neo-Hookean models were used because of their relative simplicity and the Ogden model was used because of its relative accuracy in describing the behavior of the experimental results. The Hooke model does not capture the non-linearity of PDMS and the Neo-Hookean model plateaus and does not predict the rise in stress at higher strains. The Ogden model, however, does allow for an increased stress at larger strains, leading to a more appropriate fit for non-linear materials such as PDMS.

The fits to the three material models for the samples cured for 2 hours at 70, 90 and 120 °C are shown in Figure 2.10c and Table 2.1. The Neo-Hookean and Ogden model coefficients were calculated using the curve-fitting tool in ANSYS and the Hooke model coefficient was calculated using Excel. As was expected, the Ogden model fit better than the Hooke model, which in-turn fit better than the Neo-Hookean model. As was mentioned above, it is important to note that while Figure 2.10 is plotted with units of MPa and percent strain, the coefficients in Table 2.1 are for the stress in MPa and the stretch ratio so that they correspond with Equations 2.8, 2.9, and 2.10. All of the data show the engineering stress and strain, as opposed to the true stress and strain.

While the Hooke model is linear, the Neo-Hookean and second order Ogden models are non-linear. A Young's modulus can still be extracted from each of these fits, as shown in Equations 2.11, 2.12, and 2.13 [64, 65]. The values of the moduli are listed in Table 2.1.

$$E^{H} = C_{H} \tag{2.11}$$

$$E^{NH} = 6C_{NH} \tag{2.12}$$

$$E^{O} = \frac{1}{2}\sum_{i=1}^{2} \mu_i \alpha_i \tag{2.13}$$

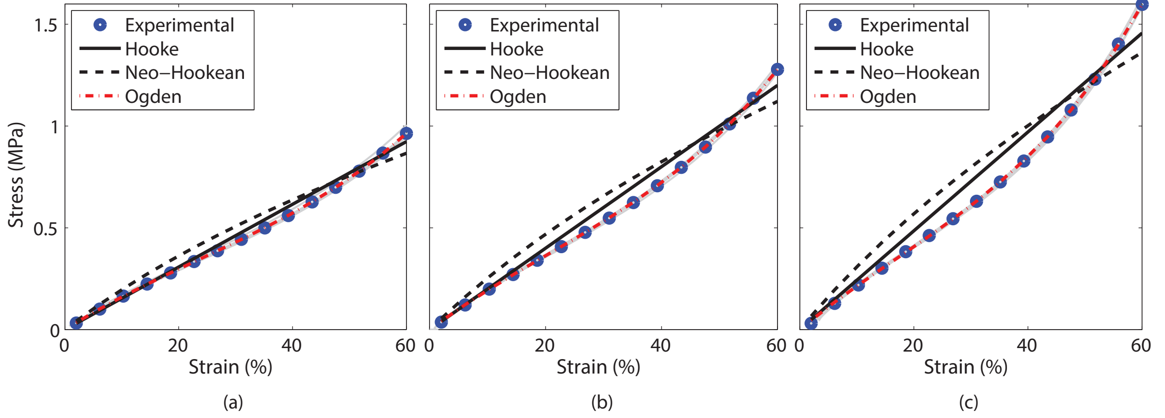

Figure 2.10: Stress-strain curves for the elongation of the macroscale samples cured for 2 hours at (a) 70 °C (b) 90 °C and (c) 120 °C.

Table 2.1: Nonlinear coefficients and calculated Young's moduli for the elongation of macroscale PDMS samples cured for 2 hours at three different temperatures.

	Hooke		Neo-Hookean		2nd Order Ogden				
	C_H*	E_H*	C_{NH}*	E_{NH}*	μ_1*	α_1	μ_2*	α_2	E_O*
70 °C	1.54	1.54	0.358	2.15	0.0198	7.90	12.9	0.0801	1.78
90 °C	2.00	2.00	0.464	2.78	0.0277	8.02	82.2	0.0147	2.14
120 °C	2.43	2.43	0.563	3.38	0.0352	8.18	36.9	0.0345	2.34

* units in MPa

2.1.4.2 *In situ* Characterization

Using the test mechanism and procedure described in Section 2.1.3.2, microscale PDMS spring samples were tested. The samples were manufactured using the process described in Section 2.1.2 with either a 5 or 8 hour 18:1 BHF release time. After the tests were performed, the device was calibrated and the acquired images were processed to produce the stress-strain data. The focus of this section is on the elongation phase of the tests and not the contraction phase. Dynamic testing to characterize

the viscoelastic behavior of PDMS will be a focus of future work, which requires simultaneous force and displacement sensing on-chip at higher speeds.

As was mentioned in Section 2.1.3.2, the test mechanism was nominally designed so that the spring constants of the silicon flexures and PDMS springs were the same. The manufactured devices varied slightly from the designed value as a result of the fabrication. The silicon flexures were designed to have a spring constant of 10.8 N/m but the fabricated devices had an average spring constant of 2.39 N/m. The discrepancy between the designed and fabricated spring constants was caused by the lateral etching and footing, which was discussed in Section 2.1.2.3, and resulted in a reduction of the width and thickness of the silicon features. The spring constant has a cubic dependence on the width of the flexures, so lateral etching led to dramatic changes in the final spring constant. Assuming a linear modulus of 1.4 MPa [44], the PDMS springs were designed to have a spring constant of 5.6 N/m.

2.1.4.2.1 Long-term stability

The long-term stability of the PDMS was examined by cycling a sample 1,000 times and collecting stress-strain data every 100 cycles. Figure 2.11 shows that there was little discernible change in the stress-strain results, demonstrating that the PDMS samples were stable over strains to 65% for at least 1,000 cycles. One curve in Figure 2.11 is slightly offset from the others. This was the first cycle performed during the test, demonstrating that there was a slight change from cycle 1 to cycle 100, but not

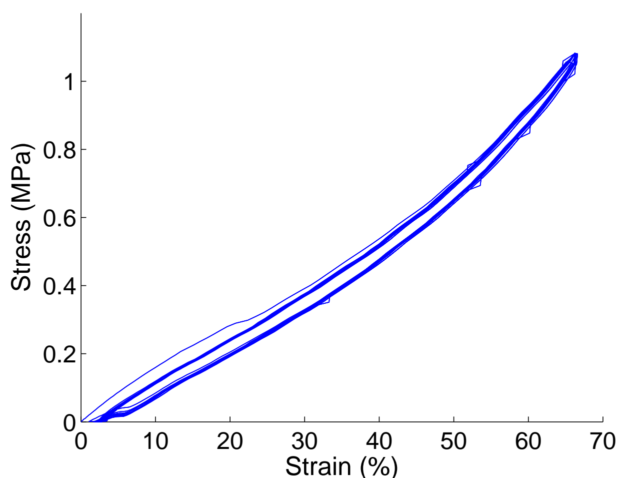

Figure 2.11: Results representing 1,000 strain cycles on microscale samples. This figure shown eleven curves, one to represent every 100$^{\text{th}}$ cycle.

from cycle 100 to cycle 1,000. This change after the first cycle is likely a result of the Mullins effect which says that the stiffness of elastomers decrease to a steady-state value as they are cycled [69, 70].

2.1.4.2.2 Test Results

The stress-strain curves for the PDMS samples tested *in situ* are shown in Figures 2.12, 2.13, and 2.14. Figure 2.12 shows the curves for both the 5 and 8 hour BHF releases. There were four samples tested with a 5 hour release and seven samples tested with an 8 hour release. The results shown in theses figures do not all represent the same cycle; the cycle shown ranged from the second cycle to the tenth cycle. The samples occasionally had to be cycled a few times during setup of the tests. In Figure 2.12 there are two clusters of lines. The group with the higher slope and red

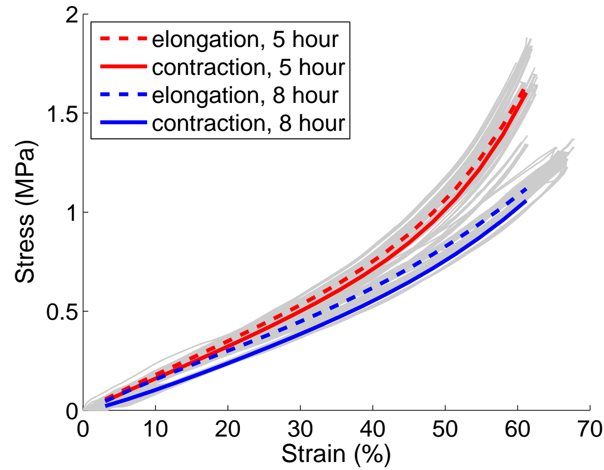

Figure 2.12: Stress-strain curves for the microscale PDMS samples released for 5 and 8 hours.

average curves represents the samples released for 5 hours and the group with the lower slope and blue average curves represents the samples released for 8 hours. The dashed curves show the average curve during elongation and the solid curves show the average curve during contraction.

Figures 2.13 and 2.14 show the elongation of the samples released for 5 and 8 hours, respectively, as well as the Hooke, Neo-Hookean, and second-order Ogden model fits. The coefficients and calculated moduli for each of these models are listed in Table 2.2. As with the DMA results, the Ogden model was the best fit for the collected data.

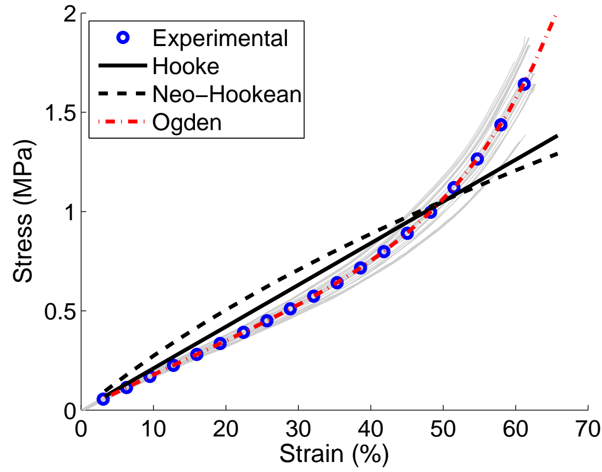

Figure 2.13: Stress-strain curves showing the elongation of the microscale PDMS samples released for 5 hours.

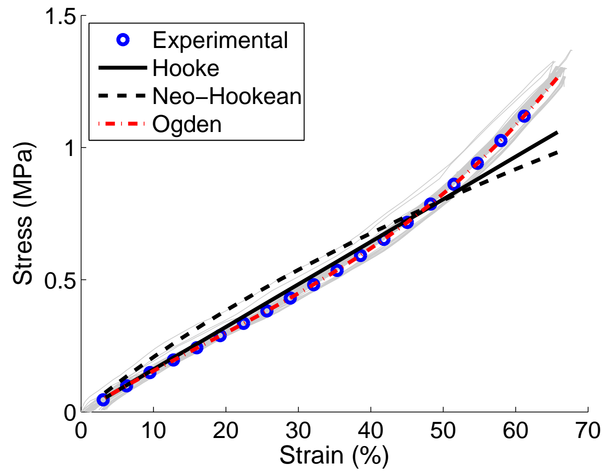

Figure 2.14: Stress-strain curves showing the elongation of the microscale PDMS samples released for 8 hours.

Table 2.2: Nonlinear coefficients and calculated moduli for elongation of microscale PDMS samples tested *in situ* after 5 and 8 hour release times.

	Hooke		Neo-Hookean		2nd Order Ogden				
	C_H*	E_H*	C_{NH}*	E_{NH}*	μ_1*	α_1	μ_2*	α_2	E_O*
5 hour	2.10	2.10	0.458	2.75	1.19×10^{-3}	14.2	0.381	3.24	1.88
8 hour	1.61	1.61	0.315	1.89	5.03×10^{-2}	6.72	4.61	0.161	1.68

* units in MPa

2.1.5 Discussion

The macroscale samples were characterized at three temperatures: 70 °C, 90 °C, and 120 °C. Table 2.1 shows that for all three of the material models, the PDMS Young's moduli calculated with Equations 2.11, 2.12, and 2.13 increased as the curing temperature increased. This data agrees with previously published works that have characterized Sylgard 184 PDMS [44, 51, 61]. The microscale samples were cured at 90 °C and were characterized at two different release times: 5 and 8 hours. Table 2.2 shows that for all three of the material models, the PDMS Young's moduli calculated with Equations 2.11, 2.12, and 2.13 decreased as the release time increased.

It is well understood that increasing the curing time and temperature of PDMS increases the stiffness of the material [51, 61, 62]. As temperature is increased, the crosslink density is also increased, which means that the length of the polymer chains between crosslinks is decreased. When the polymer chains are deformed, these shorter chains become fully elongated at lower strains and therefore require more force to elongate farther. Other work has shown that the modulus of silicones is proportional to the crosslink density [71, 72, 73].

2.1.5.1 Comparison of the Macroscale and Microscale Samples

A comparison of the data collected from the macroscale samples characterized with the DMA and the microscale samples characterized *in situ* is presented in Figure

2.15. The stress required to strain the microscale samples released for 8 hours was similar to the stress required to achieve the same strains in the macroscale samples cured at 70 °C. The stress required to strain the microscale samples released for 5 hours was similar to the stress required to achieve the same strains in the macroscale samples cured at 90 °C. Both of these statements are confirmed by the comparison of the Young's moduli calculated for the Hooke, Neo-Hookean, and Ogden models presented in Tables 2.1 and 2.2.

These results can be used to justify two hypotheses about the processing of PDMS in SOI-MEMS. The microscale samples that were released for 5 and 8 hours were exposed the same processing prior to the BHF release but the stiffness of the sample released for 8 hours was less than the stiffness of the sample released for 5 hours. This leads to the first hypothesis which says that the BHF exposure reduced the crosslink density, and therefore stiffness, of the PDMS. Additionally, the stiffness of microscale samples that were cured at 90 °C and released for 5 hours was similar to the stiffness of the macroscale samples that were cured at 90 °C. The first hypothesis, however, states that the stiffness was reduced during the 5 hour release. By extrapolating the data, this means that the crosslink density of the microscale samples must have been higher just before the BHF release than it was just after the initial cure of the PDMS. So, even though the microscale sample cured at 90 °C and released for 5 hours and the macroscale sample cured at 90 °C had similar stiffnesses, this was just a coincidence. This leads to the second hypothesis which says that all

of the processing that the PDMS was exposed to after its initial cure but before the BHF release led to additional curing of the polymer, therefore increasing the crosslink density and stiffness of the material.

It is important to note that while the decrease in crosslink density is considered in the discussion above as a change in the entire volume of the PDMS samples, the working hypothesis is that this was actually a surface effect. The ability of the BHF to decrease the crosslink density of the PDMS is limited by its diffusion rate through the volume of the PDMS. It is possible that there was a gradient in the crosslink density and that the measured stiffness of the PDMS was, effectively, a weighted average across the entire cross-section of the PDMS. This would mean that while the conclusions presented above are valid for samples with the geometry used in this work, these conclusions should not necessarily be extrapolated up or down to sample sizes with larger or smaller cross-sectional areas. Larger samples which would likely be less effected because of a larger ratio of volume-to-surface area and smaller samples would likely be more effected because of a smaller volume-to-surface area ratio.

2.1.5.2 Implications for PDMS Processing in SOI-MEMS

Figure 2.15 shows that test results for macroscale samples can not necessarily be used to describe processed microscale PDMS. A second-order Ogden model fit to test results for macroscale PDMS cured at 90 °C was used to calculate a modulus of 2.14 MPa, shown in Table 2.1. The same fit to test results for microscale samples cured at

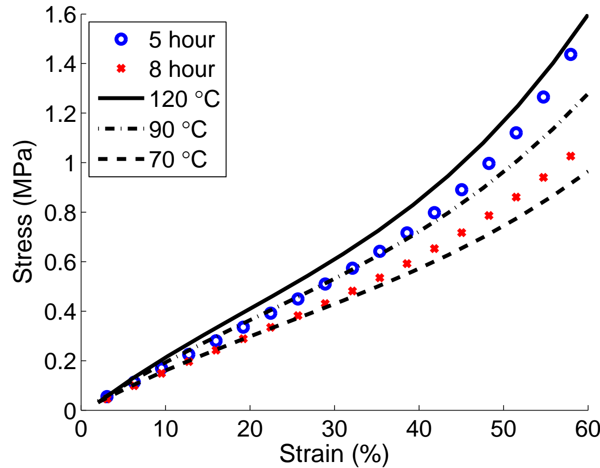

Figure 2.15: Stress-strain curves showing the average data for the elongation of the microscale and macroscale PDMS samples.

90 °C and released for 8 hours was used to calculate a modulus of 1.68 MPa, shown in Table 2.2. This represents a 22% difference between the moduli calculated for the microscale processed and the macroscale unprocessed PDMS. This is a difference significant enough that it is necessary to consider in the design of any mechanical systems which might include PDMS components.

Since the comparison of the microscale and macroscale test results imply that that the processing steps affect the mechanical properties of the PDMS, it is necessary to examine which of these steps affect the material. The steps that influenced the pre-release stiffness of the PDMS likely included the brief 2 minute 47 second 150 °C PECVD deposition that formed the silicon dioxide etch mask for the DRIE in Step 5 of the fabrication process. There were also several brief soft bakes of photoresists at 90 °C prior to the lithography for Steps 5 and 6. Finally, the PDMS was present

on the wafer during several plasma etches including the DRIE of the silicon in Steps 5 and 6, the inductively coupled plasma reactive ion etch (ICP-RIE) to pattern the silicon dioxide etch mask in Step 5, and several oxygen plasmas to clean the surface of the wafer and promote photoresist adhesion throughout all of the processing steps. Exposure to the plasmas may have cured the PDMS more by increasing the temperature of the wafer during the etches or by changing the surface chemistry of the PDMS. This is especially true of the 2 hour and 20 minute DRIE etch on the handle layer of the wafer during Step 6 of the fabrication process. The DRIE tool uses helium to cool the bottom of the wafer, but the temperature of the wafer still increases during the etch as a result of heat transfer from the plasma to the wafer [74, 75]. The possible effects of all of the processing steps on the mechanical properties of the materials must be considered when determining the specifics of the processing and details of the device design. It should be noted that the specific influences of each of the individual steps on the resulting stiffness of the PDMS were not tested in this work and are presented as something to be tested in future work.

There are also some design rules for PDMS processing that come from this work. The dimensions of PDMS features must account for both any lateral etch during the DRIE which expands the dimensions and the isotropic BHF etch of the PDMS which reduces the dimensions. The lateral etch is a factor of the DRIE tool and the recipe used during the etch. The time duration of the BHF etch is determined by the distance the BHF must etch the silicon dioxide underneath the silicon in order

to fully release the silicon features. Etch holes that allow for access of the BHF to the underlying oxide can be used to shorten the etch. The devices used in this work required a silicon undercut of 20 μm. Another factor that influenced the required etch time was the strength of the BHF. In this work 18:1 BHF was used; 6:1 BHF was diluted down to 18:1 because the 6:1 BHF was qualitatively determined to be too strong as it rapidly etched the PDMS, resulting in unusable samples. Based on the results of this work, a device must have a width greater than 2.5 μm for a 5 hour release and greater than 2.8 μm for an 8 hour release to have any remaining PDMS.

2.1.6 Elastomer Adhesion, Ultimate Strain, and Hysteresis

This section presents the characterization of several other important metrics of the fabricated polymer: the silicon-elastomer adhesion, the ultimate strains that could be reached in the elastomer, and the hysteresis of the elastomer.

2.1.6.1 Silicon-Elastomer Adhesion

In addition to the stress-strain behavior which has been discussed, adhesion of the fabricated silicon and elastomer features was critically important. If the adhesion of the two materials was not sufficient, the silicon and elastomer features would delaminate under normal operating conditions. Ideal adhesion would allow the elastomer to reach its ultimate strain before the silicon and elastomer features delaminated. Test structures to examine the normal adhesion were designed and fabricated. These

structures consisted of the elastomer that was under investigation in series with a silicon spring. The silicon spring was designed using ANSYS to have a spring constant of 4.35 N/m. The spring constant was recalculated after fabrication to account for any lateral etch during the DRIE. The DRIE process also does not fabricate perfectly vertical sidewalls, trenches are either tapered in and form a v-shaped trench or are tapered out and form a re-entrant trench. The specific process parameters during the etch, especially the etch and passivation times, dictate whether the trench will be v-shaped or re-entrant. The DRIE process used during the silicon etch was tailored to have re-entrant trenches with an aspect ratio of 25:1. During analysis, the silicon walls were assumed to be vertical, which added some uncertainty to the calculated spring constant for the silicon springs. See Appendix A for more information on the fabrication. A probe was used to manually apply a force to the end of the silicon spring and this same force was transferred to the elastomer. For analysis, micrographs were taken at several stages as the applied force was increased.

The test structure used to measure the normal adhesion is shown in Figure 2.16. The ultimate pressure at which the elastomer delaminated from the silicon due to a normal force occurred over the range of 0.8 to 1.6 MPa in eight tests. It is worth noting that these values were calculated using an estimated spring constant for the silicon flexures, not a calibrated spring constant.

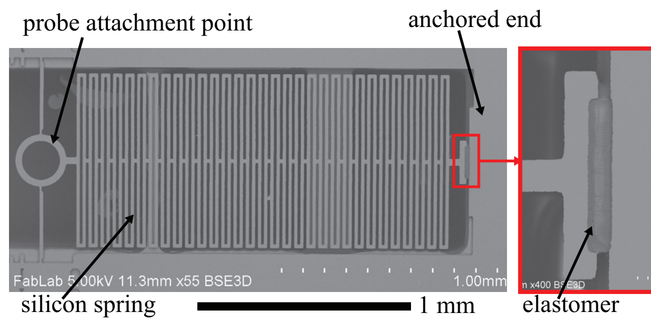

Figure 2.16: SEM of the test structure used to measure normal adhesion.

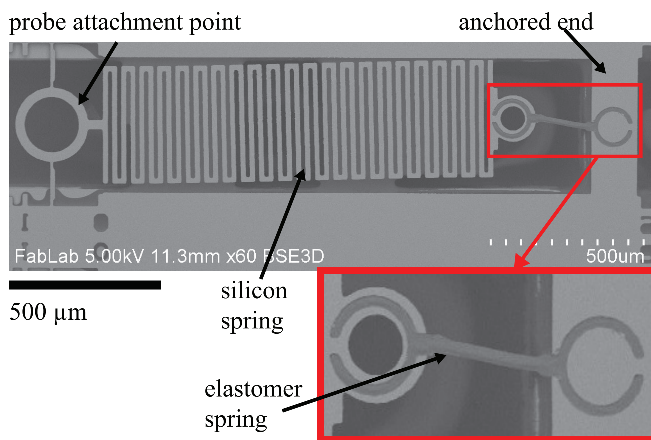

Figure 2.17: SEM of the test structure used to measure strain characteristics.

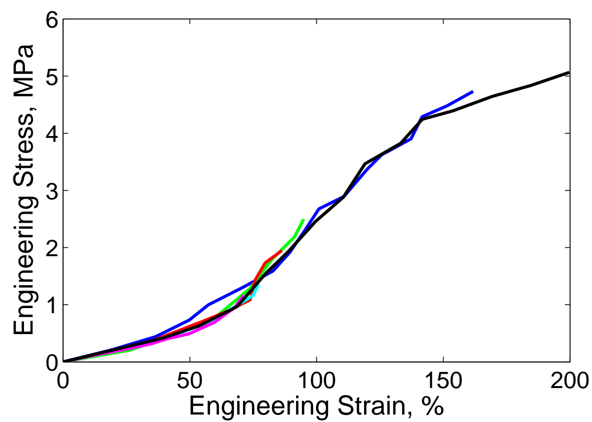

Figure 2.18: Stress-strain curves for Sylgard 184.

2.1.6.2 Ultimate Strain Behavior of Processed Elastomer

The ultimate strain behavior of the elastomer is important for understanding the mechanics of any device, especially one which uses the elastomer for mechanical energy storage. The design of the test structures used for the *in situ* characterization allowed for strains up to only 65%, so test structures used to characterize the ultimate strain of the materials were fabricated, shown in Figure 2.17. The structure had a silicon spring in series with a 1 mm long elastomer spring. These tests brought the structures to failure, which was typically due to delamination of the elastomer from the silicon in the c-shaped region of the structure, but was twice due to failure of the elastomer spring. Failure occurred at an average elongation of 116% over eight tests. Elongation of both the elastomer spring and the silicon spring were used to calculate the response of the elastomer spring. The calculated stress-strain curves of Sylgard 184 for eight separate test structures are shown in Figure 2.18. While the failure mechanism for most structures was delamination of the elastomer from the silicon surface in the c-shaped region of the structures, strains as high as 200% were achieved. This is slightly greater than the 180% maximum strain that has been reported in literature for unprocessed Sylgard 184 [51].

2.1.6.3 Hysteresis in Processed Elastomer

Stretching and relaxing an elastomer for energy storage incurs losses due to heating and friction from the rubbing of the crosslinked polymer chains as they reorganize during elongation or contraction of the bulk [76]. Two tests of the hysteresis of Sylgard 184 using the test structure shown in Figure 2.17 are shown in Figure 2.19. The solid curve had 15% energy loss during relaxation of the Sylgard 184 and the dashed curve had 27% energy loss during relaxation, though this test brought the elastomer to a higher maximum strain. These tests were performed by slowly manually straining and relaxing the elastomer spring. These results are similar to the hysteresis visible in the results from the tests on the macroscale samples in Section 2.1.4.1 as well as other work which have characterized silicone materials [62]. As with the tests of the silicon-elastomer adhesion, the data presented in Figure 2.19 used a calculated spring constant to determine the stress, but the strains were measured directly. The results, however, are independent of any error on the stress as they only depend on the change in the stress and strain, not the absolute value.

2.1.7 Conclusions

This discussion presents a comparison between the results of *in situ* tests performed on microscale samples with a custom MEMS device fabricated in an SOI wafer and similar tests performed on macroscale samples with a dynamic mechanical

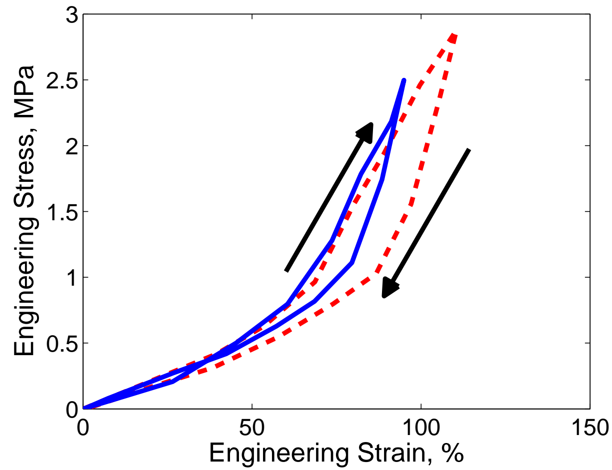

Figure 2.19: Hysteresis curves for Sylgard 184.

analyzer. The macroscale tests demonstrated a strong dependence of the material stiffness on the curing temperature. The *in situ* results showed that the various microfabrication steps initially led to increased crosslinking of the PDMS, but that the final release in BHF decreased the crosslinking, resulting in a decreased stiffness of the PDMS. The 5 hour BHF release resulted in a 2.5 μm isotropic etch of the PDMS while the 8 hour release resulted in a 2.8 μm etch. Coefficients and calculated moduli for the Hooke, Neo-Hookean, and Ogden material models were also presented. Long-term tests showed that the PDMS was stable over at least 1,000 cycles to 65% strain. Test structures measured hysteresis in PDMS of 15% and 27%, yield strains in PDMS as high as 200%, and adhesion of PDMS to silicon around 1 MPa.

2.2 Dielectric Breakdown of PDMS Thin Films

2.2.1 Introduction

This dissertation uses PDMS in electrical devices as well as mechanical devices, so characterization of properties like the dielectric breakdown is important. Dielectric breakdown, or change in the molecular structure of a solid resulting in a dramatic increase in conductivity of the material [77], is well characterized in materials traditional to microfabrication such as oxides [78, 79, 80]. Polymers like PDMS, however, have not been thoroughly characterized, especially at thicknesses approaching single micrometers. PDMS is often used for encapsulation of electronics, in medical devices [42], and as a flexible substrate for electronics [35, 81]. PDMS is also used as a functional mechanical material in systems such as actuators and pumps and valves for microfluidics. Some dielectric elastomer actuators (DEAs), a type of electroactive polymer actuator, use PDMS as a compliant dielectric material to separate electrode layers [82, 83], but one of the most common failure modes in DEAs is electrical breakdown [84, 85, 86]. In most of these applications mentioned, PDMS is used primarily for its mechanical properties, but knowledge of electrical properties such as the dielectric breakdown point would be beneficial for design and optimization of electromechanical systems. The purpose of this section is to characterize the dielectric breakdown of PDMS thin films with thicknesses from 2 to 14 μm.

As the film thickness of PDMS approaches single micrometers, it becomes in-

creasingly difficult to achieve uniform thicknesses, so testing of such thin films is rare. There are many examples of previously published works that report single points for breakdown field or voltage ranging from 19 V/μm to 133 V/μm [60, 87]. There are no works that study the breakdown fields as a function of film thickness below 100 μm. This makes analysis of the breakdown fields for PDMS difficult because of the different methods used in each of these works. The closest example looked at the breakdown of PDMS at three sub-15 μm thicknesses between a rigid electrode and a conductive fluid droplet separated by PDMS for electrowetting [88]. Test structures fabricated in a silicon-on-insulator (SOI) wafer to test the dielectric breakdown of PDMS thin films are described below in this section.

This discussion begins with a description of the fabrication process and design of the test structures in Section 2.2.2. The results are presented in Section 2.2.3 followed by a discussion in Section 2.2.4. Finally, conclusions and future work are presented in Section 2.2.5.

2.2.2 Design and Fabrication of Test Structures

PDMS thin films are typically obtained by either spinning a pre-cure viscous mixture on a rigid substrate (the film thickness decreases as the spin speed increases) or by using soft lithography to mold the PDMS features [42, 89]. Both of these processes are limited in the minimum thickness uniform films that can be achieved. This section employs a molding technique similar to soft lithography and based on a

fabrication process which has been used to create PDMS-based microelectromechanical systems (MEMS) [44, 90]. In this work both the width of the gap between the electrodes and the shape of the electrodes were varied. There were seven electrode gaps, from 2 to 14 μm in 2 μm steps, and five different electrode geometries examined, which will be described in detail in Section 2.2.2.1.

2.2.2.1 Design of Test Structures

Three different types of test devices were fabricated, shown in cross-section in Figure 2.20. Type A was simply silicon electrodes with an air gap. Type B devices were coated with PDMS, cured, and then the excess PDMS was removed from the surface, resulting in test structures with a silicon and PDMS top-surface. Type C devices were coated with a single thick layer of PDMS and not planarized. The details of the fabrication are described below.

Test structures used to measure breakdown of dielectrics generally are oriented in vertical stacks, but stacking uniform structures with single micron thicknesses is not feasible when using viscous polymers like PDMS. In order to fabricate dielectric layers only micrometers in thickness, the fabrication process described below defined the PDMS thickness in-plane by molding the PDMS features. A consequence of this fabrication process is the use of silicon, a semiconductor, for electrodes. Dielectric breakdown is generally measured using metal electrodes, but the fabrication process described below was not compatible with metals.

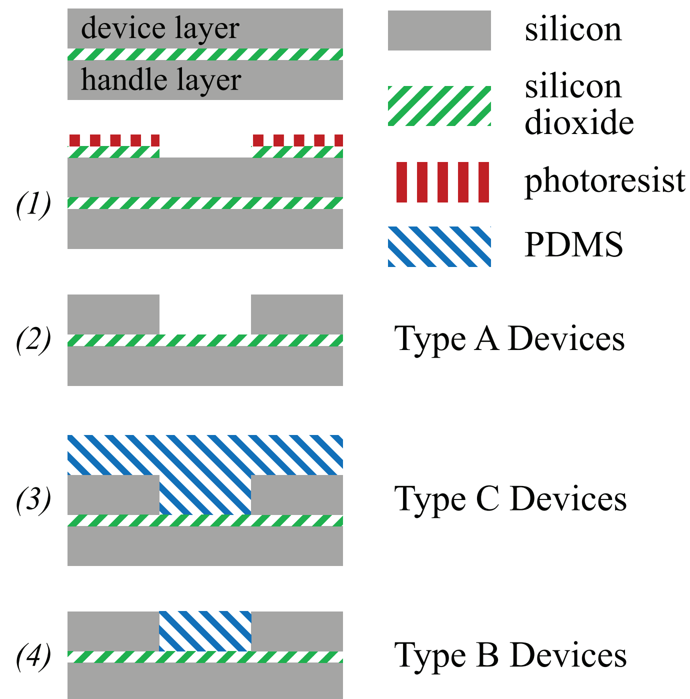

Figure 2.20: Schematic showing cross sections of the fabrication process and the three types of test structures: 2) Type A with an air gap 3) Type C coated with PDMS and 4) Type B coated with PDMS and planarized.

Each type of device was fabricated in five different style electrode geometries, shown in Figure 2.21. Style 1 had two flat electrodes. Style 2 had one flat electrode and one curved electrode. Style 3 had two curved electrodes. Style 4 had one flat electrode and one pointed electrode. Style 5 had two pointed electrodes. The electrodes were all 500 μm wide and 3 mm long. The radius of the curved electrodes was 250 μm. The pointed electrodes ended with isosceles triangles that had two leg lengths of 354 μm that met at 90° at the ends. From this point on the following naming convention will be used: a Type A device with a Style 4 geometry will be referred to as an A4 test structure, a Type C device with a Style 3 geometry will be referred to as a C3 test structure.

The thickness of the electrodes was determined by the thickness of the device layer of the SOI wafer that was used. The Type A and B devices were fabricated on SOI wafers with device layer thicknesses of 25 μm and 75 μm and device layer resistivities of 0.006-0.009 Ω-cm and 0.07-0.13 Ω-cm, respectively. These wafers both had buried silicon dioxide layer thicknesses of 2 μm and handle layer thicknesses of 400 μm. The Type C test structures were fabricated on an SOI wafer with a device layer thickness of 40 μm, buried silicon dioxide layer thickness of 5 μm, handle layer thickness of 490 μm, and device layer resistivity of 0.001-0.003 Ω-cm.

It is worth noting that these test structure designs did not test the electromechanical breakdown of the PDMS films [91], which is sometimes the case with PDMS thin films, especially ones being used for DEAs [84, 85, 86]. The electromechanical

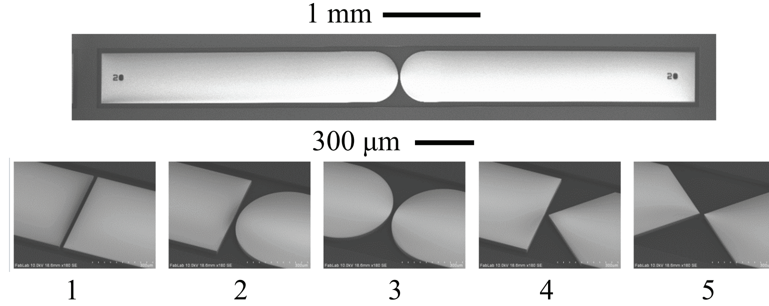

Figure 2.21: SEM images showing the five different electrode styles with 20 µm electrode gaps.

breakdown, which is typically caused by the contraction of the PDMS film due to the applied Maxwell pressure, was not being tested because the electrodes were rigidly fixed in place, so there was no contraction of the films during testing.

2.2.2.2 Fabrication of Test Structures

The fabrication for all three types of test structures began with the same processing, it was the final steps that differentiated them. A cross-section schematic of the fabrication process is shown in Figure 2.20. The fabrication began by depositing a 200 nm layer of silicon dioxide in an Oxford PlasmaLab 100 plasma-enhanced chemical vapor deposition tool (PECVD). A layer of photoresist was deposited and then patterned using an EVG 620 mask aligner. The silicon dioxide was then patterned with an Oxford PlasmaLab System 100 inductively-coupled plasma reactive ion etch (ICP-RIE) tool in Step 1.

The wafers were then diced into dies which were bonded to a handle wafer with a 15 µm layer of photoresist and etched with a Surface Technology Systems deep

reactive ion etch (DRIE) tool. The number of etch cycles performed (etch time = 10 s, passivation time = 6 s) depended on the device layer thickness; 45, 80 and 130 cycles were used for the 25, 40, and 75 μm device layer wafers, respectively. The dies were then released from the handle wafer with a solvent and the silicon dioxide mask was removed with a 1 minute dip in 6:1 buffered hydrofluoric acid (BHF) in Step 2. At this point, the Type A test structures, which had an air gap separating two silicon electrodes, could be tested.

To complete the manufacturing of the Type B and C test structures, a PDMS mixture was prepared in a 10:1 mass ratio of base to curing agent, poured over the wafer, degassed in a vacuum for 15 minutes at 50 Torr to remove the air bubbles introduced during mixing which could have affected the results, and cured on a hot-plate at 90 °C for 15 minutes in ambient conditions that ranged from 34 to 35% relative humidity. Once the PDMS was cured in Step 3, the Type C structures could be tested.

Type B devices were finished by taking dies with cured PDMS and removing the excess PDMS above the surface of the wafer with a razor blade by running it across the surface of the wafer like a squeegee in Step 4, a process described in detail in [44]. This resulted in silicon electrodes with exposed top surfaces separated by thin PDMS films. The PDMS used in all of this work is Sylgard 184 from Dow Corning, the most common type of PDMS used in microsystems.

2.2.3 Test Procedure and Results

2.2.3.1 Test Procedure

Tests were performed by applying a voltage between the two silicon electrodes with tungsten probes, shown in Figure 2.22. During testing, the voltage was slowly increased until breakdown occurred. There were four ways in which the breakdown was evident: a spike in the current draw, demonstrated in Figure 2.23, a visually noticeable destruction of the silicon, demonstrated in Figure 2.22, a drop in the supply voltage from the the current-limited power source due to a reduction of the resistance of the load, or an audible sound. Voltages were applied using a Bertan Series 230 High Voltage Power Supply.

2.2.3.2 Test Results

This section reports the results of the tests of the dielectric breakdown of the PDMS thin films. For this section, the term dielectric breakdown is defined as the voltage at which failure occurred when an increasing voltage ramp was applied to the material [92]. All of the tests were performed in ambient conditions that ranged from 38 to 40% relative humidity and 18 to 21 °Cwithin 72 hours of the PDMS being cured.

All of the results represent at least two separate test structures, but most of the results represent five devices for each style and type combination of test structure.

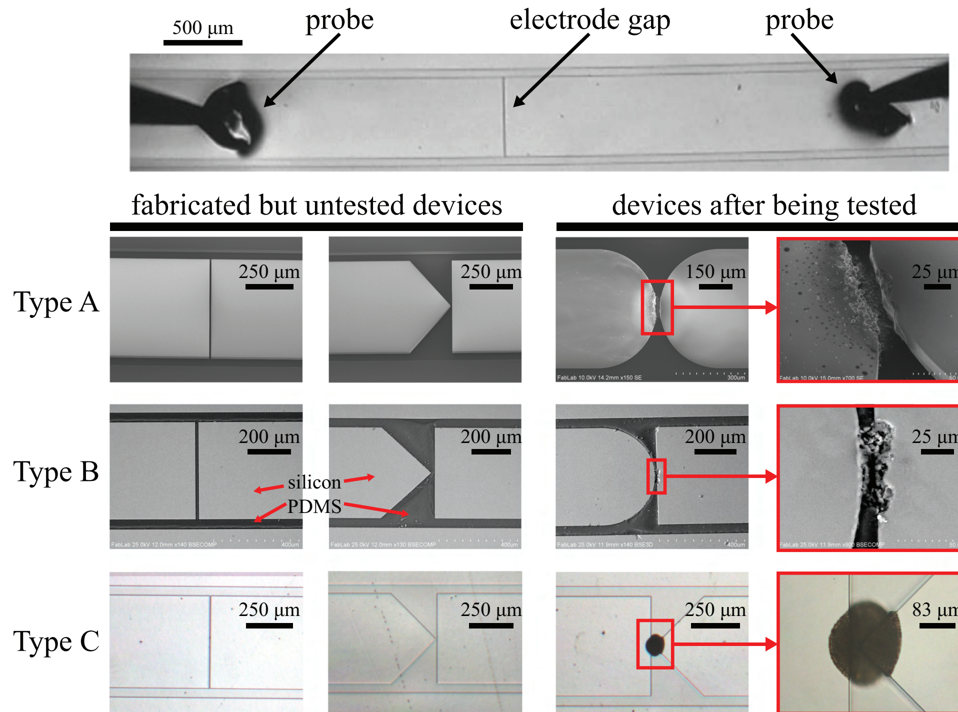

Figure 2.22: The top image is a C1 test structure with flat electrodes and a 6 μm gap before breakdown. Below that are images of Type A, B, and C devices. Columns 1 and 2 show two fabricated but untested devices. Column 3 shows a tested devices. Column 4 shows a closeup on the damage resulting from the breakdown. The Type A and B images were acquired from an SEM. The Type C images are optical micrographs.

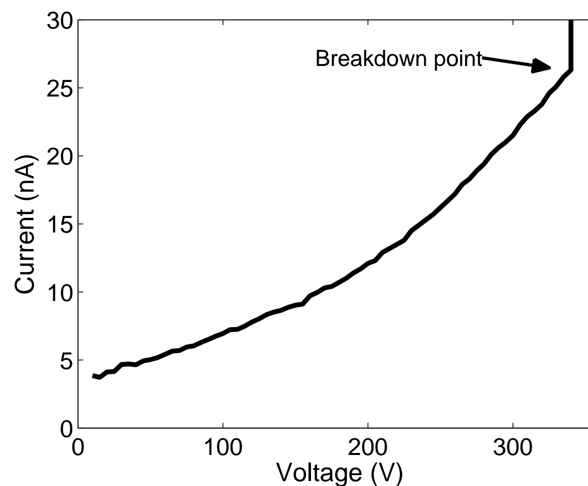

Figure 2.23: A voltage versus current curve from a test of an A1 test structure with an 8 μm air gap. At 345 V the current jumps several orders of magnitude, indicating breakdown of the structure.

The voltages were measured on a multimeter using a voltage divider in parallel with the test structure. There was also an ammeter in series with the test structures used to indicate any increase in the current draw. The electrode gap dimensions used to calculate the breakdown field were not the as-drawn gaps but rather an average of at least three measurements performed in a scanning electron microscope (SEM) for each electrode gap and each test structure geometry.

In order to confirm that the tests were in fact measuring breakdown, the Type A devices were used to measure the breakdown of air so that the results could be compared to Paschen's Law, which describes the breakdown of air [93]. Paschen's Law is valid down to approximately 8 μm, at which point it begins to deviate from experimental results. Below that, however, the behavior has been characterized experimentally [94, 95, 96, 97, 98, 99, 100].

The test results for the Type A devices are shown in Figure 2.24a, which demonstrates that the breakdown fields match well with Paschen's Law. This figure, and all the figures which plot breakdown fields as a function of electrode gap, show the breakdown according to Paschen's Law down to 4 μm [94] as well as experimental data for gaps from 10 μm down to 2 μm [96].

The results for the Type B devices are shown in Figure 2.24b and demonstrate that the breakdown fields were again similar to Paschen's Law. When compared directly to the results of the Type A devices, shown in Figure 2.24c, it is evident that the breakdown field of the Type B structures was slightly higher than that of the

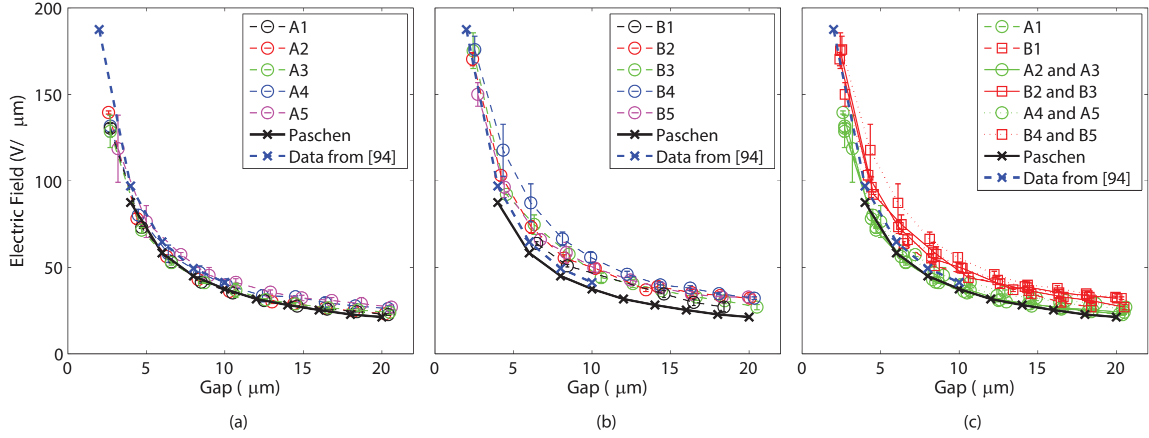

Figure 2.24: a) Breakdown of the Type A test structures b) breakdown of the Type B test structures c) breakdown of the Type A and B test structures.

Type A structures.

The results for the Type C test structures are shown in Figure 2.25. The breakdown of the devices with one or two curved electrodes, Styles 2 and 3, is shown in Figure 2.25a and the breakdown of the devices with one or two pointed electrodes, Styles 4 and 5, is shown in Figure 2.25b. A direct comparison of the different styles of electrodes is shown in Figure 2.25c.

Figure 2.25 demonstrates that the maximum gap size that was tested varied by electrode style. This was because at voltages above 4340 V, the test structures broke down through the buried silicon dioxide layer that separated the silicon device and handle layers, as opposed to breaking down through the PDMS. Figure 2.25c shows a thick black line labeled Oxide that represents the electric field at a constant 4340 V, which effectively denotes the maximum voltage that could be applied to the test structures. This limited the maximum electrode gaps which could be tested, as is

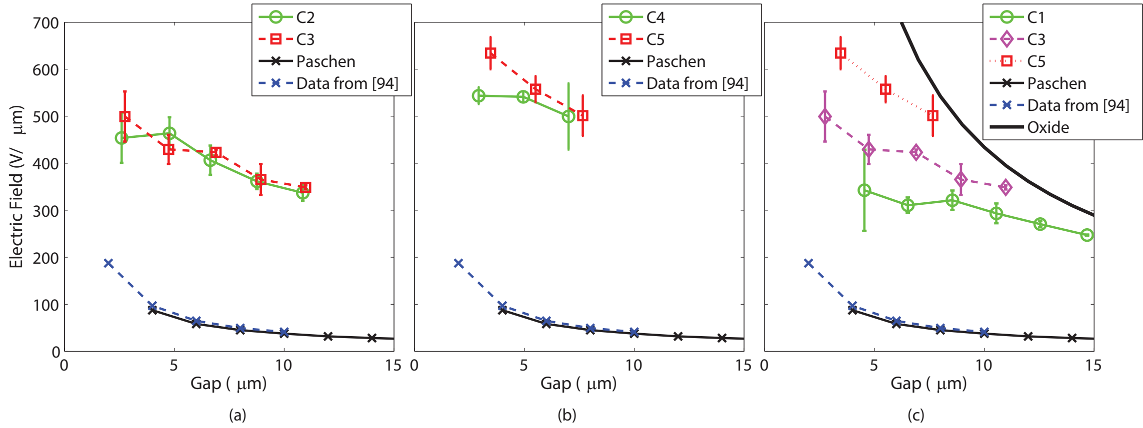

Figure 2.25: a) Breakdown of the C2 and C3 test structures b) breakdown of the C4 and C5 test structures c) breakdown of the C1, C3, and C5 test structures.

seen in the figure; Type 1 devices could only be tested up to 14 µm gaps, Type 2 and 3 devices could only be tested up to 10 µm gaps, and Type 4 and 5 devices could only be tested up to 6 µm gaps. The position of this line is a function of the particular wafer that was used in the tests. Increasing or decreasing the thickness of the buried silicon dioxide layer of the wafer would shift the curve up or down, accordingly.

2.2.4 Discussion

The results of the Type A test structures used to characterize the breakdown of air are shown in Figure 2.24. As was expected, the results closely match the breakdown of air described by Paschen's Law. It was not expected that the data would exactly match Paschen's Law as the breakdown field depends on the electrode shape and material as well as the ambient environment in which the tests were conducted. One of the side effects of using a DRIE tool to etch the silicon is scalloping, or

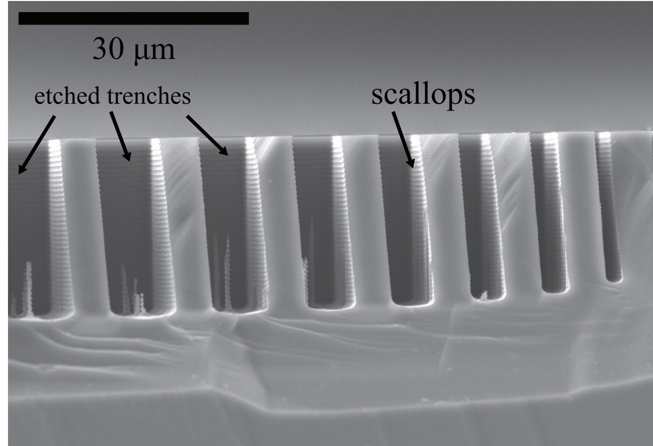

Figure 2.26: SEM image of a series of trenches etched in a silicon wafer showing the scalloping resulting from the DRIE process.

sharp points on the sidewalls of the trenches resulting from the cyclic nature of the etch process, which likely contributed to the variation of the results. A SEM image demonstrating scalloping on a series of trenches etched in silicon is shown in Figure 2.26 with a closeup of the sidewall and base of an etched trench shown in Figure 2.27.

The Type B test structure results, shown in Figure 2.24b and 2.24c, demonstrate a breakdown field that was slightly higher than the breakdown of the Type A structures. The cause of the increase is not fully understood, but is likely due to the fact that the breakdown was isolated to the surface of the wafer. In the Type A devices, breakdown could occur at any point along the depth of the test structures. In the Type B structures, however, the breakdown could only occur at the surface of the wafer due to the PDMS which filled the gaps between the electrodes and inhibited breakdown. Any damage to the surface of the electrodes during the planarization could have affected the ultimate breakdown field that was measured during testing.

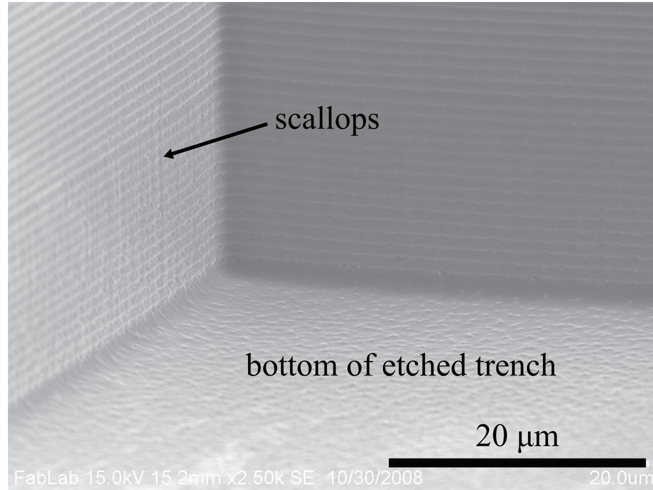

Figure 2.27: SEM image of scalloping in silicon after a DRIE process.

The results from the Type C devices demonstrate far more interesting results. Figures 2.25a and 2.25b compare the different styles of electrodes that were fabricated. Figure 2.25a shows that the breakdown fields for the Style 2 and 3 devices were similar. Additionally, Figure 2.25b shows that the breakdown fields for the Style 4 and 5 devices were similar. This suggests that the effect of having curved or pointed electrodes is accomplished by adding a single such electrode to the test structure, such as in the Style 2 and 4 structures. When the test structure had two curved or pointed electrodes, such as in the Style 3 and 5 structures, respectively, there was no significant change in the breakdown field at the gaps tested. Figure 2.25c, however, shows that changing from having two flat electrodes to having at least one pointed or curved electrode led to a dramatic increase in the breakdown field.

A similar dependence of the breakdown on the thickness of the films has been demonstrated in larger size films. It is generally accepted that the breakdown field E_B

is proportional to the inverse of the dielectric thickness t to the power of a constant n, which varies by material, or $E_B \propto t^{-n}$ [101, 102, 103]. Some have suggested that failure polymer films tested in a similar manner was a result of thermal breakdown, or an imbalance between the dissipation of heat and Joule heating from any conduction through the dielectric [77, 101].

One of the significant findings of this work is that electrode shape and gap both had a dramatic effect on the breakdown field of PDMS, which contradicts the findings for the breakdown of air. Figure 2.24 shows that the breakdown field of the Type A and B test structures had a limited dependence on the electrode shape and gap at widths above 5 μm. Figure 2.25c, however, shows that the electrode shape and gap had a large effect on the breakdown of PDMS. The breakdown fields ranged from 349 V/μm for the C3 devices with a 10 μm gap to 500 V/μm for the same devices with a 2 μm gap, demonstrating the variation with electrode gap for one electrode geometry. Additionally, the breakdown fields ranged from 343 V/μm for the C1 devices with a 4 μm gap to 541 V/μm for the C5 devices with a 4 μm gap, demonstrating the variation with electrode geometry at one electrode gap.

A comparison of the increase in the breakdown field for the Type B and C test structures relative to the Type A test structures is shown in Figure 2.28. The ratios shown in this figure were calculated by dividing the breakdown field of the Type B and C devices by the breakdown field of the Type A devices for each style of test structure. Figure 2.28 shows that the increase in the breakdown field for the Type C

test structures was much greater than that of the Type B test structures. The Type B devices had ratios of 1.1 to 1.4 and were linear over all of the electrode gap widths. The Type C test structures, however, had with ratios varying from 4.4 to 9.5. The ratios increased significantly as the electrode gaps increased, meaning the impact of the PDMS on the breakdown field increased as the electrode gap increased, relative to air.

Figure 2.28 also shows that the data for the Style 2 and 3 devices overlapped, as did the data for the Style 4 and 5 devices. The overlaps led to grouping of data for the Type C devices into three different groups with the Style 1 devices in one group, Style 2 and 3 devices in a second group, and the Style 4 and 5 devices in a third group. This again implies that the effect of curved or pointed electrodes is achieved with just a single electrode and that adding a second pointed or curved electrode does not additionally effect the breakdown field.

There are no known examples of previous work that have looked at the effect of electrode shape on the breakdown of polymers at similar length scales, though some previous work has examined the effect of the electrode shape on the breakdown of air [97]. This work demonstrates a noticeable but relatively modest relationship between electrode shape and breakdown field, which agrees with the data shown in Figure 2.24. The results in Figure 2.25 suggest that the PDMS increases the variation of the breakdown field across the electrode geometries.

It is worth acknowledging that the results of this work demonstrate breakdown

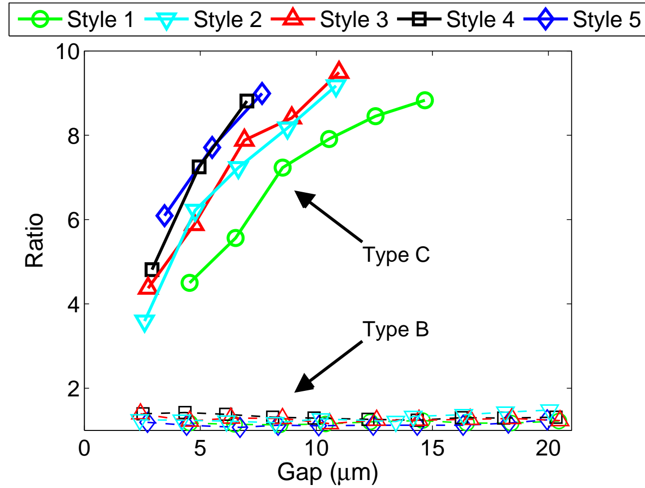

Figure 2.28: The ratio of the change in the breakdown field with respect to air as a function of gap for Types B and C.

fields that are higher than the breakdown fields typically reported for Sylgard 184 PDMS. As was mentioned earlier, breakdown results for Sylgard 184 range from 19 to 133 V/μm [60, 87, 104, 105, 106, 107, 108]. This discrepancy is most likely due to the difference between the electrode gap geometries and materials used in this work and used in other works. As the results presented above demonstrate, the breakdown field does depend on the electrode gap, and most other works used larger PDMS film thicknesses. These other works also used different electrode geometries and materials, so comparing the results directly can be deceiving. The list of citations above is not intended to be an exhaustive list; there are many other publications which mention the dielectric breakdown of PDMS. Most publications, however, simply use results from other papers as a guideline for the breakdown of PDMS. There are not any previous works that measured breakdown of sub-14 μm PDMS thin films between silicon

electrodes. The results in this section demonstrated a wide range of breakdown fields by varying electrode gap and geometry and emphasize the importance of determining the breakdown field of PDMS as it changes with the environment in which it is implemented.

2.2.5 Conclusions

This discussion described the dielectric breakdown of PDMS thin films at thicknesses from 2 to 14 μm with several electrode geometries. The results showed that while there was not a strong influence of the electrode shape and gap size on the breakdown field of air gaps, there was a strong influence for similar gaps filled with PDMS. The results show that the PDMS dielectric breakdown fields varied from 250 V/μm to 635 V/μm, depending on the electrode shape and geometry, which corresponds to a 4.4x to 9.5x increase in the breakdown field over that of air.

2.3 Conductive PDMS

While all of the polymers that have been characterized so far have been dielectrics, it is common for conductive filler particles to be added to a polymer matrix in order to create conductive PDMS. Common filler particles include silver microparticles [109], carbon black [109], exfoliated graphite [52], and carbon nanotubes [110]. All of the work presented in this dissertation used carbon black particles because it is inexpensive and readily available in particle sizes down to tens of nanometers. Carbon

black particles are about an order of magnitude less expensive than silver particles of the same size. Carbon nanotubes and exfoliated graphite are potential options in the future, but are required to be much smaller than 2 μm, the approximate size of the trenches which the particles must enter and are not readily available at this size scale.

Conductive traces have been patterned on elastomeric substrates with thin metal films [111] and wavy thin silicon films [112]. These methods, however, are not compatible with the fabrication processes that will be used for the devices described in Chapters 4 and 3, so while these methods are useful for particular applications, it is not practical for fabrication of high aspect ratio features, which is central to this dissertation.

2.3.1 Carbon Black Filler Particles

The influence of carbon black particles on rubber was discussed by Guth in the first half of the twentieth century [113]. In his paper, Guth introduces a model that describes the relationship between the modulus of a rubber and the volume concentration of a carbon black filler, shown in Equation 2.14.

$$E^{*} = E_{o}\left(1 + 0.67fc + 1.62f^{2}c^{2}\right) \tag{2.14}$$

where E_o is the unloaded modulus, c is the volume concentration, and f is a shape factor which equals the length divided by the breadth of the particles. Guth describes

three ranges of volume concentration that a carbon black and rubber sample can exist in. The first, a volume concentration of carbon black from 0% to 10%, describing the range in which there is no discernible electrical conductivity of the polymer. The second, a volume concentration of carbon black from 10% to 30%, describes the range in which the electrical conductivity of the polymer increases as the number of paths through the polymer that electrons can follow increases with volume concentration. Eventually the polymer becomes saturated by the carbon black and packing of the carbon reaches its most dense configurations, which Guth suggests is a volume concentration of carbon black over 30%. Guth does not address how particle size might influence his model or how it might shift any of these percentages.

Strictly speaking, Guth writes that Equation 2.14 should be used to describe the second range of conductive filler, volume concentrations from 10% to 30%. Guth also states that the model should be used for are rod-shaped fillers where the shape factor f is much greater than 1, not for spheres, as is the case with carbon black where f=1. However, this model can still be used as a reference for considering the affect of spherical fillers, like carbon black. Equation 2.14 shows that carbon black particles are ideal when the a low modulus material is desired. This is because when f=1, the increase in the modulus is smallest. It should be noted that assuming f=1 for carbon black is an approximation as the carbon black particles do tend to agglomerate, as opposed to individual particles suspended in the matrix material. The agglomeration was noticed visually upon inspection of the material under an optical microscope.

Materials like carbon nanotubes have f values that can be from 10^1 to upwards of 10^4 times larger, so they have a much more significant impact on the modulus of the materials. Smaller filler particles, however, require larger concentrations to achieve conductivities similar to that of larger filler particles. One of the challenges of using nanoparticles to provide conductivity to the polymers is the difficulty in uniform dispersal of the particles throughout the matrix [114, 115], but the evaluation of various mixing methods is outside of the scope of this work. Once suitable polymers were realized there was no additional work done to optimize them.

2.3.2 Characterization of PDMS/carbon

The conductive polymers were created by combining the carbon black with the polymer. The two, however, cannot be simply mixed together to result in a high quality film. This is because as increasing amounts of carbon black are added, the viscosity of the mixture increases as well. In the fabrication process detailed earlier in this chapter, a low viscosity pre-cure polymer mixture is required in order to successfully refill the silicon trenches. To mitigate this issue, solvent can be added in order to decrease the viscosity of the mixture and facilitate mixing. Then, during the curing process, the solvent evaporates, resulting in a PDMS and carbon black composite.

There is a strong dependence on the conductivity of the resulting material, as is shown in Figure 2.29. The data shown here is collected from samples with varying

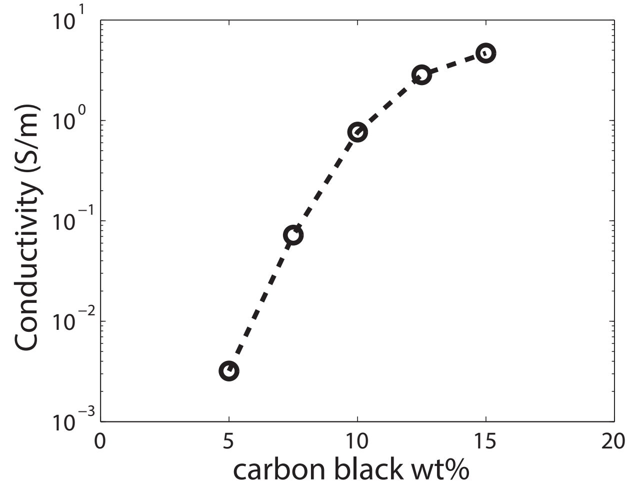

Figure 2.29: Conductivity of the PDMS/carbon as a function of weight percentage of carbon black. Note the log scale on the y-axis.

amounts of carbon black relative to the amount of PDMS. The solvent used was hexane and was a constant 20x the mass of the carbon black in the solution. The filler particles used in these tests were 39724 carbon black from Alfa Aesar which was mixed with the polymer Sylgard 184 PDMS. This data shows that the conductivity varies more than three orders of magnitude, depending on the amount of carbon black added to the solution. At 2.5 wt.% carbon black the tool being used to measure the resistance of the devices indicated an open circuit, meaning the sample resistance was greater than 200 MΩ.

It is worth noting that adding solvents to the polymer and carbon mixture is not without consequence. The influence of solvents on polymers like silicones has also been widely studied [116, 117, 118, 119]. Most of these studies focused on determining the affect of the solvents on the crosslinking density and organization of the crosslink

networks. There is some discrepancy between published work, however. Some papers claim that the solvents decrease the final crosslinking density, while others claim that the crosslinking density is maintained but the length of the polymer chains between crosslinks increases with increased solvent. The former would lead to a decrease in the modulus of the material, as the modulus has been shown to be linearly dependent on the crosslink density. The latter considers what is called "supercoiling" [120, 121]. This is when the polymers form crosslinks in the presence of the solvent and then contract as the solvent evaporates. When the solvent has evaporated, the chains of the polymer have contracted into ordered coils. The resulting decrease in entanglements and supercoiling lead to a decrease in the modulus of the polymers and an increase in the ultimate strain and strain crystallization.

One of the issues with using carbon black as the conductive filler in PDMS is that the conductivity of the films was also very sensitive to strain. The effect has been widely reported and hinders the use of carbon black and PDMS films in strain sensor application that require reasonably fast response times [122]. Any perturbation of the films created using this combination led to a dramatic change in the conductivity and had a settling time on the order of hours. To demonstrate this, a sample of PDMS/carbon was strained to 100% and was then relaxed. Figure 2.30 shows the response of the resistance as a function of time during the relaxation. The dashed horizontal red line shows the resistance prior to the sample being strained. This general type of decay in the resistance over time was seen regardless of the strain.

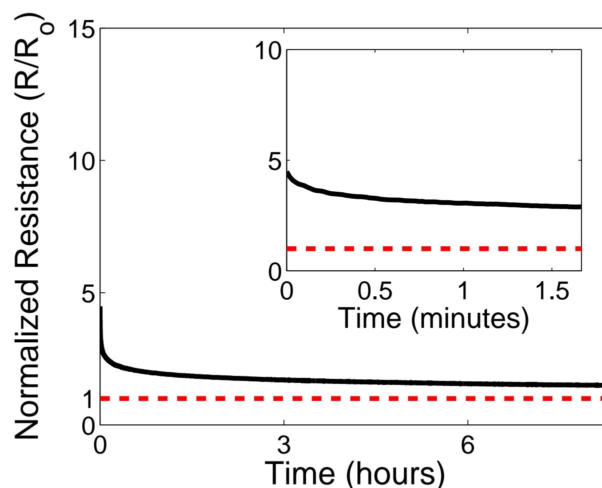

Figure 2.30: Resistance as a function of time during relaxation for a PDMS/carbon sample that was strained to 100% and relaxed. The dashed horizontal red line shows the resistance of the sample prior to being strained.

The samples are very sensitive to changes in strain but take a long time to return to their initial value.

In addition to the electrical properties, the mechanical properties of the polymer filled with carbon black are also important to characterize, especially how adding the carbon black particles effects the modulus of the polymer material. In order to examine this, three macroscale samples were prepared and tested in a DMA. In this work, the polymer MRTV-9 from Insulcast was used. This polymer was used because it has a lower viscosity than the Sylgard 184 PDMS, which aids the mixing with the carbon black particles. Three samples were prepared: the unfilled MRTV-9, MRTV-9 mixed with an equal amount of hexane, and MRTV-9 mixed with an equal amount of hexane and 7% carbon black particles by weight. The MRTV-9 and MRTV-9 and hexane samples were mixed by hand. The samples with carbon black were prepared

by first mixing the hexane and carbon black with a magnetic stir bar for several hours and then for several additional hours after the MRTV-9 was added to the mixture. The samples were then poured into polyoxymethylene molds and cured at 120 °C.

Once the samples were prepared, they were tested in a dynamic mechanical analyzer. The results of the tests are shown in Figure 2.31. The results show that adding hexane to the MRTV-9 lowered the modulus but adding carbon black and hexane to the mixture increased the modulus. Fits to the linear Hooke material model return coefficients of 0.27 MPa for the MRTV-9 sample, 0.23 MPa for the MRTV-9 and hexane sample, and 0.62 MPa for the MRTV-9, hexane, and carbon black sample. The decrease and increase of the modulus was expected, as discussed earlier in this section. The Guth model predicts that a 7% by weight concentration of carbon black, or 15% by volume, would lead to an increase in the modulus from 0.23 MPa for the MRTV-9 with hexane to 0.25 MPa for the MRTV-9 with hexane and carbon black. This is much lower than the increase in the modulus that was actually seen, but this is likely because the Guth model was developed for use with materials with a high aspect ratio such as carbon nanotubes, not carbon black which has an aspect ratio of 1, assuming perfectly round particles.

2.4 Conclusions

This chapter has presented the mechanical and electrical characterization of polymers fabricated in SOI wafers for MEMS applications. The results show that the

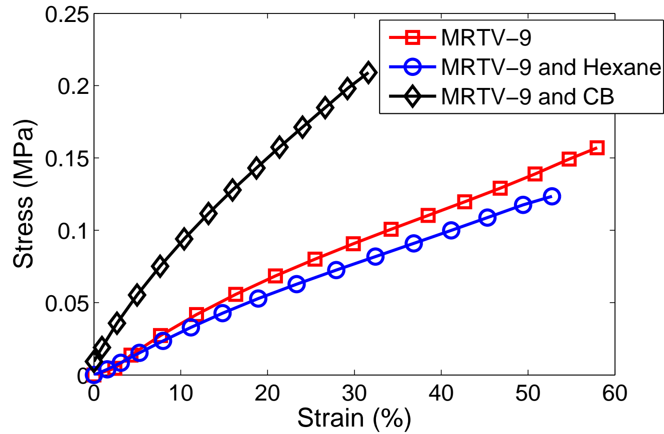

Figure 2.31: Stress-strain curves for three types of MRTV-9 samples.

polymer materials can be integrated into semiconductor processes without adverse effect on the material properties. PDMS features can be molded in high aspect ratio silicon features and achieve strains upwards of 100%. Tests of the dielectric breakdown of PDMS showed a large increase in the breakdown fields at small gap sizes over the breakdown fields of previously published works at larger gap sizes. This chapter has also demonstrated how carbon black filler particles can be added to PDMS to create conductive polymers. Throughout the rest of this dissertation, the materials described in this section will be used to create various components for microrobots such as actuators in Chapter 3 and actuated systems in Chapter 4.

Chapter 3

All-Polymer Actuators

The previous chapter described the electrical and mechanical characterization of PDMS fabricated in silicon. This chapter describes the use of the polymers described in microscale thermal and electrostatic thermal all-polymer actuators. Section 3.2 of this chapter is based on the publication "Microfabrication of compliant all-polymer MEMS thermal actuators" from volume 122 of *Sensors and Actuators A: Physical*, pages 16 - 22, by A. P. Gerratt and S. Bergbreiter, published in 2012. Section 3.3 of this chapter is based on the publication "Batch fabricated bidirectional dielectric elastomer actuators" in the proceedings of the *International Conference on Solid-State Sensors, Actuators, and Microsystems (Transducers)*, pages 2422 - 2425, by A. P. Gerratt B. Balakrisnan, I. Penskiy, and S. Bergbreiter, presented in June 2011. All of the work included in this chapter was performed by Aaron Gerratt. Co-authors Bavani Balakrisnan and Ivan Penskiy gave input on the design of the dielectric elastomer actuators described in Section 3.3.

3.1 Fabrication

The actuators demonstrated in this chapter are all-polymer MEMS devices. The microfabrication process described in this section is an extension of the silicon and

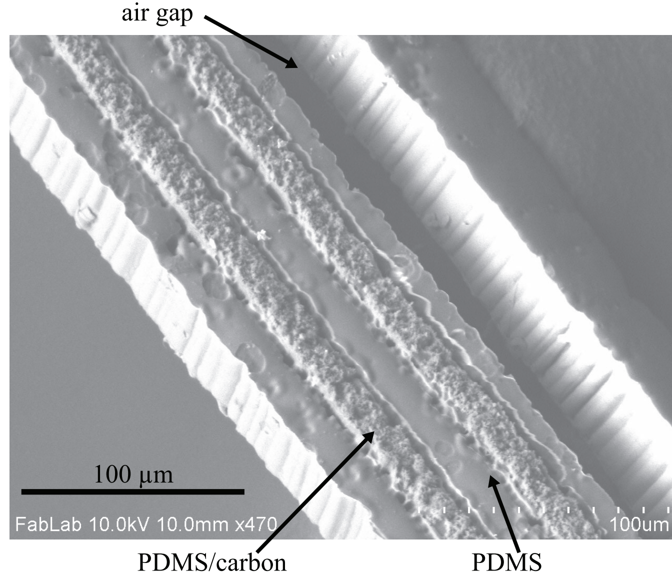

Figure 3.1: 20 μm PDMS and conductive-PDMS features fabricated together in-plane.

polymer microfabrication process shown in Chapter 2. This section presents a manufacturing process that allows for both conductive and dielectric polymer structures within the devices, which can provide interesting benefits and possibilities beyond the capabilities of devices that are fabricated with silicon. The essence of the process includes etching sets of trenches in a silicon wafer and using these trenches to mold different polymer layers together, such as in the device shown in Figure 3.1.

3.1.1 Fabrication Process

The fabrication process is detailed in Figure 3.2. The process began with the deposition of 200 nm of silicon dioxide on a bare 500 μm thick silicon wafer. A 1.4 μm photoresist layer was patterned with photolithography and the pattern was

transferred to the oxide layer with a brief etch in 6:1 buffered hydrofluoric acid (BHF). This was followed by a 40 μm deep reactive ion etch (DRIE), shown in step 1 (steps correspond with Figure 3.2). A one minute oxygen plasma clean was then performed to remove any residual passivation from the DRIE etch.

A composite with a PDMS matrix and carbon black particle filler was then prepared. The PDMS was prepared in a 10:1 ratio of base:curing agent. The carbon black used in this work was Vulcan XC72-R from Cabot [123]. The PDMS/carbon composite was 82.5 wt% PDMS and 17.5 wt% carbon black particles. The polymer was prepared using the fabrication process described in Section 2.3.2.

After curing, the excess PDMS/carbon was manually planarized to the surface of the wafer with a razor blade. A 60 second etch in 3:1 tetrabutylammonium fluoride (TBAF) and n-methylpyrrolidone (NMP) was performed to remove any remaining PDMS/carbon residue [59]. This was followed by a brief 6:1 BHF etch to remove the oxide mask. A low-temperature (100 °C) plasma enhanced chemical vapor deposition (PECVD) silicon dioxide was deposited and patterned for a second DRIE in step 3. Following the DRIE, a 20 second SF_6 isotropic dry silicon etch was performed to remove any residual silicon that may have survived the DRIE along the sidewalls of the PDMS/carbon.

This second set of trenches was refilled in step 4 with PDMS, which was manually planarized in the same manner as the PDMS/carbon. In steps 5 and 6, the wafer was bonded, topside down, with Cool Grease from AI Technologies to a handle wafer

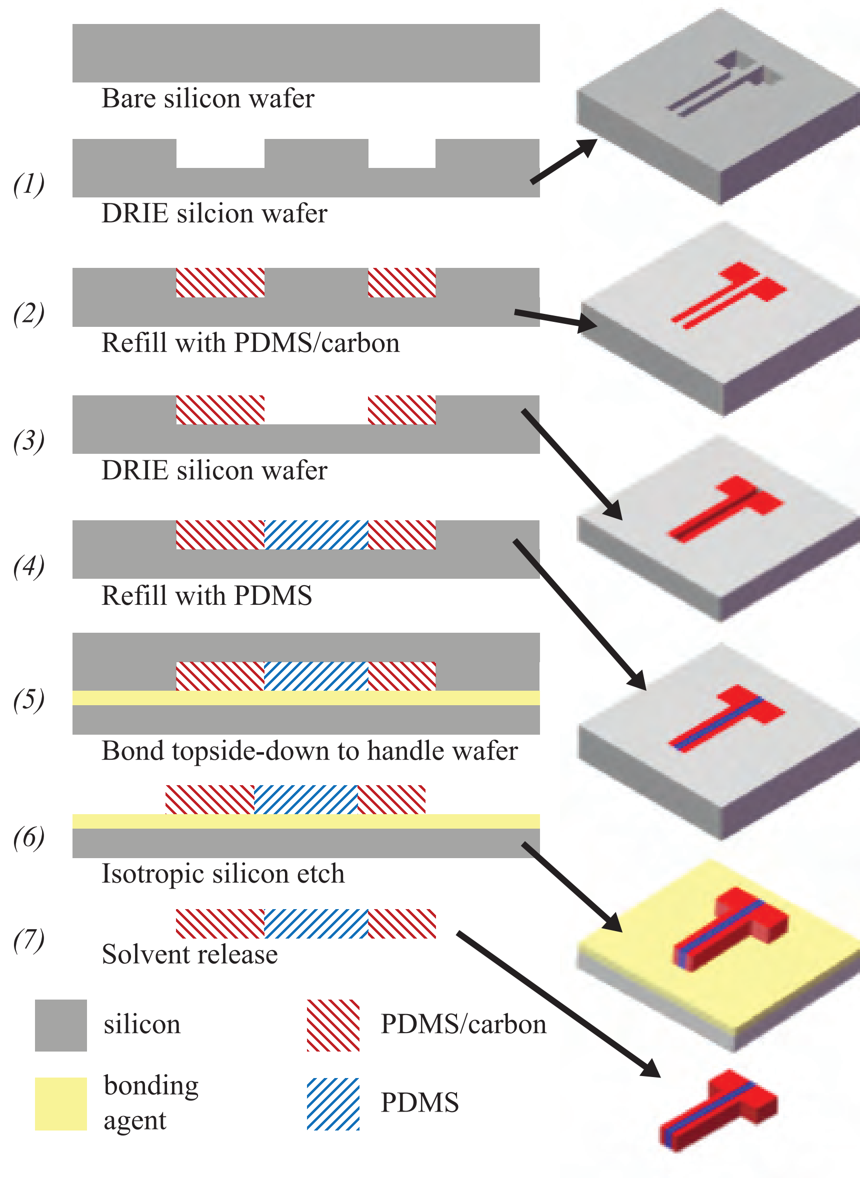

Figure 3.2: Perspective and cross section views of the microfabrication process. Gray is the silicon, light yellow is the bonding agent, red is the conductive polymer, and blue is the dielectric polymer.

and an SF_6 plasma isotropic dry silicon etch was performed to remove the exposed silicon. In step 7, an acetone soak and ultrasonication was used to release the devices from the handle wafer. Finally, a brief etch in 6:1 BHF was performed to remove the remaining oxide mask.

3.1.2 Fabrication Results

One of the main benefits of this fabrication process is the ability to pattern very thin films of both conductive and dielectric polymer layers. Polymer layers are often spin coated to achieve uniform films [89]. The film thickness to spin speed relationship is highly non-linear and generally asymptotically approaches some minimum thickness, which depends on the specific polymer being processed and the substrate material [124]. As the film thickness approaches this minimum, the thickness uniformity of the PDMS decreases as well. This is especially true when filler particles such as carbon black are added. Such filler particles have dramatic implications on the uniformity and minimum thickness of films that can be achieved through spin coating [125].

The benefit of the process presented above is that the films are all patterned with a molding process, so there is no spin coating of the pre-cure polymer films. This means that a wide variety of feature sizes can be patterned, even multiple feature sizes on the same wafer. This molding technique has been used to fabricate feature sizes from 2 μm to several millimeters in length and width [44]. Feature sizes from 20 μm

to 1 mm have been fabricated at the same time on one silicon wafer. Additionally, the depth of the features depends only on the depth of the DRIE during the fabrication and depths from 5 μm to 40 μm have been achieved. In this chapter, the feature sizes ranged from 10s to 1000s of microns in width and were all 40 μm in depth.

In the process presented in this section, the PDMS/carbon was deposited before the PDMS was deposited. This helped to prevent any electrical shorting in the devices. During deposition of the second polymer layer, any non-uniformities on the top surface of the PDMS/carbon layer were filled in with PDMS. If the PDMS were deposited first followed by PDMS/carbon, the non-uniformities would be filled with the conductive PDMS/carbon, which could potentially short the devices.

One issue with this fabrication process is that some of the devices had large residual stresses after fabrication, though this varied across the wafer. It is likely that this came from the reaction between the polymer and the SF_6 plasma during the DRIE etch cycle, coupled with inadequate cooling from the handle wafer. It was observed that soaking the devices in 18:1 buffered hydrofluoric acid for several hours helped to relieve some of the residual stresses, though the exact mechanism is not yet fully understood. It is possible that the BHF removed a thin oxide layer on the surface of the PDMS that was generated during the plasma etch cycles during the DRIE [126].

Attempts were also made to use 2.3 μm silver particles as a conductive filler material, but the PDMS/silver films did not survive the final isotropic silicon etching

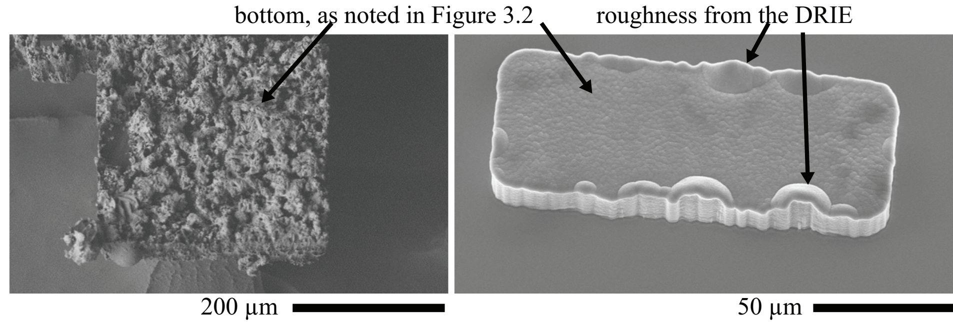

Figure 3.3: PDMS films with silver (left) and carbon black (right) filler particles. The surface roughness of the silver sample was a result of the reaction with the SF_6 plasma during the isotropic etching process while the surface roughness of the carbon black sample was a result of the non-planar silicon trench surface from the DRIE that were transferred to the PDMS/carbon during the molding process.

process. The silver particles reacted more strongly with the silicon etch than the carbon black. Other than the residual stress in the PDMS/carbon, there were no other adverse affects of the isotropic silicon etch on the PDMS/carbon films that were observed. The PDMS/silver, however, became highly porous and greatly increased the resistivity of the PDMS/silver films. A visual comparison of the silver and carbon black films after the isotropic silicon etch is shown in Figure 3.3. This figure shows the highly porous nature of the surface of the PDMS/silver as a result of the isotropic silicon etch. The surface of the PDMS/carbon sample was also slightly non-uniform, but this was due to the surface roughness at the bottom of the silicon trenches prior to the deposition of the PDMS/carbon; it was not a result of the final isotropic silicon etch.

3.2 All-Polymer Thermal Actuators

Microfabrication processes that integrate non-traditional MEMS materials such as polymers have recently garnered increased attention in part due to material properties that are significantly different from traditional materials like silicon, oxides, and metals [35]. Silicon is an anisotropic material with a Young's modulus between 130 and 188 GPa [28] and a coefficient of thermal expansion (CTE) of $2.9\text{x}10^{-6}$ 1/K [127]. For some applications, however, it is beneficial to have materials with a Young's modulus that is many orders of magnitude smaller than silicon along with a CTE that is several orders of magnitude larger. Large displacement thermal actuators in particular could benefit from such a combination. Parylene C has a Young's modulus of 2.76 GPa and a coefficient of thermal expansion similar to silicon of $3.5\text{x}10^{-6}$ 1/K [36]. Compliant elastomers such as PDMS have a Young's modulus on the order of 1 MPa and a coefficient of thermal expansion of $310\text{x}10^{-6}$ 1/K (two orders of magnitude above silicon) [128].

There are prior works that integrate mechanical polymer layers in MEMS devices for actuation. These works employ fabrication methods that typically require large feature sizes [129, 130], rigid structural layers (silicon, SU-8) [27] or serial processing and manual assembly of messy carbon grease layers [131]. There are also examples of works that exploit the difference in the coefficient of thermal expansion between silicon and polymeric materials such as SU-8 to demonstrate actuation dur-

ing heating [27]. These devices, however, are limited in their displacements because of the high modulus of silicon. Other work achieved bending by using metal traces patterned on polyimide to create asymmetric expansion of polyimide-filled v-shaped groves [16]. Devices that use rigid materials with different coefficients of thermal expansion, however, have issues with delamination at the interface of the two materials [132]. The devices demonstrated in this dissertation require no rigid structural materials and are made entirely of polymers, which allows for very robust actuators with large achievable displacements.

PDMS is a good material choice to achieve these large displacements, due to its high achievable strains in excess of 100% [51]. PDMS, however, is a dielectric material and to design actuators it is beneficial to have conductive traces that can also undergo such large strains. Many attempts to integrate conductive materials with compliant polymers use thin metal layers, such as gold, but these devices can only survive relatively small strains [41]. Conductive filler particles such as silver [133], carbon black [134], and exfoliated graphite [52] have been used to create conductive PDMS. In this work, carbon black was used because it results in films with only moderately altered mechanical properties with very inexpensive and simple fabrication.

3.2.1 Thermal Actuator Design

There are three common types of silicon-based thermal actuators: chevron [135], heatuator [27], and bilayer [136]. Polymer versions of these actuators are shown in

Figure 3.4. These actuators are powered with Joule heating by running a current through the conductive traces. Thermal actuators are ideal in applications where the electrical power requirements are not strict, as thermal actuators generally have low efficiencies. Thermal actuators can be beneficial in applications that require large forces [135] and in situations where large currents but not large voltages are available from the control electronics. One issue with these devices was that the resistance of the actuators was typically on the order of 100s of kΩ to 10s of MΩ. Since the heat production is determined by the applied power, this meant that high voltages (as high as 150 V) were needed at higher currents in order to satisfy Ohm's law. Other conductive polymer mixtures have shown lower resistivities and could be used in future process iterations [52, 133, 134].

As was discussed earlier, the CTE of PDMS is 310x10^{-6} 1/K and the CTE for silicon is 2.7x10^{-6} 1/K. Carbon black filled silicones were shown to have a CTE that was decreased by approximately the same percentage wt% of carbon black that was added [137]. The PDMS/carbon in this work was 17.5 wt%, so the PDMS/carbon CTE is approximately 82.5% of the CTE of pure PDMS, or 256x10^{-6} 1/K. This agrees with rudimentary tests that were performed by placing long strips of PDMS and PDMS/carbon on a hotplate and optically monitoring the change in length as the temperature of the hotplate was increased in steps. It is partly this large CTE that makes PDMS an attractive material for thermal actuators. Thermal strain can be calculated as where is the CTE and is the temperature change. So, a 50 °C change

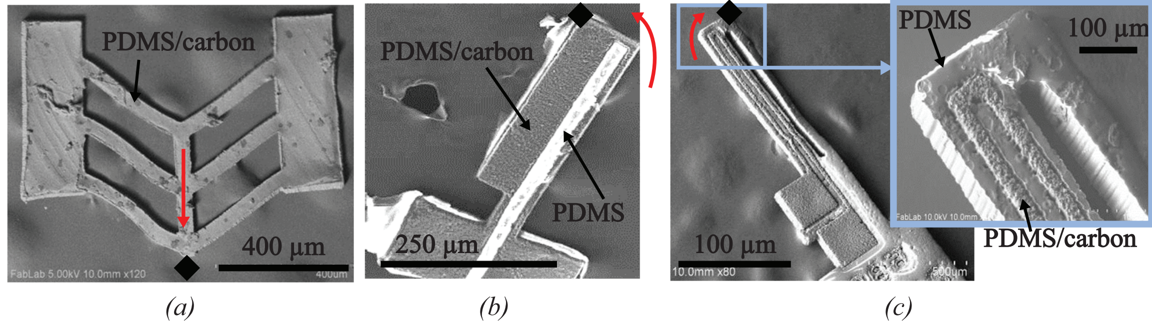

Figure 3.4: SEM of a) chevron b) heatuator and c) bilayer thermal actuators. The blue arrows show the direction of actuation. The black diamond indicates the point at which the displacements were measured on each actuator.

results in 15 millistrain in PDMS and 0.14 millistrain in silicon; PDMS strains are 100x those in silicon. However, the Young's modulus of PDMS, as shown in Section 2.1.4.2.2, is approximately 1.68 MPa. Since the force scales with the modulus of the material, this low modulus will result in a lower output force.

3.2.2 Experimental Results

Two tests were run to characterize the actuators. The first test analyzed the static free displacement of the actuators. A probe station was used to apply power to the actuators with tungsten probe tips contacting electrodes that were patterned at the base of each type of actuator. The power applied to the actuator was increased in steps, with optical images taken at each step. The power was applied at a constant voltage at each step. The second test analyzed the output force of the actuators. A vertical tungsten wire (1.3 mil wire from Gaiser Tool Company) was placed at the end of the actuator, as shown in Figure 3.5. In the equilibrium position, the tungsten wire

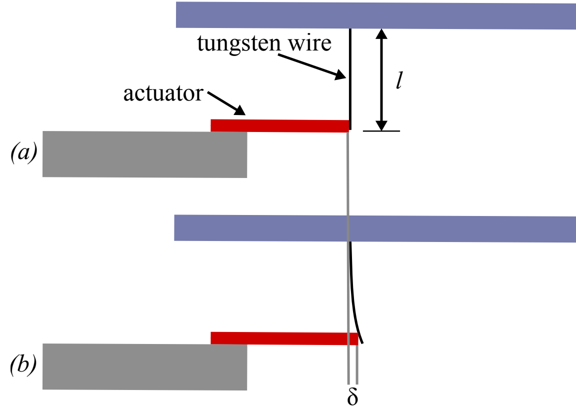

Figure 3.5: Schematic of the force-displacement characterization setup. In 3.5a, the equilibrium state of the system is shown. In Figure 3.5b, the heated state of the system is shown. The expansion of the actuator bends the tungsten wire, which is used to calculate the applied force.

was aligned vertically in front of the actuator, as shown in Figure 3.5a. The power applied to the actuator was increased in steps, leading to Joule heating and expansion of the actuator. This expansion exerted a force on the tungsten wire, bending the tungsten wire, as shown in Figure 3.5b. Optical images such at those shown in Figure 3.6 were taken at each step as the input power was increased.

After the testing was completed, the images were analyzed to measure the displacement of the tip of the tungsten wire as a function of the input power. The physical and geometric parameters of the tungsten wire were known. The analysis assumed the wire diameter had a uniform cross section, homogeneous mechanical properties, that it was rigidly fixed at the base, that the displacement was small enough that beam theory was still valid ($l >> \delta$), and that any thermal energy conducted into the tungsten wire did not alter any of its mechanical properties. The force-displacement relationship follows simple beam theory [138]:

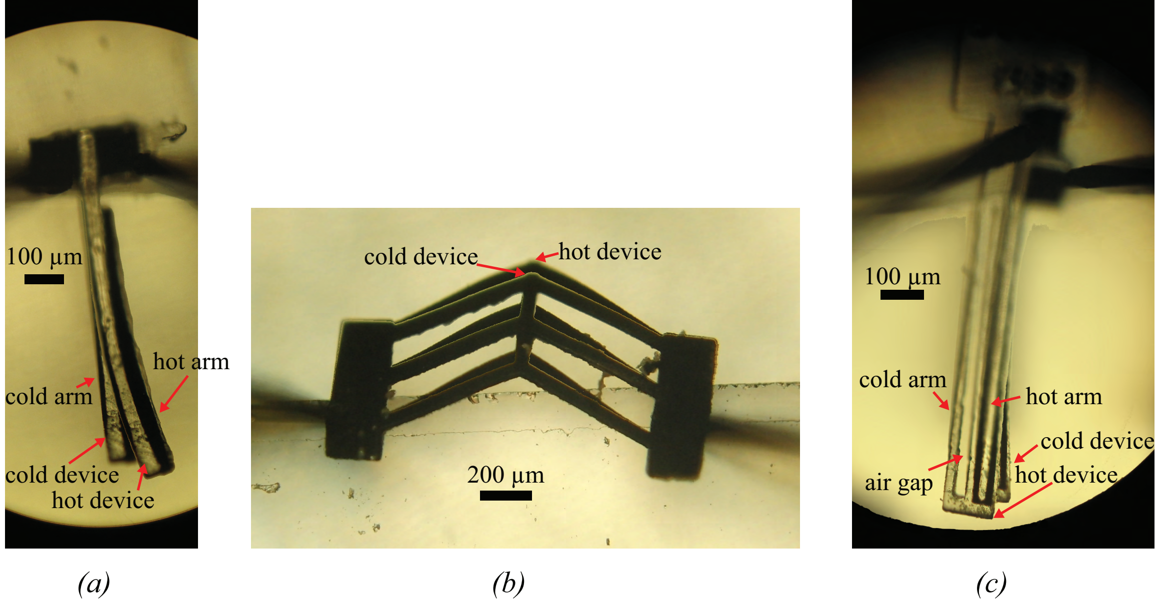

Figure 3.6: Overlaid images of hot and cold *(A)* heatuator actuators *(B)* chevron actuators *(C)* bilayer actuator.

$$F = \frac{3EI\delta}{l^3} \tag{3.1}$$

where E is Young's modulus of the wire (411 GPa [139]), I is the area moment of inertia (58200 µm^4), δ is the displacement of the tip of the wire, and l is the length of the wire (4.5 mm). It should be noted that since this method of measuring the force allowed the actuator to expand, the blocked force was not being measured; the measured force was something less than the blocked force. It should also be noted that this setup was not calibrated, so the accuracy of the measurement is unknown. The forces calculated using the method are approximate, but provide a good estimate of the magnitude of the forces.

3.2.2.1 Thermal Actuator Performance

The results of the actuation tests varied from device to device and typical results are shown. This was largely due to variations in the resistivity of the actuators, likely resulting from the hand mixing of the PDMS/carbon mixture. The residual stress also likely contributed to variations in the performance of the actuators. Figure 3.7 shows the free displacement as a function of the input power and Figure 3.8 shows the force as a function of the input power. The tests were performed as described above. For the bilayer and heatuator actuators, the displacement was determined by measuring the motion of the top right and left corners, respectively, as shown in Figure 3.4. It should be noted that all three styles of actuator are presented on one graph, but the performances should not be used to directly compare the actuators as differences such as resistance and footprint were not compensated for. The results are presented together, but are best interpreted separately. The thermal expansion at elevated temperatures led to effective strains up to 5% at the highest temperatures.

A comparison of the polymer thermal actuators can be made with silicon thermal actuators [135]. This example of a silicon chevron actuator demonstrated at least 6.7 mN at 3W with a size of 2.1 mm x 2.5 mm. The thermal actuator demonstrated in this work exerted 30 μN at 80 mW with a size of 1.5 mm x 1.2 mm. The silicon based chevron actuator had a force density of 1.3 kN/m^2 and a power density of 571 kW/m^2. The PDMS based chevron actuator had a force density of 16 newton/m^2 and a power density of 44 kW/m^2. So, the force output of the silicon based device was

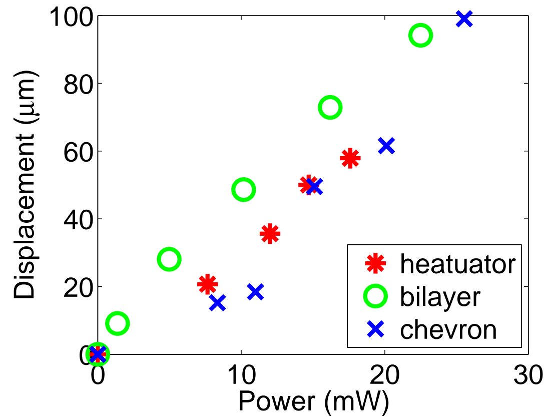

Figure 3.7: Displacement as a function of input power.

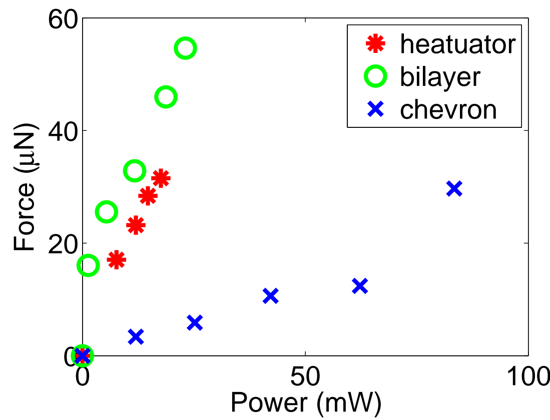

Figure 3.8: Force as a function of input power.

higher, but power density of the polymer based devices was lower. Additionally, the free displacement of the PDMS actuator was much greater than the free displacement of a similarly sized silicon thermal actuator since this displacement is proportional to the CTE of each material.

3.2.2.2 Frequency Response

The frequency response of a chevron actuator was measured by applying a square wave with a frequency of 0.005 Hz to 12 Hz. High speed video of the actuation was taken at 300 frames per second. The displacement amplitude between the power on and power off states was considered to be the displacement for the given frequencies. It should be noted that at higher frequencies the actuators did not cool completely to their equilibrium position. The normalized frequency response is shown in Figure 3.9. At lower frequencies the actuators had time to completely heat and cool during each cycle so the response is frequency independent. As the frequency increased above 1.25 Hz, the amplitude of the displacement decreased by approximately 16 dB per decade. Bilayer actuators showed a faster time response and operated at 90% of their static free displacement at 10 Hz. The difference between the performances of the two actuators is largely due to the difference in the thermal mass between the two actuator types.

3.2.2.3 Robustness

One of the benefits of using compliant polymers is their ability to absorb energy when deformed by an external force and release this energy to return to their original position when the external force is removed. As shown in Figure 3.10, the actuators can be manipulated by straining and bending, and when they are released, they return

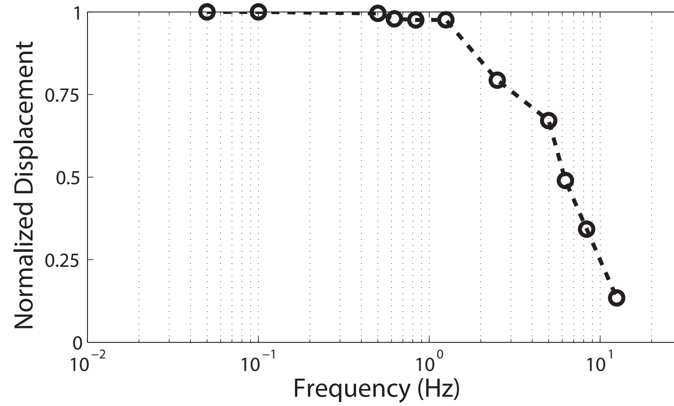

Figure 3.9: Frequency response of the displacement amplitude during actuation.

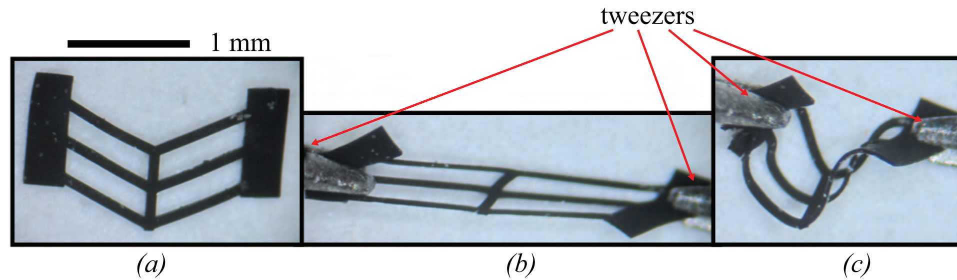

Figure 3.10: A chevron-type actuator in three states a) as fabricated b) strained by tweezers and c) bent out of plane by a pair of tweezers.

to their original shape and can be re-used. This is the case for any deformations that do not exceed the elastic strain limit of the PDMS and PDMS/carbon.

3.3 All-Polymer Electrostatic Actuators

One of the drawbacks of the thermal actuators described in the previous section is the relatively large electrical power draw, which was on the order of milliWatts. This is due to the low efficiency of the thermal actuators. This section will focus on the development of dielectric elastomer actuators (DEAs), which offer the potential

for operation at powers several order of magnitude lower than that of the thermal actuators.

DEAs are fabricated using elastomeric materials and are lightweight, compliant, robust, and have relatively high power densities [85, 140, 141]. These properties make DEAs attractive for biomimetic applications including artificial muscles [85]. Additional applications of DEAs include lightweight actuators for space exploration [142] and in biomedical MRI-compatible systems [143]. There are many examples of macroscale DEAs, but microscale DEAs are still difficult to realize because of complications with the fabrication process [82, 125, 144].

The major focuses of current DEA research are improving mechanical and electrical properties of the materials, fabricating actuators that are resistant to electrical failure, and reducing the operating voltages [85, 140, 141]. DEA materials have typically been limited to silicone and acrylic for the dielectric layer of DEAs and carbon grease for the electrodes [145]. There has been extensive research on the use of nanoparticles for increasing the dielectric constant of these materials, but this also typically leads to a decrease in the breakdown voltage [125, 146]. Nanoparticles are also used as filler particles in the elastomer matrices to create conductive elastomers. Research in this area is focused on increasing the conductance of the composites without altering the mechanical properties [52, 82, 129, 130]. The last thrust in DEA research is on reduction of the operating voltage, mainly by decreasing the dielectric layer thickness. Fabrication processes commonly used allow for film thicknesses down

to 10s of microns. DEAs are typically operated at 10s or 100s of volts per micron, so operating voltages are often many kilovolts [141, 147] resulting in actuators that are difficult to integrate into larger systems.

Prior works have been successful at demonstrating DEAs using microfabrication techniques, but still have not made significant progress in decreasing the actuation voltage of DEAs. There has been some work into surface micromachining DEAs, but these actuators have not yet been successfully operated [148]. A microfabrication process using ion-implantation of gold particles into thin films of dielectric elastomers has been used to demonstrate microscale membrane DEAs, but the devices require a differential pressure on the membrane to operate [82]. Additionally, work has been done to demonstrate microscale DEAs using conductive grease as the electrode material [129, 130]. Conductive grease, however, is messy and is not robust compared to other macro-scale electrodes.

The research described in this section use the same fabrication process used for the thermal actuators in Section 3.2 to fabricate DEAs plus one additional step added to the end of the processing. This was a several hour soak in 18:1 buffered hydrofluoric acid. The purpose of this soak was to remove any oxides that may have developed on the actuators. The elastomer used in these actuators was not Sylgard 184 but rather MRTV-9, which was characterized in Section 2.3.

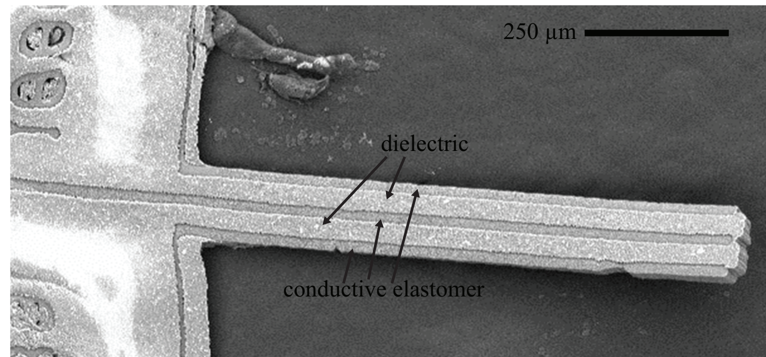

Figure 3.11: A microfabricated bidirectional DEA with alternating conductive and dielectric layers.

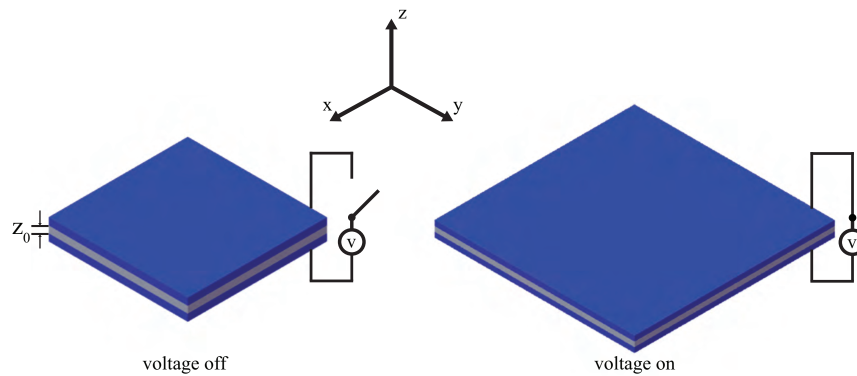

Figure 3.12: A DEA without and with a voltage applied. The top and bottom blue layers are the electrodes and the gray middle layer is the dielectric.

3.3.1 Analysis of Dielectric Elastomer Actuators

The derivation of the compressive force in a single DEA unit (two electrode layers and one dielectric layer, shown in Figure 3.12) is presented in this section. This analysis will neglect the effect of the electrode layers and of the boundary conditions on the performance of the actuators (assume a modulus/thickness of zero) and is similar to the analysis presented in [67]. This other analysis derives the force, pressures, and pull-in strains. The analysis is extended in this dissertation to describe the pull-in voltages.

The capacitance of a single actuator is

$$C = \varepsilon_0 \varepsilon_r \frac{A}{z} \tag{3.2}$$

where ε_0 is the relative permittivity, ε_r is the dielectric constant of the dielectric material, A is the overlapping area of the electrodes, and z is the thickness of the dielectric layer, as shown in Figure 3.12. The force can be determined using Equation 3.3

$$F_e = -\frac{\partial U}{\partial z} \tag{3.3}$$

where

$$U = \frac{1}{2}\frac{Q^2}{C}. \tag{3.4}$$

By substituting Equations 3.4 and 3.2 into Equation 3.3 we see that

$$F_e = \frac{\partial U}{\partial z} + \frac{\partial U}{\partial A}\frac{\partial A}{\partial z} \tag{3.5}$$

which can be solved to show

$$F_e = \frac{1}{2}\frac{Q^2}{\varepsilon_0\varepsilon_r A} - \frac{-1}{2}\frac{Q^2 z}{\varepsilon_0\varepsilon_r A^2}\frac{-A}{z} = -\frac{1}{2}\frac{Q}{\varepsilon_0\varepsilon_r A} - \frac{1}{2}\frac{Q}{\varepsilon_0\varepsilon_r A} = -\frac{Q}{\varepsilon_0\varepsilon_r A}. \tag{3.6}$$

The DEAs will be operated by controlling the voltage, not the charge, so it useful to convert this equation so that it is a function of voltage, not charge:

$$V = \frac{Q}{C} = Q\frac{z}{\varepsilon_0\varepsilon_r A}. \tag{3.7}$$

The electric field E can be described by

$$E = \frac{V}{z} = \frac{Q}{\varepsilon_0\varepsilon_r A}. \tag{3.8}$$

So, Equation 3.6 can be simplified to

$$F = -\varepsilon_0\varepsilon_r A E^2 \tag{3.9}$$

and the pressure is equal to

$$P = -\varepsilon_0 \varepsilon_r E^2. \tag{3.10}$$

It is useful to look at the instability, or pull-in, point of the actuators. This is the point at which the mechanical elastic restoring force in the dielectric cannot increase at the same rate as the compressive electrostatic stress applied by the electrodes, leading to a collapse of the dielectric layer. Taking Equation 3.10, we can make the z term a function of the strain by setting $z = z_0 (1 + S)$ where S is the z-axis strain and z_0 is the initial gap between the electrodes, using the axis directions from Figure 3.12. We also know that the pressure P is equal to the Young's modulus of the material E_Y times the strain S. This can be substituted in to Equation 3.10 and after some simply algebra, we see that the resulting equation can be written as:

$$S^3 + 2S^2 + S = -\frac{\varepsilon_0 \varepsilon_r V^2}{E_Y z_0^2} \tag{3.11}$$

The instability points are the roots of the partial of Equation 3.11 with respect to the strain, or the roots of

$$0 = \frac{1}{3S^3 + 4S^2 + 1} \tag{3.12}$$

which are -1 and $-\frac{1}{3}$. As the compressive strain cannot be 100%, the instability, or pull-in, point is $-\frac{1}{3}$ strain in the z-direction.

The analysis above examined pull-in in terms of the strain of the dielectric, but

it is also necessary to understand the relationship between the applied voltage and the pull-in to determine the operational limits of the devices. To begin this, Equation 3.9 can be re-organized to show that

$$F_e = -\frac{\varepsilon_0 \varepsilon_r A V^2}{(z_0 - z)^2} \tag{3.13}$$

where z is the magnitude of the compression. We can also say that the mechanical restoring force of the dielectric layer is

$$F_m = kz \tag{3.14}$$

where k is the spring constant of the dielectric layer. Equations 3.13 and 3.14 can be combined to show the net force in the system is

$$F_{net} = -\frac{\varepsilon_0 \varepsilon_r A V^2}{(z_0 - z)^2} + kz \tag{3.15}$$

By taking the differential of the net force with respect to the displacement and substituting the solution from the pull-in strain analysis ($z = \frac{1}{3} z_0$), the resulting pull-in voltage is

$$V_{PI} = \sqrt{\frac{4}{27} \frac{k z_0^3}{\varepsilon_0 \varepsilon r A}} \tag{3.16}$$

where k is the spring constant of the dielectric material being compressed. The

dielectric can be considered a beam being compressed whose spring constant is $k = \frac{E_Y A}{L}$ where E_Y is the Young's modulus of the material. In this derivation, the length L is equivalent to the thickness of the dielectric, z. Substituting this into Equation 3.16, the pull in voltage as a function of the compliance and thickness of the dielectric layer is

$$V_{PI} = \sqrt{\frac{4}{27} \frac{E_Y z_0^2}{\varepsilon_0 \varepsilon_r}}. \tag{3.17}$$

One of the important takeaways from Equation 3.17 is that the pull in voltage depends only on the material properties of the dielectric (Young's modulus and relative permittivity) and the thickness of the dielectric.

It is also worth looking at the strain in the transverse directions. All of the elastomers used in this work are assumed to be incompressible, so volume must be conserved. This means that Equation 3.18 must be stratified. This equation assumes that there are no boundary conditions that limit the compression of the dielectric in z or expansion of the electrode and dielectric layers in x and y, which implies that the strain in x and y are the same:

$$(1 + S_z)(1 + S_x)(1 + S_y) = 1. \tag{3.18}$$

Since there is compression only in the z-direction, $S_x = S_y$, so Equation 3.18 can be simplified to

$$(1 + S_z)(1 + S_x)^2 = 1 \tag{3.19}$$

By using the Taylor series expansion of this equation, we can see that

$$S_z = -2S_x = -2S_y. \tag{3.20}$$

It is important to remember that Equations 3.11 and 3.17 neglect the influence of the electrode layers, which will work to decrease the ultimate strain that can be achieved at a given voltage. An analytical solution for the performance of DEAs with the affect of the electrode layers is possible, but is also very dependent on the specifics of the design of the DEA of interest. Additionally, it is important to include the influence of the traces which supply the electrodes of the DEA with their potential, which further degrades the performance of the DEA and further complicates the analytical solution to the equations describing the performance of DEAs. There are many other works which have focused on modeling DEAs and provide more complete derivations, but additional modeling was not included in this dissertation as the focus of the work was on the fabrication [84, 149, 142].

3.3.2 Design

DEAs are traditionally fabricated by vertically stacking alternating layers of conductive and dielectric elastomers. This method is difficult to replicate at the

microscale due to the complications involved with stacking and patterning thin layers of elastomers. Thin layers are commonly fabricated by spinning the elastomers prior to curing them. As the spin speed is increased to realize thinner layers, however, the thickness uniformity of the layers decreases rapidly. Once filler particles are added, additional complications arise due to the increase of the viscosity that occurs when fillers are added to the polymer matrix.

This work uses the fabrication process described in Section 3.1.1, which allows for molding of the elastomer layers, thereby eliminating the issues related to spinning of the polymer films. Unlike macroscale DEAs that have vertically stacked layers, the DEAs shown in this work have horizontally stacked layers. A similar approach using deep reactive ion etched (DRIE) trenches to mold dielectric polymer and silicon DEAs was proposed, but has not been successfully demonstrated [86].

By patterning alternating layers of conductive and dielectric elastomers, in-plane bending actuators can be realized, such as that shown in Figures 3.11 and 3.13. Applying an electrical potential between two of the neighboring electrodes generates a stress in the dielectric layer between the two electrodes. The elastomers used are incompressible, so this stress leads to transverse compression and axial extension of the dielectric layer that separates the two electrodes. The beam is essentially a bimorph and axial extension in one layer leads to bending of the beam. Figure 3.13a shows bending of such a DEA when a potential is applied between the bottom and middle electrodes. The beam returns to its equilibrium position once the potential is

removed, shown in Figure 3.13b. Actuation in the opposite direction is achieved by applying a potential between the top and middle electrodes, shown in Figure 3.13c.

One of the benefits of the fabrication process described in Section 3.1.1 is that the thickness of the dielectric and conductive electrode layers is determined by the width of the etched trenches. The consistency in the thickness of the layers eliminates one of the common issues in DEAs. Electrical failure of the DEAs commonly occurs at the defects in the dielectric layer where the thickness or particles allow for premature breakdown of the DEA.

The devices fabricated in this work had layer thicknesses of 20 or 30 μm. Using Equation 3.17 and assuming a linear elastic modulus of 0.267 MPa for the MRTV-9 dielectric layer, as was calculated in Section 2.3.2, the pull-in voltage at 30 μm is 1.3 kV, which sets a theoretical maximum voltage that can be applied. Another concern is the breakdown of the materials. Section 2.2 characterized the dielectric breakdown of PDMS thin films up to only 14 μm, but assuming a conservative breakdown field of 40 V/μm, which is well below any of the breakdown points measured in Section 2.2, the maximum voltage that can be applied across the 30 μm wide dielectric is 1.2 kV. It is also important to consider the breakdown of air, which could occur at the top and bottom surface of the DEA, which, according to Paschen's Law, is 548 V in air at a 30 μm gap.

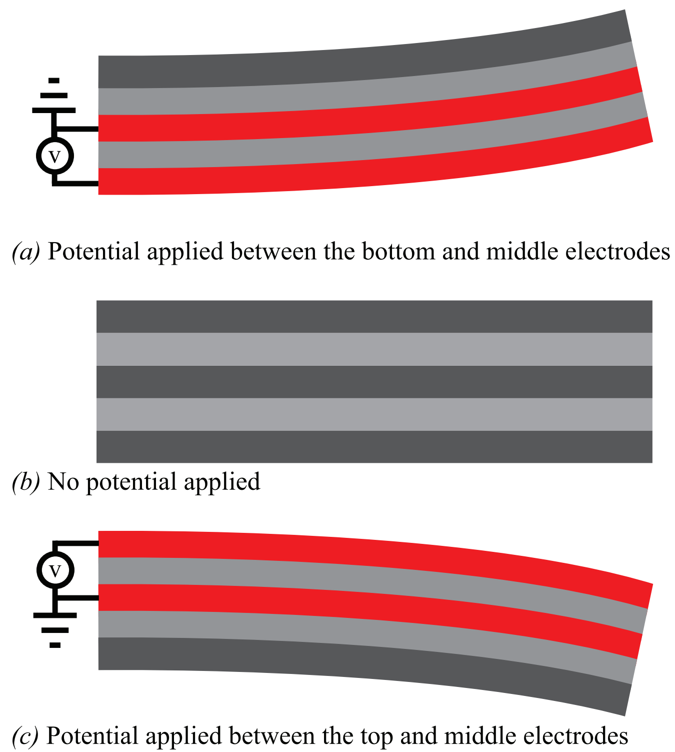

(a) Potential applied between the bottom and middle electrodes

(b) No potential applied

(c) Potential applied between the top and middle electrodes

Figure 3.13: Schematic showing how applied voltages lead to bidirectional actuation. The red layers represent the layers with applied electric potential. The left side of the beams is fixed and the right side is free.

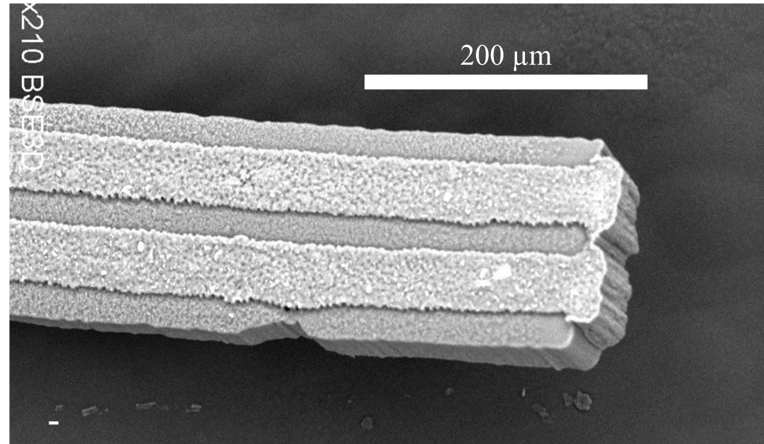

Figure 3.14: The tip of a fabricated DEA with 30 µm traces.

3.3.3 Actuation Results

A DEA with 30 µm layer thicknesses was fabricated with the process described above and is shown in Figure 3.11 with a close-up at the tip of a DEA is shown in Figure 3.14. An actuated device with 20 µm layer thicknesses is shown in Figures 3.15 and 3.16. During operation, the middle electrode was grounded and one of the outer two electrodes was put at a potential, depending on the desired direction of operation.

Unidirectional operation of a fabricated DEA is demonstrated in Figure 3.15. This shows one actuator at four different voltages. Images were taken at 0, 700, 900, and 1100 volts. Then the images were cropped and overlaid. Figure 3.17 shows the displacement of the end of the actuator as a function of voltage. The actuator is 1000 µm long, 100 µm wide (five 20 µm traces), and 40 µm thick. Operating voltages were varied between 0 and 1100 volts, which resulted in tip displacements up to

Figure 3.15: Overlaid images of the actuator at a) 0 V, b) 700 V, c) 900 V, and d) 1100 V. The red arrow shows the direction of displacement with increasing voltage.

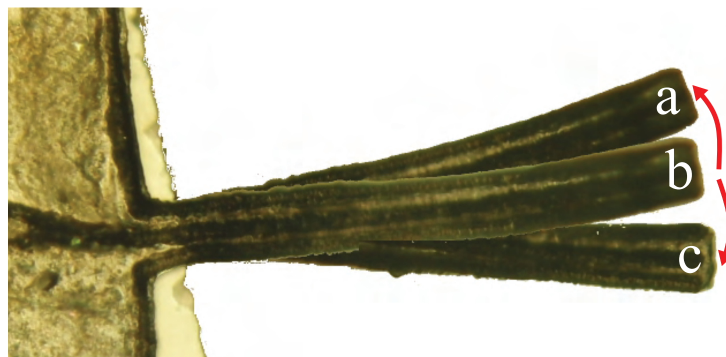

Figure 3.16: Overlaid images of a DEA demonstrating bidirectional actuation of the DEA a) up, b) at equilibrium, and c) down.

350 μm.

The experimental data was verified against a 2-dimensional model created in ANSYS. The model used the PLANE223 element type with the electroelastic coupled-field analysis mode active. This element allows for three degrees of freedom: motion in the x-direction, motion the in y-direction, and the applied voltage. The solver finds a solution considering both the structural and electrostatic components of the model. The full code used can be found in Appendix D. One of the important considerations when establishing the ANSYS model was setting the material properties. A dielectric constant of 2.94 was used, which is stated in the MRTV-9 datasheet [150]. There were no tensile tests performed on the materials used in the fabricated DEAs, so the material properties were not known. This meant that the modulus values used in the model had to be extrapolated from the data presented in Chapter 2.

The results of the material characterization from Chapter 2 was used to estimate the modulus of the DEA materials. The microscale *in situ* Sylgard 184 samples were soaked in 18:1 BHF, just like the DEAs. The *in situ* samples that were cured at 90 °C experienced a decrease in their modulus of 22% (from 2.14 MPa for the macroscale unsoaked samples to 1.68 MPa for the microscale samples soaked in BHF for 8 hours). The discussion of these results in Chapter 2 determined that this decrease was likely larger, so the ANSYS material model assumed a modulus with a decrease of 25% resulting from the BHF soak.

The dielectric layer of the DEAs was MRTV-9, which was shown in Section 2.3

to have a macroscale modulus of 0.27 MPa. The electrode layer was made from a mixture of MRTV-9, hexane, and carbon black at 17.5 wt.%. This exact material was not tested in a dynamic mechanical anaylzer, so values again had to be extrapolated. A sample with 7 wt.% carbon black was charaterized in Section 2.3 and had a modulus of 0.62 MPa. The modulus of 0.62 MPa represented a 2.3x increase over the unfilled material, or 0.33x increase per 1 wt.% of carbon black added. In order to calculate the change in the modulus of the dielectric and electrode layers, the following assumptions were used:

- Carbon black leads to a linear increase in the modulus of the polymer at 0.33x per 1 wt.% of carbon black added (i.e., a sample an unloaded modulus of 1 MPa with 1 wt.% carbon black has a modulus of 1.33 MPa and a sample with 10 wt.% carbon black has a modulus of 3.3 MPa).

- Exposure to 18:1 BHF leads to a 25% decrease in the modulus of the polymer.

These assumptions are very simplistic, but provide a rough estimate of the final polymer modulus. The Guth model shows that the linear increase with carbon added assumption is not a correct, but Chapter 2.3 also showed that the Guth model does not hold for filler particles with an aspect ratio of 1. Using these assumptions, the moduli for the two layers in was calculated, as shown in Table 3.1.

Figure 3.17 shows both the experimental results and the results of the ANSYS simulation. The ANSYS model underestimates the experimental data using the material properties described above. Even though the data for the two do diverge at

Table 3.1: Calculation of the material properties used in the FEA analysis. The calculations are based on data from Section 2.3 which showed MRTV-9 has a modulus of 0.27 MPa.

Layer	MRTV-9 Modulus (MPa)	Multiplier for Carbon Black (0.33x per wt.% CB)	Multiplier for BHF Soak	Final Modulus (MPa)
Electrode	0.27	17.5 wt.% *0.33x = 5.78x	0.75x	0.27*5.78x*0.75x = 1.16
Dielectric	0.27	-	0.75x	0.27*0.75x = 0.20

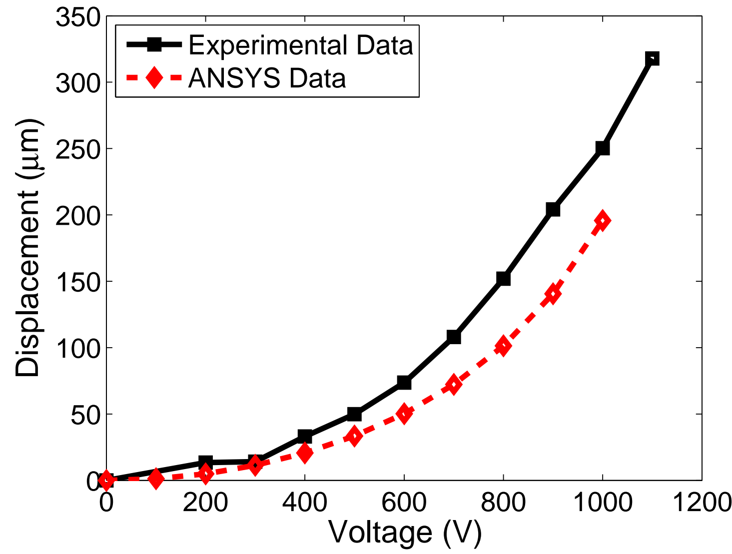

Figure 3.17: The voltage-displacement curve that corresponds with Figure 3.15.

large voltages, the similarity of two does demonstrate that the model used can at least be used to generalize the behavior of the DEAs and that the assumptions of the material properties were reasonable. The model would not converge above 1000 V because of the large displacements, so the 1100 V solution was not performed.

The operating voltages of the DEA are above the voltage at which the air was expected to break down, 440 V. The reason that there was no breakdown is not entirely understood, but is possibly due a variation in the conductivity through the depth of the actuator. Though this is not confirmed, it is expected that the carbon

black concentration at the top (top relative to how the actuator was fabricated) of the actuator was higher that the concentration at the bottom. This is because the trenches likely acted as filters for the carbon black, resulting in electrodes with dramatically lower conductivities than that of the bulk material. It is also possible that differences in the depths of the silicon etches for the conductive and non-conductive polymers led to differences in the profile at the bottom of the trench, as is evident in Figure 3.1, which would have increased the effective path over which the air would have had to breakdown. This, however, would lead to only a moderate increase in the breakdown voltage.

As was shown in Equation 3.10, the pressure in the dielectric layer has a squared dependence on the voltage. As was mentioned earlier, this actuator is a bimorph, or cantilever with layers of multiple materials [151]. There is effectively a stress generated in one of the dielectric layers which then acts on the other layers of the cantilever to generate displacements. It has been shown that the radius of curvature of a bimorph DEA is proportional to the square of the voltage [86, 129, 130, 142]. As is expected, there was a quadratic relationship between the applied voltage and the displacement. The quadratic fit to the set of points in Figure 3.17 is

$$\delta = 358.82V^2 - 127.74V + 23.44 \tag{3.21}$$

where V is the applied voltage in kV and δ is the resulting displacement in microns. The r-squared value for this fit is 0.99. The offsets of the curve are likely due to

inaccuracies in the measurement of the displacements and residual stresses in the materials. Additionally, there was a long tungsten wire (diameter of 25.4 μm which was pushing down on the DEA, holding it in place. The wire made was quite long, approximately 2 cm, so as to decrease the lateral spring constant of the actuator and minimize its effect on displacement. The wire was necessary so that the entire length of the DEA was in the same optical plane so that images of the displacement of the DEA could be acquired with a compound microscope. This may have contributed to the non-uniform curve observed in Figure 3.15.

Figure 3.16 demonstrates one actuator with bidirectional actuation achieved by switching the high potential from the top electrode to the bottom electrode. Full analysis of the transient response was limited by the available electronics, but devices were operated at frequencies in excess of 30 Hz with losses less that 10% of the static displacement.

An ideal DEA would draw current only when switching the voltage, but these devices typically drew current on the order of 10 nA in static conditions. This results in a total maximum power draw on the order of 11 μW. The output force of the actuators was not examined due to limitations of available equipment.

Figure 3.16 shows the displacement of a single actuator, but the typical displacement that was seen in all of the actuators varied widely, from just tens of microns to the results shown here of hundreds of microns. The variation in the displacements is likely due to the residual stresses in the polymer layers from exposure to heat and

the SF_6 plasma during the final isotropic silicon etch.

3.4 Conclusions

This chapter has demonstrated a process for fabricating conductive and non-conductive elastomeric polymer features together in-plane. The fabricated thermal actuators demonstrated displacements as high as 100 μm and forces as high as 55 μN. The electrostatic actuators are the first to have demonstrated actuation at sub-1000 V levels. The device achieved 350 μm of displacement with an input voltage of 1.1 kV at 10 nA for a total power consumption of only 11 μW. Additionally, both the thermal and electrostatic devices are robust and can survive large strains in tension and bending.

Chapter 4

Incorporating Silicone for Jumping Locomotion in Microrobots

The previous chapter focused on the development of actuators using microscale patterned polymer features. This chapter focuses on some of the capabilities of the manufacturing process described in Chapter 2 and take advantage of the elastic property of the material for creating mechanical energy storage systems. This chapter is based on the publication "Incorporating compliant elastomers for jumping locomotion in microrobots" from volume 22, issue 1 of *Smart Materials and Structures* by A. P. Gerratt and S. Bergbreiter, published in 2013. All of this work was performed by Aaron Gerratt other than the wirebonding on the actuated device which was performed by Ivan Penskiy.

4.1 Introduction

Nature does a fantastic job of generating impressive locomotion in small packages. Cockroaches can run at speeds up to 50 body lengths per second [152] and ants less than 5 mm long have been demonstrated running at speeds approaching 40 body lengths per second [153]. Jumping, which requires high power, is performed by insects with the help of biological mechanisms that store energy slowly and release it quickly [154]. Froghopper insects can jump to heights over 100x their own length

[155]. Such impressive movement in insects is in part due to complex mechanisms designed in small packages.

While nature can easily create these mechanisms by combining various biological materials from resilin to chitin to muscle, this is much more difficult to achieve in microrobotics. Microrobots, defined as sub-centimeter sized robots with microscale features, are typically built using microelectromechanical systems (MEMS) and microfabrication [16, 19, 44, 156, 157, 158, 159]. Since MEMS were derived from the same techniques used to build integrated circuits, they are often limited to the same materials as integrated circuits - typically silicon, silicon dioxide, silicon nitride, polysilicon, and metals [3]. These materials are brittle, limited to strains of several percent, and have moduli of 10s to 100s of GPa. The biological material that enables jumping in many insects is resilin. This material can undergo large strains, has a modulus of approximately 2 MPa, and is highly resilient (approximately 97% of energy is returned when deformed) [160]. It is promising to consider the benefits of adding compliant materials like resilin to microrobot design.

At larger scales, bio-inspired robots have taken advantage of a wide array of materials to provide the same passive mechanical properties used by insects at smaller scales. For example, iSprawl was manufactured using the shape deposition manufacturing process in which materials with various properties were combined to create complex mechanisms such as a passive hip joint for rapid locomotion [161]. RHeX maintained its mobility across a variety of terrains by taking advantage of the passive

compliance of its legs [162]. A joint made of carbon fiber and polyimide resulted in an additional passive degree of freedom that enabled in the first liftoff of a centimeter-scale flapping robot [15].

Microrobots made from traditional MEMS materials, however, lack the robustness of their biological cousins. The microrobot in [17] often lost legs due to the brittleness of 2 μm square polysilicon pin hinges. However, the only legged microrobot that has demonstrated forward motion also displayed impressive robustness, in part due to the use of polymer legs made from a combination of polyimide and silicon [16].

A key challenge in microrobotics is the addition of new materials to the currently existing microfabrication toolbox for manufacturing complex mechanisms and substantially improving locomotion. Poly(dimethylsiloxane) (PDMS) is a compliant material that can undergo elastic strains in excess of 100% and has a Young's modulus of 1.8 MPa [51], which is very similar to that of resilin. PDMS is most commonly used to quickly and easily fabricate small and clear channels for fluid flow in microfluidics and bioMEMS [42]. However, it has rarely been used for its mechanical properties, primarily because of the lack of adequate fabrication processes. Parylene has been used to replace silicon springs given its modulus of 1 GPa [26], but this is still a relatively stiff, non-elastic material. Polyimide has been used for its thermal properties in the microrobot legs mentioned above [16].

The contributions of this section include the application of a fabrication process

that integrates elastic materials into microfabrication to achieve small feature sizes and high aspect ratios for microrobot mechanisms. Compliant elastomers can increase robustness and can be used in microrobot mechanisms including energy storage/quick release structures for jumping. Other than wirebonding and breaking tethers used to hold structures in place during fabrication, no post-process assembly is required. In addition, this microfabrication process allows for integration with silicon actuators that have already been developed in the MEMS world.

An introduction to scaling for jumping and the mechanism described in Section 4.3 was included in a previous conference proceeding [57], but both have been significantly expanded in this dissertation. An earlier article by the authors described the details, characterization, and un-actuated operation of a device manufactured with the fabrication process used in Section 4.4 [44], but did not consider integrating actuation, which is directly addressed and demonstrated in this dissertation.

This section begins with an introduction to jumping robots in Section 4.2. A mechanism used to demonstrate jumping at the microscale is described in Section 4.3 and an actuated mechanism is described in Section 4.4.

4.2 Jumping Robots

The focus of this chapter is the integration of compliant materials in MEMS devices to enable jumping in microrobots. There are several key points laid out in this section that are important to keep in mind for the design of a jumping microrobot.

First, the actuators and mechanical components must be able to rapidly release energy for jumping, which can be achieved with a mechanical spring. Second, as the scale of the systems is decreased, the drag increases, so parameters such as velocity, mass, and area of the robot must be considered. Third, the actuators must be small and simple to control so that they do not adversely alter the maximum height the robot can jump and the processing required for the actuators must be compatible with the elastomeric materials used for the springs. These points are discussed in the following sections in the context of the final goal of integrating MEMS actuators and compliant materials for jumping locomotion.

4.2.1 Scaling

As the size scale of a robot is decreased from macroscale to mesoscale to microscale, challenges related to mobility increase as the size of a robot itself decreases relative to the objects in the environment around it. As a result, jumping becomes an attractive mobility method for microrobots [163]. An important performance metric for jumping robots at all scales is the energy release time [57, 164]. An insect such as a froghopper begins the process of jumping by first storing energy in resilin. When this energy is released, the froghopper's feet push against the ground and accelerate the insect. The acceleration time, defined as the time between the initiation of the jump and liftoff, can be determined with Equation 4.1; l_{leg} is the leg length and v_i is the initial takeoff velocity.

$$t_{acc} = \frac{2l_{leg}}{v_i} \tag{4.1}$$

A robot with a 1 mm leg and a desired initial velocity of 2 m/s must have a takeoff time of just 1 ms. This short takeoff time requires a means of rapidly releasing energy in order to realize the desired initial velocities, and therefore jump heights.

In vacuum, assuming the robot jumps vertically, the maximum height, h, that a robot can reach depends only on the initial velocity of the robot and the gravitational acceleration, g, as shown in Equation 4.2.

$$h = \frac{1}{2}\frac{v_i^2}{g} \tag{4.2}$$

Due to the scaling effects of drag and inertial forces, there are some additional considerations that must be made at the microscale that are not necessary with larger, macroscale robots. The Reynolds number, shown in Equation 4.3, is the ratio of inertial forces to viscous forces; μ is the dynamic viscosity and ρ is the density of the medium in which the object of interest is moving, v is the velocity of the object, and L is a characteristic linear dimension of the object.

$$Re = \frac{\rho v L}{\mu} \tag{4.3}$$

A high Reynolds number means that the inertial forces dominate the viscous forces; a low Reynolds number means that viscous forces dominate the inertial forces. A

medium-sized bird has a Reynolds number on the order of 10^5 [165]. A microrobot with a takeoff velocity of 2 m/s, a characteristic length of 4 mm, and operating in air ($\rho_{air} = 1.2$ kg/m^3 and $\mu_{air} = 1.98\text{x}10^{-5}$ kg/m/s) has a Reynolds number of 484, which is low enough that drag must be considered.

The low Reynolds number of microrobots in air implies that drag forces must be considered. The instantaneous drag force, shown in Equation 4.4, depends on the drag coefficient, C_d, the frontal area of the robot, A_{robot}, the density of air, ρ_{air}, and the instantaneous velocity of the robot, v.

$$F_{drag} = \frac{1}{2} C_d A_{robot} \rho_{air} v^2 \tag{4.4}$$

Inserting the drag force into the equation of motion and solving the differential equation leads to Equation 4.5, the jump height, h_{drag}, as a function of the initial velocity, v_i [166].

$$h_{drag} = \frac{m_{robot}}{C_d A_{robot} \rho_{air}} \ln \left(1 + \frac{C_d A_{robot} \rho_{air}}{2 m_{robot} g} v_i^2 \right) \tag{4.5}$$

This equation is a valuable tool for jumping microrobot design. A robot operating in air with a mass of 8 mg, drag coefficient of 1 [167], an area of 4 x 4 mm^2, and an initial velocity of 2 m/s would reach a maximum height of 16.6 cm.

4.2.2 Actuation

The short takeoff times demonstrated by Equation 4.1 mean that high power actuators are required. This requirement exceeds that of currently available microactuators [168]. One exception is chemical-based solutions which includes focused exothermic reactions whose byproducts work to propel the robot [169, 170]. These systems, however, require a means of carrying and mixing or activating the reagents. This poses specific challenges to integration and repeatability which need to be addressed before chemical-based actuators can reliably be integrated into jumping microrobots.

Due to the output power limitations of voltage controlled actuators, macroscale jumping robots, in addition to insects, often employ mechanisms in addition to actuators in order to slowly store energy over time that can be rapidly released [164, 171]. This enables the use of low input power actuators, which are more readily accessible, to elicit a high output power of the robot. These mechanisms work to store potential energy, be it as compressed air in a pneumatic cylinder [172, 173] or in a strained mechanical spring [164, 171, 174]. As with the chemical-based methods mentioned earlier, pneumatic systems also have specific challenges to integration and repeatability which need to be addressed. Pneumatic systems require compressed air, which must be either carried along with the robot or generated with on-board pumps, and both options pose significant additional weight requirements.

A spring-based solution, however, requires only a spring and an actuator and is repeatable for multiple jumps. One of the contributions of this work is the imple-

mentation of elastomers for enhancing the capabilities of microrobots. A thorough justification for an elastomer spring over more readily available materials like silicon is discussed in previous works by the authors [44, 166]. Advantages include increased robustness, lightweight and high energy density elastomer springs, and simple integration with silicon-based actuators.

There are several types of MEMS actuators that can be integrated into a microrobot including electrostatic, thermal, piezoelectric, and electroactive polymer actuators, among others [168, 175]. Electroactive polymer actuators, such as dielectric elastomer actuators and ionic polymer actuators, are promising due to their robustness, but require more development to increase force densities and to simplify and generalize fabrication before they can be integrated into microrobots [85, 148, 140]. Piezoelectric actuators have been integrated into centimeter-scale walking and flying robots [15, 176], but it is difficult to scale these complete systems down with existing fabrication processes. Piezoelectric materials also impose limitations on the materials that can be used because of the processing parameters such as high temperatures. Electrostatic and thermal actuators, however, have already been demonstrated in microrobots [17, 159] and are easily fabricated in silicon [135, 177]. Thermal actuators are beneficial because they can generate large forces and because of the simplicity of their design, but are not suitable for autonomous, untethered operation because they are very inefficient (10^{-7} electrical efficiency [135]). Electrostatic actuators are much more efficient, but currently lack the force density and robustness required to

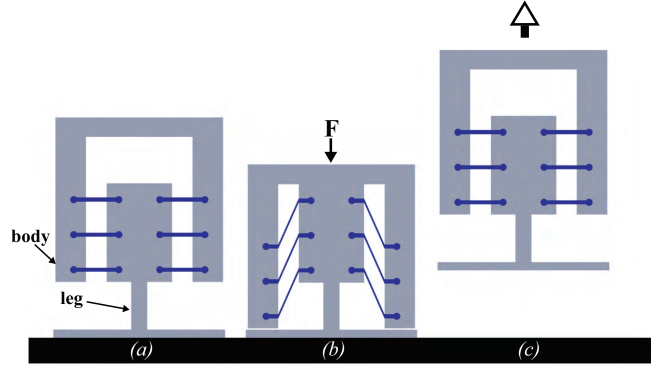

Figure 4.1: A schematic of the three phases of the jumping process: (1) equilibrium position, (2) with an external force applied, and (3) just after takeoff.

compete with thermal actuators [178]. This dissertation uses thermal actuators for force density and simplicity, but future work will apply electrostatic actuation.

It is worth noting that a complete robot is a complex, integrated system that includes power, control, sensing, and actuation. This dissertation addresses issues related to actuation including the actuators themselves and the mechanisms on which these actuators perform work. Based on the discussion above, fabrication to incorporate elastomer-based mechanisms and silicon thermal actuators has been demonstrated for the first time. However, this dissertation does not address power, control, and sensing, but it does consider these issues in the context of how they affect performance and future work.

4.3 Jumping Mechanism

In order to examine jumping locomotion at the microscale, a jumping mechanism was fabricated and first presented in [57]. The robot mechanism is essentially

two rigid masses that are connected by a series of elastomer springs, as shown in Figure 4.1. In this case, the robot "leg" is in the center of the device and the robot "body" is the u-shape around the outside. When an external force is applied, the structure is compressed and the springs are strained, storing potential energy. When the external force is removed, the potential energy is released. The force in the springs works to increase the kinetic energy of the body.

One of the keys to the fabrication of such a mechanism was the integration of the elastomer spring into the semiconductor fabrication. Previous work accomplished this in a similar system by manufacturing the springs on a silicon-on-insulator chip, but the system was fragile and could not demonstrate jumping [44]. A new fabrication process was developed using a 300 μm thick, 100 mm diameter double side polished (DSP) silicon wafer and deep reactive ion etching (DRIE). A standard DRIE process results in high aspect ratio trenches; features that are 2 μm wide and 40 μm deep are possible. By combining two DRIE steps with one elastomer molding step, planar silicon and elastomeric features were simple to create. The elastomer used in all of this work was Sylgard 184 PDMS from Dow Corning, but the process has also been adapted to work with other elastomers.

4.3.1 Fabrication Process

The fabrication process, shown in Figure 4.2, began with the plasma enhanced chemical vapor deposition (PECVD) of an 8 μm thick layer of silicon dioxide on the

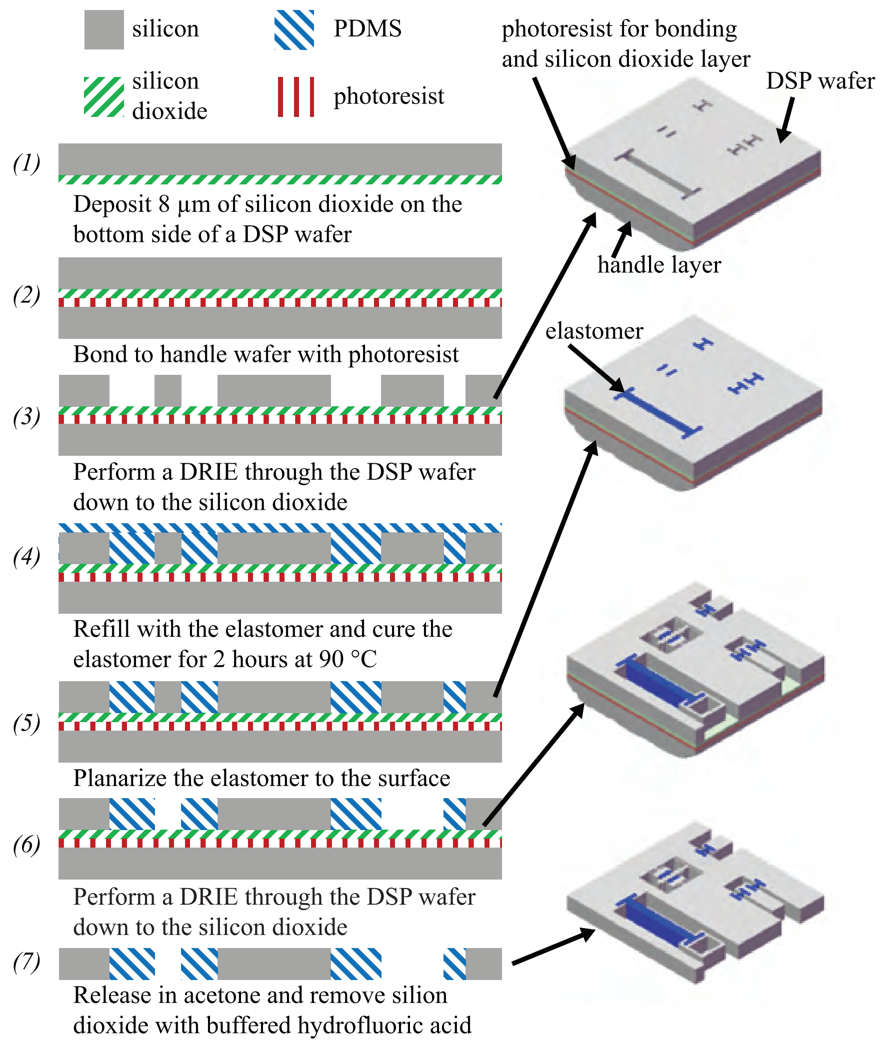

Figure 4.2: Cross-section and perspective views of the DSP-based fabrication process.

backside of a silicon wafer, shown in Step 1. A 15 μm thick layer of photoresist was deposited and patterned on the front side of the wafer. This photoresist layer served as a mask for the first DRIE process. Prior to the DRIE, the wafer was bonded to a handle wafer using a thick layer of photoresist and was baked for 2 hours at 90 °C. After this bonding step, the DRIE was performed. The DRIE was complete when the entire thickness of the DSP wafer was etched, shown in Step 3. This set of trenches formed the mold for the elastomer features.

The elastomer was prepared using the manufacturer-recommended process. A 10:1 ratio of the base to the curing agent was used. The two were mixed thoroughly and then poured over the surface of the wafer. To ensure that the elastomer completely refilled the trenches, the wafer was put into a vacuum and held at 1 Torr for 10 minutes. The elastomer was then cured at 90 °C for two hours, shown in Step 4.

Once the elastomer was cured, the excess was removed from the surface of the wafer by running a razor blade across the surface of the wafer. This left some residual pieces of elastomer, so a one minute rinse in a 3:1 mixture of n-methylpyrrolidone and tetrabutylammonium fluoride was performed [59]. This planarized the elastomer to the top of the wafer, shown in Step 5.

The new surface was planar enough that a new layer of photoresist could be deposited and patterned on the front side of the wafer. This created a second mask which was used to perform a second DRIE through the entire thickness of the wafer. The result of this etch was silicon features that were patterned around the elastomer

features, shown in Step 6.

The final step in the process was to release the devices from the handle wafer by soaking the wafers in acetone and performing a brief etch in 6:1 buffered hydrofluoric acid (BHF) to remove the silicon dioxide mask, shown in Step 7.

4.3.2 Results

Using the process described above, the mechanism in Figure 4.1 was fabricated. A scanning electron microscope (SEM) image of the final fabricated device is shown in Figure 4.3. The mechanism was 4 mm on a side and had a total mass of 8 mg. The elastomer springs were 720 μm long, 100 μm wide, and 300 μm thick, the full thickness of the wafer. The elastomer spring dimensions were designed so that the stored energy was approximately 100 μJ. Equation 4.1 indicates that this amount of energy would result in a jump height of 127 cm in vacuum, or 58 cm in air, according to Equation 4.5.

By compressing the robot with tweezers and therefore tensioning the elastomer springs, mechanism was repeatedly launched and reached a maximum height of 32 cm. A series of 18 jumps reached an average height of 19.4 cm with a standard deviation of 7.2 cm. Failed launches, defined as ones that reach heights less than 2 cm, were not included in these statistics. The jumping performance varied greatly because of the method of launching the robot. It was not uncommon for the robot to hit the tweezers during or immediately after takeoff, which dramatically affected the jump

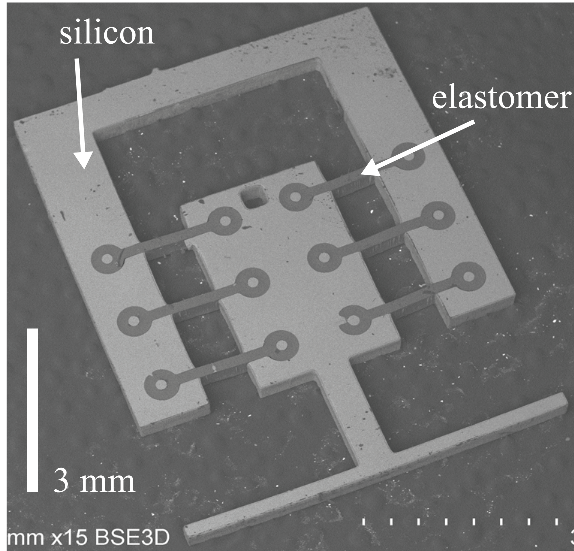

Figure 4.3: A SEM image of the jumping mechanism.

performance. The height was determined by launching the robot in front of 1 cm grid paper and video of several jumps was taken with a Casio Exilim EX-F1 camera at 300 frames per second. Screenshots from these videos are shown side-by-side in Figure 4.4. The maximum jump height of 32 cm was 80x the robot's own height, and the same robot was used repeatedly, demonstrating the robustness of the process and final mechanism. A video clip which demonstrates the jumping mechanism is included as supporting information.

The jump that reached 32 cm had an initial velocity of 3 m/s, or initial kinetic energy of 36 μJ. This number was calculated by measuring the distance traveled between two frames of the video. This corresponds to a Reynolds number of 726 (ρ_{air} = 1.2 kg/m^3, v = 3 m/s, L = 0.004 m, and μ_{air} = 1.98x10^{-5} kg/m/s). A Reynolds number this low means that drag should be considered. According to Equa-

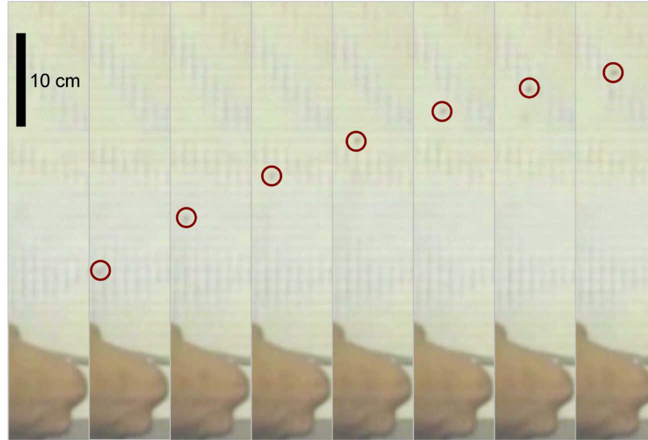

Figure 4.4: Screenshots from a video showing the takeoff of the jumping mechanism. Due to the small size of the jumping mechanism relative to the scale of the jump, the mechanism is difficult to make out, but it has been circled in each frame to show the position.

tion 4.5, a jump height of 32 cm requires 38 μJ at takeoff, which matches well with the calculated initial kinetic energy. An initial velocity of 3 m/s in vacuum, however, would result in a height of 46 cm according to Equation 4.2. Assuming 100 μJ of stored energy, the calculated transfer efficiency from stored potential energy to kinetic energy used for a jump is 40%. Losses can be due to spring viscosity, leg mass [179], rotation, and interaction with the tweezers during takeoff, among other factors. Previous work by the authors demonstrated hysteretic losses on the order of 20 to 30% [44]. Assuming hysteretic losses of 30%, the losses due to other sources such as leg mass and rotation also contributed 30% losses.

The robot demonstrated here achieved jump heights almost 80x its own size. This is similar to the froghopper insect mentioned in the introduction that can reach heights 100x their own size. This comparison, however, does not account for the

fact that the froghopper includes all of the components necessary to jump (muscles, skeleton, sensory neurons, etc. [180]). The robot includes only the mechanisms required to demonstrate a jump. In order to jump autonomously, however, actuators, control, and power are also required, each of which will add to the mass and size of the robot. The robot also did not include mechanisms that mimic the mechanics of a jump performed by a froghopper. The froghopper has several features that aid its jumping ability including sensory mechanisms that aid in the timing of the jump mechanics, small spines on the bottom of their legs that increase friction with the surface from which they are jumping, and specialized legs to enhance jumping [181]. Mechanisms such as these can be exploited in future generations of the robot once the ability of the fabrication process to be create joints is determined, which is a topic of future work.

4.4 Combining Actuation and Elastomer Mechanisms

While the mechanism described in Section 4.3 is useful for examining the merits of jumping microrobots, it is interesting to consider how actuation can be added to such a system, as any system employed outside of a laboratory setting would require on-board actuation. The fabrication process described in Section 2.1.2 was used to manufacture these devices.

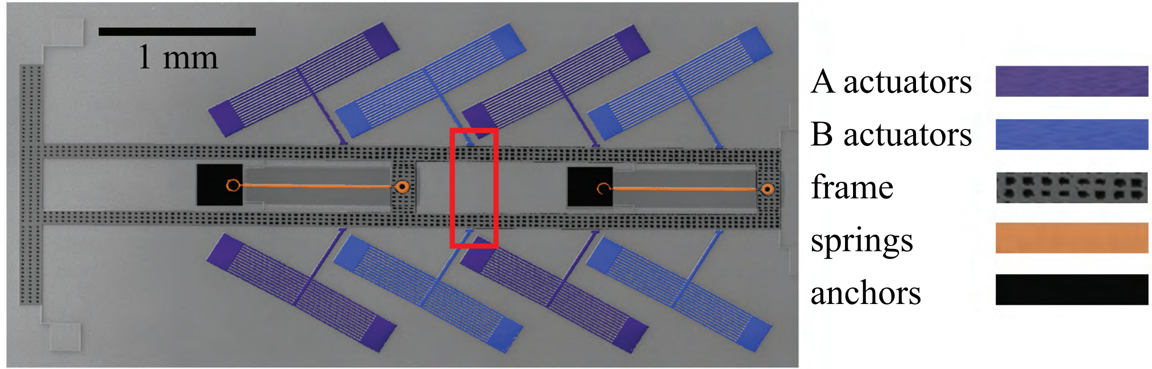

Figure 4.5: A colored SEM image of the actuated mechanism. The blue and purple areas are the two sets of actuators. The orange areas are the springs. The black areas are the anchors for the springs. The patterned gray area is the frame. A closeup of the area inside the red box is shown in Figure 4.7.

4.4.1 Actuated Mechanism

A SEM image of a fabricated actuated mechanism is shown in Figure 4.5. The color in this image was added after it was captured for illustrative purposes. The frame is shown in dark gray with black patterning. The frame was used to transfer the force from the actuators to the springs. The springs, orange in color in Figure 4.5, were anchored to the substrate at one end, shown in black, and were attached to the frame at the other end. There were two sets of actuators arranged around the frame; one set is blue and the other set is purple. Figure 4.5 shows a mechanism with two springs, but mechanisms with eight springs (two sets of four) were also fabricated, shown in Figures 4.8 and 4.9.

The actuators used in this work were thermal actuators, often referred to as chevron actuators because of their angled arms which resemble a chevron. When a

current was passed through the structure, the silicon heated up due to Joule heating, which resulted in expansion of the silicon. The temperature the actuators reach was directly related to the amount of current passed through the actuators. The chevron actuators, shown in Figure 4.6, were symmetric structures. The voltage was applied between the two large pads on either side of the thin beams. There were twelve 10 μm beams on either side which, when heated, expanded towards each other. The beams were at a slight angle, so the expansion led to bending of the beams, which pushed the central beam forward, as labeled in Figure 4.6. The thermal strain can be calculated with Equation 4.6:

$$\varepsilon_{thermal} = \alpha \Delta T \tag{4.6}$$

Silicon has a thermal coefficient of expansion of 2.9 ppm/K at room temperature [127]. Previous work demonstrated 800 K is the approximate maximum temperature the actuators should reach during normal operation [135]. The temperature change of 502 K (from room temperature of 298 K to 800 K) results in 1.5 millistrain. A strain this small can result in large displacements due to the configuration of the chevron beams. Figure 4.7 shows the actuators in the on and off positions to show how they interface with the frame.

It is worth noting the symmetry of the mechanism shown in Figure 4.5. The actuators had to be symmetric on either side of the frame since the frame was not anchored at any point. If there were actuators on only one side, the actuators would

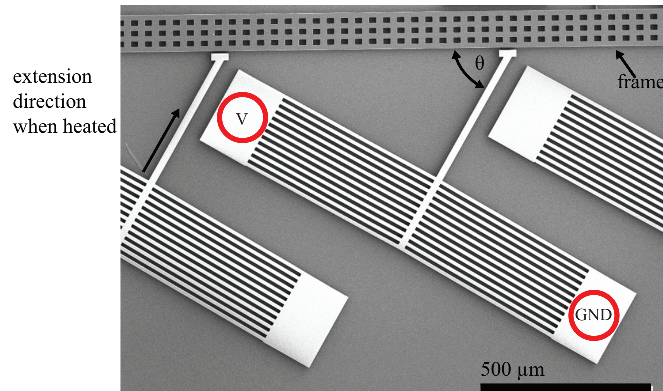

Figure 4.6: A SEM image of a thermal actuator. The voltage was applied to the inner pad next to the frame and ground was applied to the other outer pad.

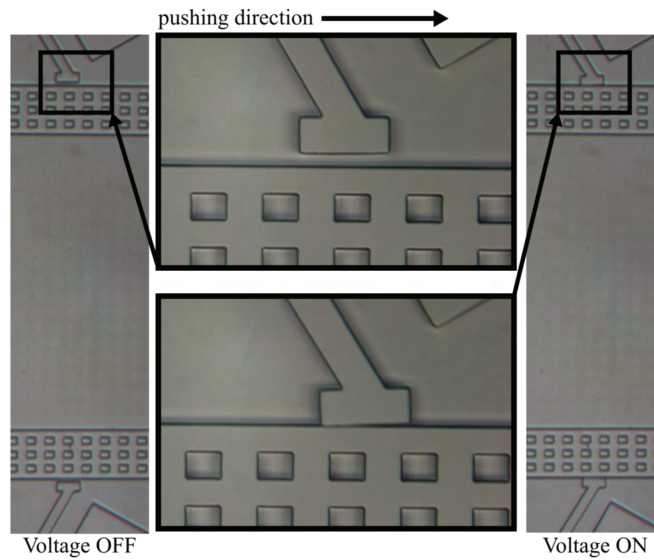

Figure 4.7: Closeup on the area down in the red box on Figure 4.5. The thermal actuators are shown in the off and on positions and closeups on the pads on the actuators which engage with the frame during operation are shown to demonstrate the motion. The actuators push the frame from left to right in small steps which are accumulated to achieve large displacements.

simply push the frame up or down. The symmetry meant that the up/down forces (normal force) of the actuators worked against each other so there was no net up/down motion of the frame, but the left/right drive forces of the actuators added serially to push the frame.

The actuation scheme was based on the design presented in the work by Maloney [135]. By operating the A and B sets of actuators in an alternating fashion, many small displacements of the frame were accumulated to result in a large displacement. The sequence began with both the A and B actuators on. Then the A actuators were turned off, allowing the B actuators to push. The A actuators were then turned back on, returning the actuators to the intermediate step with both actuators on. Finally the B actuators were turned off, allowing the A actuators to push. The process was repeated until the desired displacement has been achieved. A video clip which demonstrates the actuated mechanism is included as supporting information.

During operation the voltage was switched between V_{low} and V_{high}. One important note is that V_{low} was not 0 V. By switching between two higher voltages, a faster response was possible. V_{low} was set to be just low enough that the actuators did not engage with the frame. This left the frame free to move with respect to that set of actuators, while not requiring them to cool to room temperature. This was particularly important because of the nature of the thermal actuators. One of the downsides of using these actuators was the relatively long thermal cycling time that was required. By cycling over a smaller range of voltages, the thermal cycling time

was reduced, therefore increasing the operating speed. A complete thermal analysis of these actuators was performed in previous work [135].

There were two forces that needed to be balanced during operation. The first was the friction force between the actuator and the frame. The second was the force exerted along the length of the frame, or drive force. If the friction force was too small, the beam of the actuator that interfaced with the frame would simply slip along the frame when engaged. As the friction force was increased, so was the maximum possible drive force. The magnitude of the two forces was determined by the angle of the between the actuator arm and the frame, labeled as θ in Figure 4.6. As the angle approached 90°, more of the total force output of the actuators contributed to increasing the fictional force at the expense of the driving force. As the angle approached 0°, more of the total output force of the actuators contributed to increasing the driving force at the expense of the friction force. The angle used in the fabricated mechanisms was 60°.

The voltages were applied to the actuators with probes under a microscope. There were three probes required: one for the ground, one for the A actuator voltage, and one for the B actuator voltage. The grounded probe was simply touched to the handle layer of the wafer. This simplified the wirebonding that was required because the end of the actuator facing away from the frame, as labeled in Figure 4.6, was wirebonded to the handle layer with a short wirebond to ground the pad. Then all of the actuators in set A were wirebonded together and all of the actuators in set B

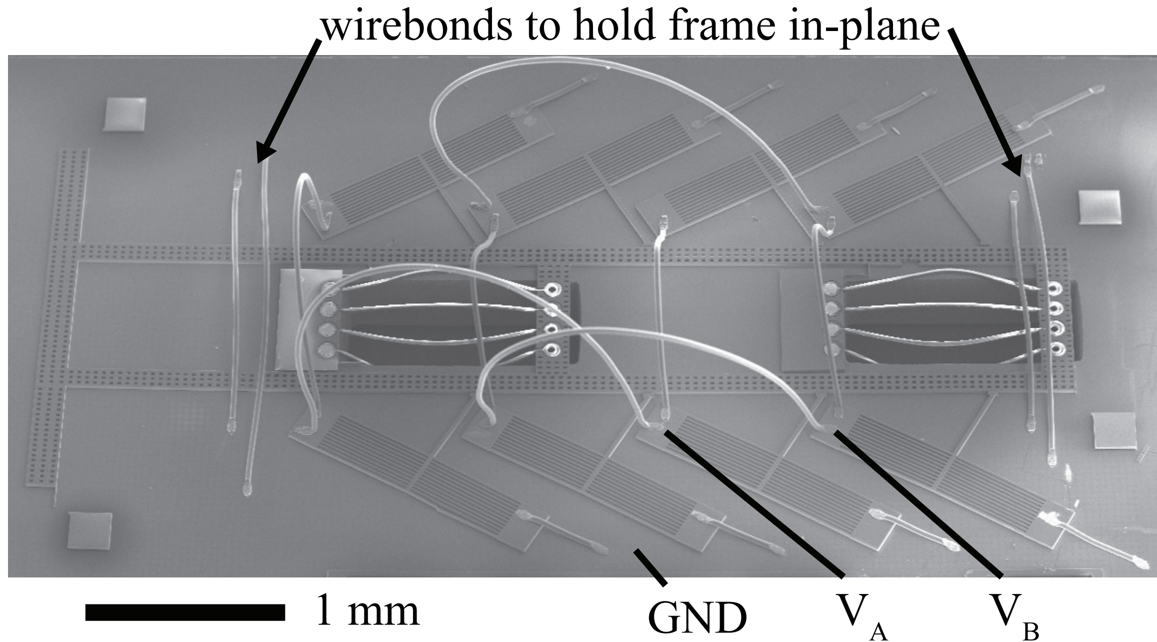

Figure 4.8: A fully wirebonded actuated mechanism. Note the extra wirebonds which cross over the frame. These wirebonds worked to hold the frame down in-plane during operation. V_A was the voltage applied to the A actuators. V_B was the voltage applied to the B actuators. The entire substrate was grounded, so the outer pad of each actuator was grounded with a wirebond.

were wirebonded together, shown in Figure 4.8.

4.4.2 Results

After fabrication, the tethers holding the frame in place were broken and the actuators were wirebonded together. Then the actuators were used to repeatedly store and release energy in the elastomer springs. Figure 4.9 shows the system in two states: unstrained on the left and strained on the right. This figure show the frame after it was advanced 580 μm, straining the 1 mm springs 58%. The solid yellow line shows the position of the top of the spring attachment point in the unstrained

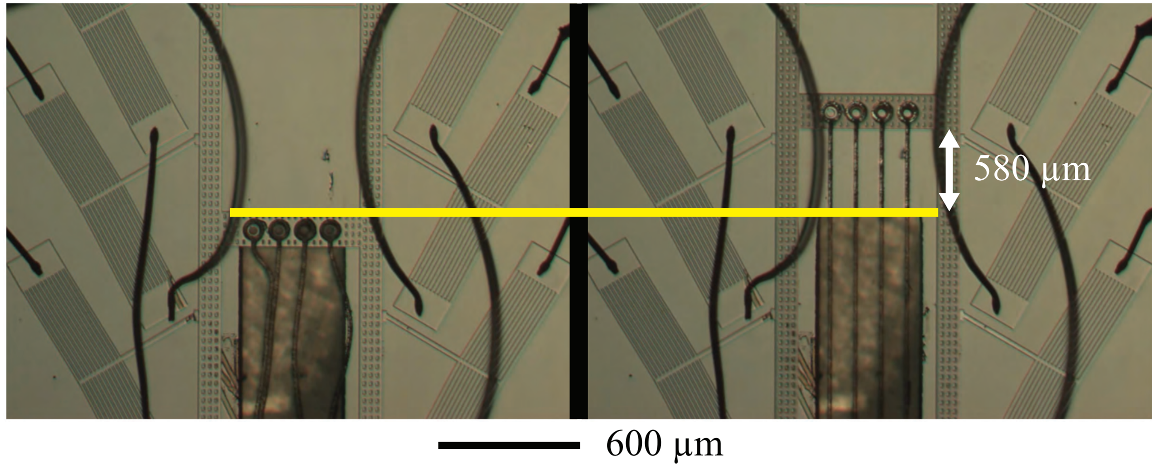

Figure 4.9: Two images of the system before (left) and after (right) the actuators were sequenced. The frame was advanced 580 μm during the voltage sequencing.

condition. It is worth noting the state of the elastomer springs in Figure 4.9. In the unstrained condition, the two leftmost springs were stuck to each other and the rightmost spring was stuck to the substrate. During operation it was not uncommon for the springs to stick to each other or the substrate. The adhesive force, however, was not great enough to keep the springs attached once strained, which is evident on the right in Figure 4.9. The backside etch in Step 6 of the fabrication process aided in alleviating this issue.

The actuated mechanism was used to propel a projectile, as shown in Figure 4.10. The voltage signals were generated using an Arduino Uno microcontroller and a motor driver. The system was cycled to strain the elastomer springs 45% and store 0.45 μJ. The projectile, an 0402 sized surface mount capacitor with a mass of 1.4 mg, was then placed directly in front of the frame. The actuators were then turned off, releasing the frame. The force from the energy stored in the springs

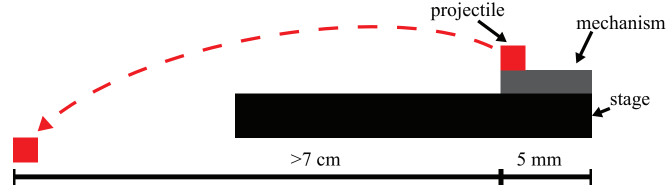

Figure 4.10: A schematic of the test setup. The projectile was placed on top of the wafer substrate, which was placed on a stage under a microscope.

worked to accelerate the frame, which in turn worked to accelerate the projectile. The projectile was 1 mm long, 0.5 mm wide, and 0.5 mm tall. In the best test, the projectile traveled more than 7 cm, so it traveled at least 70x the longest dimension of the projectile. The exact distance is not known because the projectile fell off the stage under the microscope after it traveled 7 cm. As with the tests performed on the jumping mechanism, not every test was successful. The projectile was 0.5 mm tall, but the frame of the actuated mechanism was only 0.02 mm tall, so during several tests the frame slide under the projectile. In a series of eight consecutive tests, five were successful and had projectile travel distances with an average and standard deviation of 4.82 cm and 1.9 cm, respectively. A failed test was defined as one where the projectile travelled less than 1 cm.

As was mentioned in the introduction, one of the benefits of being able to integrate a material such as an elastomer is the ability to have repeatable actuation. Several tests were performed where the springs were strained to store energy and then released to allow the springs to return to their unstrained position. This cycle was then repeated to strain and release the springs a total of 10 times. This test was performed

17 times with one device at various operating voltages and frequencies without failure for a total of 170 strain/release cycles, demonstrating the robustness of the elastomer material. These tests strained the springs to several 10s of percent strain, but strains as high as 100% were demonstrated. The fastest speed demonstrated was 0.7 mm/s to achieve 45% strain. This was an average speed over the entire strain cycle as the speed decreased as the strain, and therefore force in the springs, increased.

4.5 Discussion

One issue encountered was that the frame would pop out-of-plane during operation. This issue was exacerbated by the fact that the frame was only attached to the springs; there was nothing working to keep the frame in the same plane as the actuators. As a result, the force of the actuators on the frame was significant enough that the pads of the actuators which interfaced with the frame worked to push the frame up out-of-plane. The solution was to use a series of wirebonds across the frame to hold it in-plane. These wirebonds can be seen in Figure 4.8. The left and rightmost wirebonds across the frame were attached to the substrate at both ends, so did not pass any electrical signals, but simply served to hold the frame in place.

The actuators used in this work drew 0.4 A at 12 V per set of actuators for a total power draw around 10 W, depending on the exact voltage being applied. While this power is excessive for many applications, thermal actuators are valuable because of their robustness, large displacements, and ease of design. Before on-board

power can be integrated into the system, it is necessary that either the efficiency of the thermal actuators be improved or a more efficient actuator be implemented. The former is an issue with all thermal actuators, so it is necessary to identify an alternate transduction method. Prior work by the authors demonstrated the application of the process described in Section 2.1.2 to manufacture electrostatic actuators with integrated elastomers for thin films [45]. There are also several examples of inchworm-type electrostatic actuators which can be used to deliver a similar force density as the thermal actuators that were employed in this work [17, 177, 178, 182, 183, 184]. As of the publishing date of this work, the force per area of SOI-based electrostatic inchworm actuators is approximately one order of magnitude lower than that of the thermal actuators used in this work (0.28 mN/mm^2 for electrostatic [45] and 1.28 mN/mm^2 for thermal [135]), but the electrical efficiency of the electrostatic actuators is five orders of magnitude higher than that of the actuators used in this work (17% for electrostatic [45] and 10^{-5}% for thermal [135]). Once the issues related to the integration of electrostatic actuators have been resolved, efficient options for storing and releasing potential energy in elastomer springs can be demonstrated.

The results in this chapter came from tests that were performed under ideal test conditions. In real-world applications, however, the conditions in which robots operate are variable and sometimes unknown. As was mentioned in Section 4.2.1, outside physical forces exerted on jumping robots change with size scale. Other work has explored centimeter-scale jumping robots in uncertain, stochastic environments

[185], but did not consider microscale robots. Analysis of the influence of the environment on the performance of the robots is necessary in order to demonstrate a jumping microrobot with repeatable and reliable operation. This is particularly true for repeated jumping, as the robot must either always land in the jumping position or be able to either right itself [185, 186, 187]. These considerations, however, are outside of the scope of this dissertation and is a topic for future work.

4.5.1 Comparison of the two Systems

It is interesting to compare the results from the two systems. The jumping mechanism from Section 4.3 stored 100 μJ while the actuated mechanism from Section 4.4 stored only 0.45 μJ. The discrepancy between the two systems is largely due to the difference in the two fabrication processes. The DSP process utilized the entire 300 μm thickness of the wafer while the SOI process could utilize only the 20 μm device layer of the wafer. SOI wafers with thicker device layers can potentially be used to increase the thickness, and therefore spring constant, of the elastomer springs, but the thickness is limited by the achievable DRIE aspect ratio. The energy in the actuated system can also be improved by increasing the maximum strain before release. By increasing the width and thickness of the springs from 20 μm to 40 μm and straining the springs to 100%, 9 μJ can be stored in an 8 spring system, such as that shown in Figure 4.8. This would be enough energy for an 8 mg, 4 mm x 4 mm robot to reach a jumping height of 10.1 cm in air.

4.6 Conclusions

This section demonstrates the application of the first microfabrication process to incorporate compliant elastomer structures in-plane with traditional silicon micro-electromechanical systems. By incorporating new materials, elastomer springs were applied as compact energy storage mechanisms for small jumping robots. The fabrication process for an 8 mg jumping mechanism that was 4 mm x 4 mm x 0.3 mm was described. The device stored 100 μJ, 40% of which was transferred into kinetic energy of the mechanism resulting in jump heights as high as 32 cm. A similar fabrication process was used to fabricate an actuated system on an SOI chip. This thermally actuated device stored and released 0.45 μJ to propel a 1.4 mg projectile more than 7 cm. The jumping mechanism and the actuated mechanism were both used repeatedly to store and release energy, demonstrating the enhanced mechanical robustness of the devices manufactured with these processes.

Chapter 5

Conclusions, Contributions, and Future Work

5.1 Conclusions and Contributions

This dissertation presents a large step forward toward developing new generations of polymer-based microrobots. The process presented in Chapter 2 was used to create various components for microrobots. Robust actuators with displacements on the order of several hundreds of microns were presented. The operating voltages of microscale dielectric elastomer actuators were reduced an order of magnitude to sub-1000 V levels. Elastomer springs, or microscale rubber bands, were fabricated and integrated with silicon actuators to create microscale energy storage and release systems. The variety of devices that were created using a basic fabrication framework demonstrates the generality of the fabrication process. This is important because it demonstrates that the process can be adapted in order to meet the particular demands of various applications; the process is not intended for a specific device, but is meant to enable batch fabrication with new materials for a wide variety of devices. Ultimately the goal and purpose of this dissertation was to improve fabrication capabilities so that future microrobot design is not limited to traditional materials like oxides and silicon, but can use polymers such as those used throughout this dissertation.

The following list describes the specific contributions of this dissertation:

1. Development and Characterization of Novel Silicon and Elastomer Microfabrication Process

    - This dissertation presents the details of a fabrication process that creates elastomer features together with silicon features. The process is the first to integrate mechanical elastomer features with silicon features at this size scale. One of the major improvements of this process over others methods is the batch processing and the generality of the process. While PDMS thin films down to 10s of μm can be achieved by spinning, the process demonstrated in this dissertation allows for patterning film dimensions at any size scale from single microns to 100s of microns at the same time. The details of the process provided include the process tool parameters, which will simplify the task of repeating the process or replicating the work. The process was designed for the purpose of creating components for microrobots, but is generally applicable across many scientific fields.
    - Mechanical characterization of elastomer features fabricated in the process was completed. Results of tests performed *in situ* on microscale samples using a custom MEMS device fabricated in an SOI wafer were compared to results of similar tests performed on macroscale samples with a dynamic mechanical analyzer. This allowed for a detailed analysis of the effect of all of the processing steps on the mechanical behavior of the PDMS

samples. This analysis represents the only large-strain characterization of PDMS samples at the single microns scale, which makes the information presented in the results and analysis particularly useful for design of mechanical structures. The fact that this analysis considers the effect of the exposure to chemicals and plasmas during the fabrication makes this work particularly unique. Many other works at this scale use results of macroscale tests without accounting for the processing. This dissertation provides information which will allows for such accounting to be made.

- The polymer used throughout this dissertation, PDMS, is commonly used as a passivation layer on electronics to isolate traces and components from the outside world. This dissertation provides results of tests on the breakdown of PDMS films from 2 μm to 14 μm, scales which have not previously been explored with silicon electrodes. This data is also necessary for the design of dielectric elastomer actuators at these length scales. The maximum operating voltage of DEAs is dependent on the breakdown point of the dielectric layer, but until this dissertation the breakdown PDMS thin film had not been characterized at these film thicknesses.
- The polymer used throughout most of this dissertation is a dielectric material, but work included demonstrates how carbon black filler particles can be added to the polymer to create conductive polymers. This included characterization of the effect of the filler particles on the modulus of the

materials as well as the change in conductivity of the material with amount of filler particles added to the polymer matrix.

2. Thermal Microactuators

   - An all-polymer fabrication process based on the elastomer and silicon process was detailed. This process allows for fabrication of dielectric and conductive polymer features together in-plane at length scales from tens of microns to hundreds of microns.
   - This all-polymer fabrication process was implemented to fabricate thermal actuators that take advantage of the relatively large coefficient of thermal expansion of the polymers. When powered via Joule heating the actuators were designed to expand and displace. Three different styles of actuators were demonstrated and showed displacements as high as 100 μm and forces as high as 55 μN.

3. Dielectric Elastomer Microactuators

   - Using the same all-polymer fabrication process developed for the microscale thermal actuators, electrostatic dielectric elastomer microactuators were fabricated. A 1 mm long electrostatic dielectric elastomer actuator demonstrated a tip displacement as high as 350 μm at 1.1 kV with a electrical power consumption of 11 μW. The thermal and electrostatic actuators were both fabricated with elastomeric polymers, so they are very robust

and can undergo large strains in both tension and bending and still operate once released.

- Operation at sub-1000 V levels is significant as the operating voltage of DEAs is typically on the order of several thousands of volts, so these actuators demonstrate an order of magnitude improvement.

4. Actuated Micromechanism

- Using the silicon and elastomer fabrication process, mechanisms for storage and release of potential mechanical energy were designed and fabricated. The purpose of these devices was to evaluate the feasibility of jumping microrobots using on elastomer-based energy storage systems.
- The fabrication process for an 8 mg jumping mechanism that was 4 mm x 4 mm x 0.3 mm was described. The device stored 100 μJ, 40% of which was transferred into kinetic energy of the mechanism resulting in jump heights as high as 32 cm.
- A similar fabrication process was used to fabricate an actuated system on an SOI chip. This thermally actuated device stored and released 0.45 μJ to propel a 1.4 mg projectile more than 7 cm.
- The jumping mechanism and the actuated mechanism were both used repeatedly to store and release energy, demonstrating the enhanced mechanical robustness of the devices manufactured with these processes.

5.2 Future Work

While this dissertation answers many questions about the integration of silicon and polymers together in MEMS devices for microrobotic applications, there are still many areas that can be explored further. Much of the work presented in this thesis is related to development of the details of the fabrication process and the characterization of the materials used in the process. While there was much work done on the implementation of the materials, there are still several areas which can be explored further.

One of the topic of particular promise is the use of the fabrication process used in Chapter 3 for the thermal and electrostatic all-polymer actuators. This work, especially the electrostatic actuators, show great promise, especially as the scale of the actuators is decreased. The actuators described in this work had 20 μm smallest dimensions, but if improvements to the process can be made these dimensions can be decreased even further. The biggest issue that needs to be addressed is the conductive polymer. The polymer used in this dissertation was a carbon black and PDMS composite, which has a very low conductivity, on the order of 0.1 S/m. This conductivity, however, was measured on bulk macroscale samples and does not necessarily translate directly to the microscale features. One of the largest issues was creating reproducibly conductive samples. This is because of the relatively high viscosity of the composite mixture. The samples were diluted with a solvent in order to decrease

the viscosity, but the solvent evaporates quickly as the vacuum used to evacuate the trenches is pulled. A material using different filler particles such as carbon nanotubes or graphene in a low viscosity polymer matrix that does not require dilution with a solvent would offer a much more reliable solution this issue. Ideally the material would be able to refill high aspect ratio trenches at gaps down to single microns.

The actuated mechanism described in Chapter 4 is impressive in its ability to integrate silicon and polymer components together on a single chip. Some of the details of the design, however, can be improved upon, especially related to the actuators. The thermal actuators used in this design required a significant amount of power, 2.5 W per actuator or 10 W for the entire device. This is not a suitable solution for a device which has to rely on a limited power supply such as a battery, solar cells, or energy harvester. There are, however, alternative solutions which can be used in order to reduce the power consumption, such as electrostatic actuators. One of the issues with electrostatic actuators is the low force density compared to that of the thermal actuators, but recent work has shown that electrostatic actuators that operate in a manner similar to that of the thermal actuators used in this dissertation can achieve the same forces with electrical power draws that are orders of magnitude lower and efficiencies that are orders of magnitude higher [188]. There are issues related to stability and generation of the control voltages for these electrostatic actuators, but they still represent an attractive alternative to the thermal actuators used in this dissertation.

Outside of building on the work described in this dissertation, the fabrication process used to create actuators in Chapter 3 of this dissertation can also be used to create sensors. The benefit of such a process is that the materials used are all polymers, which adds a level of robustness to the devices. Similar materials have been used to fabricate compliant tactile skins at much larger sizes, but this process presents the opportunity to scale down the size of the sensor nodes to 100s or even 10s of microns in size, depending on the application requirements.

Appendix A

Details of the Fabrication Process

This Appendix provides details of the fabrication process which was used throughout this dissertation.

List of abbreviations used in Table A.1:

PECVD - plasma enhanced chemical vapor deposition

RIE - reactive ion etch

HMDS - hexamethyldisiloxane

PR - photoresist

RPM - rotations per minute

DRIE - deep reactive ion etch

IPA - 2-propanol

DI - deionized

He - helium

SF_6 - sulfur hexafluoride

C_4F_8 - octafluorocyclobutane

N_2O - nitrous oxide

sccm - standard cubic centimeter per minute

mT - milliTorr

Table A.1: Details of the fabrication process

Step	Name	Purpose	Details
1	Piranha Clean	remove organic material	10 minute clean in piranha bath, 80 to 100 °C
2	SiO_2 deposition		PECVD, at 200 or 300 °C, see note A
3	Oxygen plasma	activate SiO_2 surface	RIE, see note B
4	Deposit HMDS		puddle on wafer for 10 s, spin at 4000 RPM for 30 s
5	Deposit 1813 PR		spin at 500 RPM for 5 s, 4000 RPM for 30 s
6	Softbake	remove solvent from PR	90 °C for 1 min
7	Exposure		3.1 s at 20 mW/cm^2 with sodalime mask
8	Develop	remove exposed PR	352 developer, 30 s
9	Oxygen plasma	descum wafer	RIE, see note B
10	SiO_2 etch	pattern oxide	ICP-RIE, see note C
11	DRIE silicon etch	pattern silicon	see note D
12	Remove PR	clean wafer	800W in O_2 asher, 2 sccm O_2, 10 min
13	Deposit polymer	mold polymer features	pour over wafer and degas at 10 T for 15 min
14	Cure polymer		120 °C for 15 min, or other time and temperature
15	Remove excess polymer	planarize polymer to wafer	use stainless steel razor blade
16	Solvent clean	remove residual polymer	see note E
17	BHF soak	remove oxide mask	soak in 6:1 BHF, 1 min
18	Oxygen plasma	activate SiO_2 surface	RIE, see note B
19	SiO_2 deposition		PECVD, at 200 or 300 °C, see note A
20	Oxygen plasma	activate SiO_2 surface	RIE, see note B
21	Deposit 1813 PR		spin at 500 RPM for 5 s, 4000 RPM for 30 s
22	Softbake	remove solvent from PR	90 °C for 1 min
23	Exposure		3.1 s at 20 mW/cm^2 with sodalime mask

24	Develop	remove exposed PR	352 developer, 30 s
25	Oxygen plasma	descum wafer	RIE, see note B
26	SiO_2 etch	pattern oxide	ICP-RIE, see note C
27	DRIE silicon etch	pattern silicon	see note D
28	Deposit 1813 PR	coat wafer with PR	spin at 500 RPM 5 s, 1000 RPM for 30 s
29	Soft bake	remove solvent from PR	90 °C for 5 min
30	Spin PR on backside	deposit backside mask PR	spin at 500 RPM for 15 s, 1000 RPM for 1 min
31	Soft bake	remove solvent from PR	90 °C for 15 min
32	pause process	rehydration of PR	wait 3 hours
33	Exposure		30 s at 20 mW/cm^2 with sodalime mask
34	Develop	pattern PR	MF CD-26 developer, 2 min 30 s
35	Spin SPR 220.7 PR	prepare handle wafer	spin at 500 RPM for 15 s, 1000 RPM for 1 min
36	Bond wafer		place SOI wafer topside down on handle wafer
37	Bake	remove solvent from PR, bond wafer	90 °C for 5 min
38	Oxygen plasma	descum wafer	RIE, see note B
39	DRIE silicon etch	pattern silicon	see note D
40	Separate wafers		heat to 90 °C and manual separate wafers
41	Solvent rinse	remove PR	acetone, methanol, IPA
42	Oxygen plasma	descum wafer	RIE, see note B
43	Dice wafer	separate individual dies on wafer	
44	Release mechanisms		18:1 BHF, with agitation
45	Soak in IPA	prevent stiction, remove BHF	soak in IPA for 1 hr
46	Dry die	remove IPA	heat to 70 °C

Notes:

A. The PECVD process begins with a 30 s N_2O clean with a 1000 mT chamber pressure, power of 50 W, and N_2O flow rate of 710 sccm. The oxide deposition process has a chamber pressure of 1000 mT, power of 50 W, 5%SiH_4/95%N_2 flow rate of 170 sccm, and an N_2O flow rate of 710 sccm. For a 200 nm thick film, a deposition time of 2 min 47 s was used.

B. This 30 s RIE plasma has a chamber pressure of 100 mT, power of 50 W, and O_2 flow rate of 50 sccm.

C. The plasma to pattern oxide was a 9 minute etch with a 1 mT chamber pressure, DC power of 50 W, ICP power of 100 W, C_4F_8 flow rate of 10 sccm, He flow rate of 10 sccm, and had backside He cooling at 12 sccm.

D. The DRIE alternates between an etch and a passivation phase. The etch phase was 10 s long, had a SF_6 flow rate of 130 sccm, an O_2 flow rate of 13 sccm, a power of 600 W on the 13.56 MHz generator, and a power of 17 W on the 380 kHz on the LF generator. The passivation phase was 6 s long, had a C_4F_8 flow rate of 85 sccm, a power of 600 W on the 13.56 MHz generator, and a power of 0 W on the 380 kHz on the LF generator. The entire process used backside He cooling at 8 T with a maximum allowable leak rate of 5 mT/min. The results of the etch are shown in Figure A.1 which demonstrates the slightly re-entrant profile of the etch. A re-entrant profile, one where the bottom of the trench is wider than the top of the trench. It was necessary to design an etch process

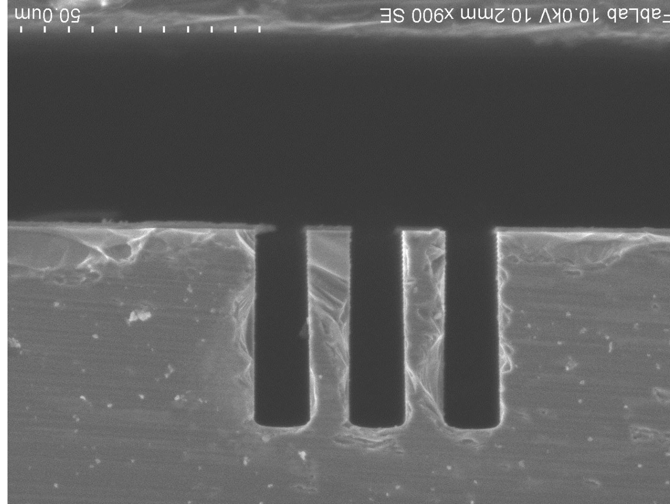

Figure A.1: SEM of the cross section of trenches etched in a silicon wafer demonstrating the trench profile.

with a re-entrant profile for the silicon etch used to mold the polymer features. If instead of a re-entrant profile the trenches had a v-shaped profile where the top of the trench was wider than the bottom of the trench, it is possible that small segments of silicon would remain un-etched. This un-etched silicon would be the silicon at the bottom of the v-shaped trench and would effectively be masked by the refilled polymer in any subsequent etch steps.

In addition to the profile of the etch, it was necessary to consider the width of the trenches being etched. If features with a small width were located near features with a large width, the aspect ratio dependency of the DRIE process would result in a slower etch rate in the smaller features than in the larger features, as shown in Figure A.2. This is because it is more difficult for the reactive gases to access smaller features than larger features [75, 189].

E. The solvent clean to remove the residual polymer was a 1 minute soak in a 3:1 mixture of n-methylpyrrolidone and tetrabutylammonium fluoride. After the

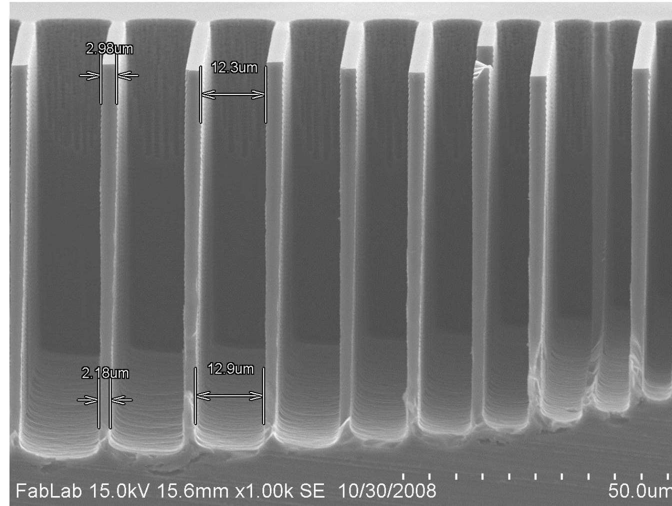

Figure A.2: SEM of the cross section of trenches etched in a silicon wafer demonstrating the ARDE.

soak, the wafer was cleaned with IPA and DI water.

Appendix B

Data from the Calibration of the Microscale Devices

As described in Chapter 2, there were two constants that had to be experimentally determined in order to calibrate the *in situ* test structure. The first constant was the capacitive constant, k_c, or slope of the linear fit of the measured change in capacitance versus displacement points. This is a linear relationship, so a simple linear fit can be used. The devices tested came from two wafers, and because of some of the variations in the silicon etch process there were slight differences between the constants from one wafer to the next. The purpose of this calibration process, however, is to account for any variations between wafers or from one die to another. The data for the two wafers is presented in Figure B.1. The average slope for the devices from Wafer A was 34.5 μm/pF ($\sigma = 0.44$) and the average slope for the devices from Wafer B was 29.3 μm/pF ($\sigma = 1.22$).

The second constant was the relationship between the displacement of the comb drive as a function of the input voltage, or k_{Vx}. In order to satisfy the derivation from Chapter 2, the relationship of interest was the slope of the displacement versus voltage squared points. This again is a linear relationship, so a simple linear fit can be used. As before, there were slight variations between the devices from the two wafers used. The average slope for the devices from Wafer A 163 $\mathrm{V}^2/\mu\mathrm{m}(\sigma = 13.5)$ and the average slope for the devices from Wafer B was 105 $\mathrm{V}^2/\mu\mathrm{m}(\sigma = 15.5)$. The devices from Wafer A had a slight offset, but the slope was the value of interest, so variations in the intercept were not an issue.

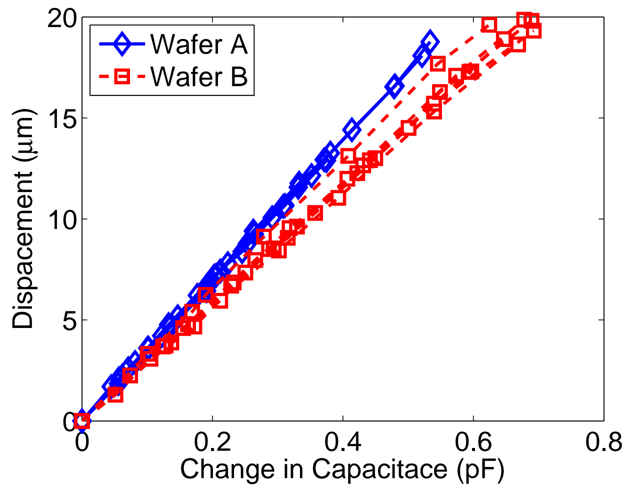

Figure B.1: Plot of the calibration data used to determine the capacitance as a function of displacement.

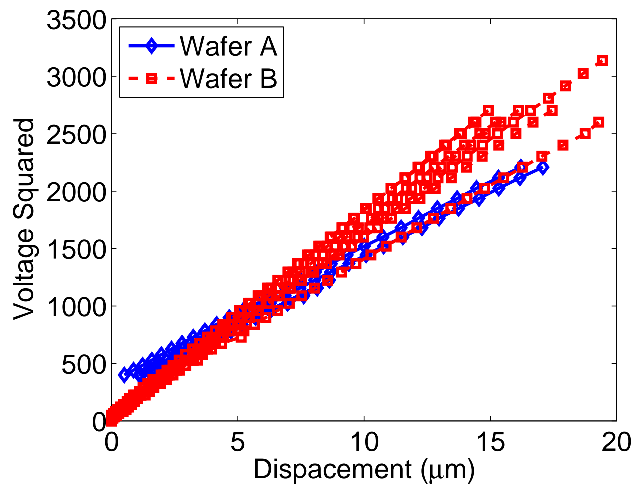

Figure B.2: Plot of the calibration data used to determine the flexure spring constant.

Appendix C

MATLAB Code for Image Processing

The following is the code that was used in Section 2.1 to analyze the displacement of the patterned feature on the *in situ* test mechanism. The code is based on the theory used in the "nano+" metrology software for MEMS characterization (lmis2.epfl.ch/nanoplus) by Christophe Yamahata [63], which can analyze video files. The theory behind the program was used and was highly simplified for analysis of a series of images by Ivan Penskiy in the Micro Robotics Laboratory at the University of Maryland, College Park.

```
1  % Setup
2  clear all
3  clc
4
5  % Create a list of all of the the TIF files in the current
      directory to be analyzed
6  path_im = '';
7  im_list = ls([path_im '*.tif']);
8
9  % Determined the number of TIF files to be analyzed
10 nFrames = size(im_list,1);
11
12 % Read in the first image to an array
13 fr = imread([path_im im_list(1,:)]);
14 % Convert the RGB image to grayscale image
15 fr_gr = rgb2gray(fr);
16 % Convert grayscale images to intensity values
17 fr_n=imadjust(fr_gr);
18 % Display the intensity values as an image
19 imshow(fr_n);
20 % Create a draggable rectangel on the intensity value image
```

```
21 h = imrect;
22 % Waits until the rectangle is created, double clicking
      inside the image resumes execution of the script, reads
      rectangle position to variable
23 position = wait(h);
24
25 % Sets width of rectangle in pixels to variable N
26 N = position(3);
27
28 % Creates an array of zeros the size of the number of frames
29 angl = zeros(nFrames, 1);
30 % Create a variable of the size of the fft
31 nfft = 2^(nextpow2(N));
32 % Set number of interference patterns included in the drawn
      rectangle
33 T_sample = 5;
34 % Set actual physical with of T_sample interference patterns
35 window_size = 35;
36
37 % Peek-peek distance in pixels
38 ppx=N*T_sample/window_size;
39
40 % The maximum frequency
41 n_max = round(nfft/ppx) + 1;
42
43 % Process each images
44 for i=1:nFrames
45     % Read in the i-th image
46     fr = imread([path_im im_list(i,:)]);
47
48     % Crop the position of the rectangle used earlier
49     fr_cr=imcrop(fr,position); %moving part
50     % Convert cropped image to gratscale
51     fr_gr = rgb2gray(fr_cr);
52     % Create intensity plot of cropped image
53     fr_n=imadjust(fr_gr);
54
55     % Sum the intensity plot by column of pixels
56     fr_intens = sum(fr_n,1);
57
58     if i==1
59                 fr_intens_first = fr_intens;
```

```
60                  % Perform fft on the summed intensity data
61                  fr_intens_first =
                       fft(fr_intens_first(:,1),N);
62
63                  % Will be used for zero padding
64                  mid_grey_level = mean(fr_intens_first);
65
66                  % Find beginning of image
67                  x_begin = round((nfft-N)/2)+1;
68                  % Find end of image
69                  x_end = x_begin - 1 + N;
70                  % Create array size of the image
71                  x = 1:1:nfft;
72      end
73
74      % Create array of average values for entire image
75      fr_intens_nfft = mid_grey_level*ones(1,nfft)';
76      % Update fft values for analyzed area
77      fr_intens_nfft(x_begin:1:x_end) = fr_intens(1:1:N);
78
79      % Perform fft
80      fr_intens = goertzel(fr_intens_nfft(:,1),n_max);
81      % Determine phase angles (radians)for each image
82      angl(i) = angle(fr_intens);
83
84  end
85
86  % Calculate change in phase angle from first image
87  % Sign convention: A displacement to the right is (+)
88  angl=angl(1)-angl;
89  % Correctphase angles
90  uangl=unwrap(angl);
91  % Compute Actual Displacement
92  disp=(T_sample*uangl/(2*pi));
```

Appendix D

ANSYS Code

The following is the code used in Section 3.3.3 to model the behavior of the DEAs in ANSYS. The convergence tolerance (CNVTOL) was set to 1e-3 for 0 to 800 V. It had to be increased to 1e-2 for 900 V and 1e-1 for 1000 V. The solution would not converge at 1100 V at 1e-1, but the CNVTOL was not increased further.

```
finish
/clear,start
/output,term

/prep7
eps0=8.854e-6 ! free space permittivity

!set the applied voltage
voltage=100

!set layer thickness
t=20
!set length of actuator
w=1000
!set nodesize, relative to layer thickness
nodesize=t/3

!build geometry
blc4,0,0,w,t
blc4,0,t,w,t
blc4,0,2*t,w,t
blc4,0,3*t,w,t
blc4,0,4*t,w,t

!set element types and material properties
!electrode layers
```

```
ET,1,plane223,1001
emunit,epzro,eps0
mp,perx,1,2.94
mp,ex,1,1.16
mp,prxy,1,0.49999

!dielectric layers
ET,2,plane223,1001
emunit,epzro,eps0
mp,perx,2,2.94
mp,ex,2,0.2
mp,prxy,2,0.49999

!select the electrode layer areas
asel,s,loc,y,0,t
asel,a,loc,y,2*t,3*t
asel,a,loc,y,4*t,5*t

!apply materials to areas and mesh electrode layers
aatt,1,,1
esize,nodesize
amesh,all

!select the dielectic layer areas
asel,s,loc,y,t,2*t
asel,a,loc,y,3*t,4*t

!apply materials to areas and mesh dielectric layers
aatt,2,,2
esize,nodesize
amesh,all

!merge points so that layers will move together
nummrg,all

/solu

!setup solution
antype,static
cnvtol,f,1,1e-3

!set the bottom electrode to voltage
```

```
nsel,s,loc,y,0,t
d,all,volt,voltage

!set the middle electrode to voltage=0
nsel,s,loc,y,2*t,3*t
d,all,volt,0

!fix the base of the actuator in x and y
nsel,s,loc,x,0
d,all,ux,0
d,all,uy,0

!enable nlgeom for large strains
nlgeom,on

!solve
alls
solve
fini
```

Bibliography

[1] R. P. Feynman. There's plenty of room at the bottom. *Journal of Microelectromechanical Systems*, 1(1):60–66, 1992.

[2] J. Kilby. Miniature semicontuctor integrated circuit. U.S. patent 3,115,581, Dallas, Texas, December 1963.

[3] K. E. Petersen. Silicon as a mechanical material. *Proceedings of the IEEE*, 70(5):420–457, 1982.

[4] A. M. Flynn. Gnat robots (and how they will change robotics). Working paper 295, Massachesetts Institute of Technology, Hyannis, MA, 1987.

[5] Q. Pan, S. Guo, and T. Okada. A novel hybrid wireless microrobot. *International Journal of Mechatronics and Automation*, 1(1):60–69, 2011.

[6] Z. Wang, G. Hang, J. Li, Y. Wang, and K. Xiao. A micro-robot fish with embedded SMA wire actuated flexible biomimetic fin. *Sensors and Actuators A: Physical*, 144(2):354–360, 2008.

[7] C. Pawashe, S. Floyd, and M. Sitti. Multiple magnetic microrobot control using electrostatic anchoring. *Applied Physics Letters*, 94(16):164108, 2009.

[8] K. Vollmers, D. R. Frutiger, B. E. Kratochvil, and B. J Nelson. Wireless resonant magnetic microactuator for untethered mobile microrobots. *Applied Physics Letters*, 92(14):144103–144103, 2008.

[9] L. Zhang, J. J. Abbott, L. Dong, B. E. Kratochvil, D. Bell, and B. J. Nelson. Artificial bacterial flagella: Fabrication and magnetic control. *Applied Physics Letters*, 94(6):064107, 2009.

[10] A. Ghosh and P. Fischer. Controlled propulsion of artificial magnetic nanostructured propellers. *Nano Letters*, 9(6):2243–2245, 2009.

[11] S. Martel and M. Mohammadi. Using a swarm of self-propelled natural microrobots in the form of flagellated bacteria to perform complex micro-assembly tasks. In *IEEE International Conference on Robotics and Automation*, pages 500–505, Montreal, QC, Canada, May 2010.

[12] S. Martel, M. Mohammadi, O. Felfoul, Z. Lu, and P. Pouponneau. Flagellated magnetotactic bacteria as controlled MRI-trackable propulsion and steering systems for medical nanorobots operating in the human microvasculature. *The International Journal of Robotics Research*, 28(4):571–582, 2009.

[13] H. Sato and M. M. Maharbiz. Recent developments in the remote radio control of insect flight. *Frontiers in Neuroscience*, 4:1–12, 2010.

[14] T. Latif and A. Bozkurt. Line following terrestrial insect biobots. In *International Conference of the IEEE Engineering in Medicine and Biology Society*, San Diego, CA, USA, September 2012.

[15] R. J. Wood. The first takeoff of a biologically inspired at-scale robotic insect. *IEEE Transactions on Robotics*, 24(2):341–347, 2008.

[16] T. Ebefors, J. U. Mattsson, E. Kalvesten, and D. Stemme. A walking silicon microrobot. In *International Conference on Solid-State Sensors, Actuators, and Microsystems (Transducers)*, pages 1202–1205, Sendai, Japan, June 1999.

[17] S. Hollar, S. Bergbreiter, and K. S. J. Pister. Bidirectional inchworm motors and two-DOF robot leg operation. In *International Conference on Solid-State Sensors, Actuators, and Microsystems (Transducers)*, pages 262–267, Boston, MA, USA, June 2003.

[18] H. Tanaka, K. Matsumoto, and I. Shimoyama. Design and performance of micromolded plastic butterfly wings on butterfly ornithopter. In *IEEE International Conference on Intelligent Robots and Systems*, pages 3095–3100, Nice, France, September 2008.

[19] B. R. Donald, C. G. Levey, C. D. McGray, I. Paprotny, and D. Rus. An untethered, electrostatic, globally controllable MEMS microrobot. *Journal of Microelectromechanical Systems*, 15(1):1–15, 2006.

[20] R. J. Wood, S. Avadhanula, M. Menon, and R. S. Fearing. Microrobotics using composite materials: the micromechanical flying insect thorax. In *IEEE International Conference on Robotics and Automation*, pages 1842–1849, Barcelona, Spain, September 2003.

[21] L. M. Roylance and J. B. Angell. A batch-fabricated silicon accelerometer. *IEEE Transactions on Electron Devices*, 26(12):1911–1917, 1979.

[22] J. S. Aden, J. H. Bohrquez, D. M. Collins, and M. D. Crook. The third-generation HP thermal inkjet printhead. *Hewlett Packard Journal*, 45:41–45, 1994.

[23] P. F. Van Kessel, L. J. Hornbeck, R. F. Meier, and M. R. Douglass. A MEMS-based projection display. *Proceecings of the IEEE*, 86(8):1687–1704, 1998.

[24] S. Bergbreiter, D. Mahajan, and K. S. J. Pister. A reusable micromechanical energy storage/quick release system with assembled elastomers. *Journal of Micromechanics and Microengineering*, 19(5):055009, 2009.

[25] S. H. Kim, J. Engel, C. Liu, and D. L. Jones. Texture classification using a polymer-based MEMS tactile sensor. *Journal of Micromechanics and Microengineering*, 15:912–920, 2005.

[26] Y. Suzuki and Y.-C. Tai. Micromachined high-aspect-ratio parylene spring and its application to low-frequency accelerometers. *Journal of Microelectromechanical Systems*, 15(5):1364–1370, 2006.

[27] N.-T. Nguyen, S.-S. Ho, and C. Low. A polymeric microgripper with integrated thermal actuators. *Journal of Micromechanics and Microengineering*, 14(7):969–974, 2004.

[28] M. A. Hopcroft, W. D. Nix, and T. W. Kenny. What is the young's modulus of silicon? *Journal of Microelectromechanical Systems*, 19(2):229–238, 2010.

[29] J. D. Williams and W. Wang. Study on the postbaking process and the effects on UV lithography of high aspect ratio SU-8 microstructures. *Journal of Micro/Nanolithography, MEMS, and MOEMS*, 3(4):563–568, 2004.

[30] X. Yang, C. Grosjean, and Y.-C. Tai. Design, fabrication, and testing of micromachined silicone rubber membrane valves. *Journal of Microelectromechanical Systems*, 8(4):393–402, 1999.

[31] D. C. Duffy, J. C. McDonald, O. J. A. Schueller, and G. M. Whitesides. Rapid prototyping of microfluidic systems in poly(dimethylsiloxane). *Analytical Chemistry*, 70(23):4974–4984, 1998.

[32] J. C. Lotters, W. Olthuis, P. H. Veltink, and P. Bergveld. Design, realization and characterization of a symmetrical triaxial capacitive accelerometer for medical applications. *Sensors and Actuators A: Physical*, 61(1-3):303–308, 1997.

[33] Y.-C. Tung and K. Kurabayashi. A single-layer PDMS-on-silicon hybrid microactuator with multi-axis out-of-plane motion capabilities - part II: fabrication and characterization. *Journal of Microelectromechanical Systems*, 14(3):558–566, 2005.

[34] S. Bergbreiter and K. S. J. Pister. Elastomer-based micromechanical energy storage system. In *ASME International Mechanical Engineering Congress and Exposition*, pages 539–545, Chicago, Il., USA, November 2006.

[35] C. Liu. Recent developments in polymer MEMS. *Advanced Materials*, 19(22):3783–3790, 2007.

[36] P.-Y. Li, T. K. Givrad, D. P. Holschneider, J.-M. I. Maarek, and E. Meng. A parylene MEMS electrothermal valve. *Journal of Microelectromechanical Systems*, 18(6):1184–1197, 2009.

[37] Z. Fan, J. M. Engel, J. Chen, and C. Liu. Parylene surface-micromachined membranes for sensor applications. *Journal of Microelectromechanical Systems*, 13(3):484–490, 2004.

[38] T. Ebefors, E. Klvesten, and G. Stemme. New small radius joints based on thermal shrinkage of polyimide in v-grooves for robust self-assembly 3D microstructures. *Journal of Micromechanics and Microengineering*, 8(3):188–194, 1998.

[39] S. Y. Xiao, L. F. Che, X. X. Li, and Y. L. Wang. A novel fabrication process of MEMS devices on polyimide flexible substrates. *Microelectronic Engineering*, 85(2):452–457, 2008.

[40] A. Mata, A. Fleischman, and S. Roy. Characterization of polydimethylsiloxane (PDMS) properties for biomedical micro/nanosystems. *Biomedical Microdevices*, 7(4):281–293, 2005.

[41] T. Adrega and S. P. Lacour. Stretchable gold conductors embedded in PDMS and patterned by photolithography: fabrication and electromechanical characterization. *Journal of Micromechanics and Microengineering*, 20(5):055025, 2010.

[42] Y. Xia and G. M. Whitesides. Soft lithography. *Annual Review of Materials Science*, 28(1):153–184, 1998.

[43] M. A. Unger, H.-P. Chou, T. Thorsen, A. Scherer, and S. R. Quake. Monolithic microfabricated valves and pumps by multilayer soft lithography. *Science*, 288(5463):113–116, 2000.

[44] A. P. Gerratt, I. Penskiy, and S. Bergbreiter. SOI/elastomer process for energy storage and rapid release. *Journal of Micromechanics and Microengineering*, 20(10):104011, 2010.

[45] I. Penskiy, A. P. Gerratt, and S. Bergbreiter. Friction, adhesion, and wear properties of PDMS coatings in MEMS devices. In *IEEE Conference on Micro Electro Mechanical Systems*, pages 440–444, Cancun, Mexico, January 2011.

[46] Y. Sun, B. Akhremitchev, and G. C. Walker. Using the adhesive interaction between atomic force microscopy tips and polymer surfaces to measure the elastic modulus of compliant samples. *Langmuir*, 20(14):5837–5845, 2004.

[47] F. Carrillo, S. Gupta, M. Balooch, S. J. Marshall, G. W. Marshall, L. Pruitt, and C. M. Puttlitz. Nanoindentation of polydimethylsiloxane elastomers: Effect of crosslinking, work of adhesion, and fluid environment on elastic modulus. *Journal of Materials Research*, 20(10):2820–2830, 2005.

[48] Q. Liao, J. Huang, T. Zhu, C. Xiong, and J. Fang. A hybrid model to determine mechanical properties of soft polymers by nanoindentation. *Mechanics of Materials*, 42(12):1043–1047, 2010.

[49] Y. Cao, D. Yang, and W. Soboyejoy. Nanoindentation method for determining the initial contact and adhesion characteristics of soft polydimethylsiloxane. *Journal of Materials Research*, 20(08):2004–2011, 2011.

[50] S. Gupta, F. Carrillo, C. Li, L. Pruitt, and C. Puttlitz. Adhesive forces significantly affect elastic modulus determination of soft polymeric materials in nanoindentation. *Materials Letters*, 61(2):448–451, 2007.

[51] F. Schneider, T. Fellner, J. Wilde, and U. Wallrabe. Mechanical properties of silicones for MEMS. *Journal of Micromechanics and Microengineering*, 18(6):065008, 2008.

[52] M. Kujawski, J. D. Pearse, and E. Smela. Elastomers filled with exfoliated graphite as compliant electrodes. *Carbon*, 48(9):2409–2417, 2010.

[53] J. C. Lotters, W. Olthuis, P. H. Veltink, and P. Bergveld. The mechanical properties of the rubber elastic polymer polydimethylsiloxane for sensor applications. *Journal of Micromechanics and Microengineering*, 7(3):145–147, 1999.

[54] A. L. Thangawng, R. S. Ruoff, M. A. Swartz, and M. R. Glucksberg. An ultra-thin PDMS membrane as a bio/micronano interface: fabrication and characterization. *Biomedical Microdevices*, 9(4):587–595, 2007.

[55] S.-H. Yoon, V. Reyes-Ortiz, K.-H. Kim, Y. H. Seo, and M. R. K. Mofrad. Analysis of circular PDMS microballoons with ultralarge deflection for MEMS design. *Journal of Microelectromechanical Systems*, 19(4):854–864, 2010.

[56] S. C. Truxal, Y.-C. Tung, and K. Kurabayashi. A flexible nanograting integrated onto silicon micromachines by soft lithographic replica molding and assembly. *Journal of Microelectromechanical Systems*, 17(2):393–401, 2008.

[57] W. A. Churaman, A. P. Gerratt, and S. Bergbreiter. First leaps toward jumping microrobots. In *IEEE/RSJ International Conference on Intelligent Robots and Systems*, pages 1680–1686, San Francisco, CA, USA, September 2011.

[58] A. P. Gerratt, I. Penskiy, and S. Bergbreiter. Integrated silicon-PDMS process for microrobot mechanisms. In *IEEE International Conference on Robotics and Automation*, pages 3153–3158, Anchorage, AK, USA, May 2010.

[59] J. N. Lee, C. Park, and G. M. Whitesides. Solvent compatibility of poly(dimethylsiloxane)-based microfluidic devices. *Analytical Chemistry*, 75(23):6544–6554, 2003.

[60] Information about dow corning brand silicone encapsulants. http://www2.dowcorning.com/DataFiles/090007c88020bcca.pdf, 2010.

[61] S.-H. Yoo, C. Cohen, and C.-Y. Hui. Mechanical and swelling properties of PDMS interpenetrating polymer networks. *Polymer*, 47(17):6226–6235, 2006.

[62] T. K. Kim, J. K. Kim, and O. K. Jeong. Measurement of nonlinear mechanical properties of PDMS elastomer. *Microelectronic Engineering*, 88(8):1982–1985, 2011.

[63] C. Yamahata, E. Sarajlic, G. J. M. Krijnen, and M. A. M. Gijs. Subnanometer translation of microelectromechanical systems measured by discrete fourier analysis of CCD images. *Journal of Microelectromechanical Systems*, 19(5):1273–1275, 2010.

[64] R. Avazmohammadi and R. Naghdabadi. Strain energy-based homogenization of nonlinear elastic particulate composites. *International Journal of Engineering Science*, 47(10):1038–1048, 2009.

[65] D. J. Charlton, J. Yang, and K. K. Teh. A review of methods to characterize rubber elastic behavior for use in finite element analysis. *Rubber Chemistry and Technology*, 67(3):481–503, 1994.

[66] R. W. Ogden. Large deformation isotropic elasticity: On the correlation of theory and experiment for compressible rubberlike solids. *Proceedings of the Royal Society of London. Series A, Mathematical and Physical Sciences*, 328(1575):567–583, 1972.

[67] F. Carpi, D. De Rossi, R. Kornbluh, R. Pelrine, and P. Sommer-Larsen. *Dielectric elastomers as electromechanical transducers: Fundamentals, materials, devices, models, and applications of an emerging electroactive polymer technology*. Elsevier, Amsterdam, 2008.

[68] G. Holzapfel. *Nonlinear Solid Mechanics: A Continuum Approach for Engineering*. John Wiley & Sons Ltd., 2000.

[69] L. Mullins. Softening of rubber by deformation. *Rubber*, 42(1):339–362, 1969.

[70] J. Diani, B. Fayolle, and P. Gilormini. A review on the mullins effect. *European Polymer Journal*, 45(3):601–612, 2009.

[71] A. Carre and M. E. R. Shanahan. Effect of cross-linking on the dewetting of an elastomeric surface. *Journal of Colloid and Interface Science*, 191(1):141–145, 1997.

[72] R. P. Wool and X. S. Sun. *Bio-Based Polymers and Composites*. Academic Press, Burlington, MA, 2005.

[73] M. Sen, A. Yakar, and O. Given. Determination of average molecular weight between cross-links mc from swelling behaviours of diprotic acid-containing hydrogels. *Polymer*, 40(11):2969–2974, 1999.

[74] S. A. McAuley, H. Ashraf, L. Atabo, A. Chambers, S. Hall, J. Hopkins, and G. Nicholls. Silicon micromachining using a high-density plasma source. *Journal of Physics D: Applied Physics*, 34(18):2769–2774, 2001.

[75] A. A. Ayn, R. Braff, C. C. Lin, H. H. Sawin, and M. A. Schmidt. Characterization of a time multiplexed inductively coupled plasma etcher. *Journal of the Electrochemical Society*, 146(1):339–349, 1999.

[76] Y. P. Khanna, E. A. Turi, T. J. Pedley, V. V. Vickroy, and R. F. Abbott. Dynamic mechanical relaxations in polyethylene. *Macromolecules*, 18(6):1302–1309, 1985.

[77] M. Ieda. Dielectric breakdown process of polymers. *IEEE Transactions on Electrical Insulation*, EI-15(3):206–224, 1980.

[78] P. Solomon. Breakdown in silicon oxide - a review. *Journal of Vacuum Science and Technology*, 14(5):1122–1130, 1977.

[79] C. M. Osburn and D. W. Ormond. Dielectric breakdown in silicon dioxide films on silicon. *Journal of the Electrochemical Society*, 150(1):G28–G32, 1971.

[80] Y. Murakami, T. Shiota, T. Shingyouji, and H. Abe. Effect of oxidation ambient on the dielectric breakdown characteristics of thermal oxide films of silicon. *Journal of Applied Physics*, 75(10):5302–5305, 1994.

[81] J. H. Ahn and J. H. Je. Stretchable electronics: materials, architectures and integrations. *Journal of Physics D: Applied Physics*, 45(10):103001, 2012.

[82] S. Rosset, M. Niklaus, P. Dubois, and H. R. Shea. Large-stroke dielectric elastomer actuators with ion-implanted electrodes. *Journal of Microelectromechanical Systems*, 18(6):1300–1308, 2009.

[83] A. P. Gerratt, B. Balakrisnan, I. Penskiy, and S. Bergbreiter. Batch fabricated bidirectional dielectric elastomer actuators. In *International Conference on Solid-State Sensors, Actuators, and Microsystems (Transducers)*, pages 2422–2425, Beijing, China, June 2011.

[84] S. J. A. Koh, T. Li, J. Zhou, X. Zhao, W. Hong, J. Zhu, and Z. Suo. Mechanisms of large actuation strain in dielectric elastomers. *Journal of Polymer Science Part B: Polymer Physics*, 49(7):504–515, 2011.

[85] P. Brochu and Q. Pei. Advances in dielectric elastomers for actuators and artificial muscles. *Macromolecular Rapid Communications*, 31(1):10–36, 2010.

[86] G. K. Lau, J. F. L. Goosen, F. Van Keulen, P. J. French, and P. M. Sarro. Actuated elastomers with rigid vertical electrodes. *Journal of Micromechanics and Microengineering*, 16(6):S35, 2006.

[87] P. J. Leask, R. A. Ibbotson, and S. J. Evans. An evaluation of dielectric materials for use in pulsed power devices. In *IEEE International Pulsed Power Conference*, pages 435–440, Washington, D.C., July 2009.

[88] J.-T. Feng and Y.-P. Zhao. Experimental observation of electrical instability of droplets on dielectric layer. *Journal of Physics D: Applied Physics*, 41(5):052004, 2008.

[89] M. Liu, J. Sun, Y. Sun, C. Bock, and Q. Chen. Thickness-dependent mechanical properties of polydimethylsiloxane membranes. *Journal of Micromechanics and Microengineering*, 19(3):035028, 2009.

[90] A. P. Gerratt and S. Bergbreiter. Incorporating compliant elastomers for jumping locomotion in microrobots. *Smart Materials and Structures*, 22(1):014010, 2013.

[91] J. Blok and D. G. LeGrand. Dielectric breakdown of polymer films. *Journal of Applied Physics*, 40(1):288–293, 1969.

[92] J. G. Drobny. *Polymers for electricity and electronics*. John Wiley & Sons, Inc., Hoboken, New York, 2012.

[93] F. Paschen. Ueber die zum funkenbergang in luft, wasserstoff und kohlensure bei verschiedenen drucken erforderliche potentialdifferenz. *Annalen der Physik*, 273(5):69–96, 1889.

[94] J. M. Torres and R. S. Dhariwal. Electric field breakdown at micrometre separations. *Nanotechnology*, 10(1):102–107, 1999.

[95] T. Ono, D. Y. Sim, and M. Esashi. Micro-discharge and electric breakdown in a micro-gap. *Journal of Micromechanics and Microengineering*, 10(3):445–451, 2000.

[96] F. W. Strong, J. L. Skinner, P. M. Dentinger, and N. C. Tien. Electrical breakdown across micron scale gaps in MEMS structures. In *Proceedings of SPIE: Reliability, Packaging, Testing, and Characterization of MEMS/MOEMS V*, volume 6111, page 611103, San Jose, CA, January 2006.

[97] F. W. Strong, J. L. Skinner, and N. C. Tien. Electrical discharge across micrometer-scale gaps for planar MEMS structures in air at atmospheric pressure. *Journal of Micromechanics and Microengineering*, 18(7):075025, 2008.

[98] C. H. Chen, J. A. Yeh, and P. J. Wang. Electrical breakdown phenomena for devices with micron separations. *Journal of Micromechanics and Microengineering*, 16(7):1366–1373, 2006.

[99] D. B. Go and D. A. Pohlman. A mathematical model of the modified paschens curve for breakdown in microscale gaps. *Journal of Applied Physics*, 107(10):103303, 2010.

[100] K. Burm. Calculation of the townsend discharge coefficients and the paschen curve coefficients. *Contributions to Plasma Physics*, 47(3):177–182, 2007.

[101] J. Huang, S. Shian, R. M. Diebold, Z. Suo, and D. R. Clarke. The thickness and stretch dependence of the electrical breakdown strength of an acrylic dielectric elastomer. *Applied Physics Letters*, 101(12):122905, 2012.

[102] W. Dai and Y.-P. Zhao. The nonlinear phenomena of thin polydimethylsiloxane (PDMS) films in electrowetting. *International Journal of Nonlinear Sciences and Numerical Simulation*, 8(4):519–526, 2007.

[103] G. Kofod, P. Sommer-Larsen, R. Kornbluh, and R. Pelrine. Actuation response of polyacrylate dielectric elastomers. *Journal of Intelligent Materials Systems and Structures*, 14(12):787–793, 2003.

[104] P. J. Leask. Pulse breakdown strengths of liquid, gel and solid insulating materials using closely spaced spherical electrodes. *Acta Physica Polonica. Series A: General Physics*, 115(6):998–1000, 2009.

[105] Z. Wang, J. K. Nelson, J. Miao, R. J. Linhardt, L. S. Schadler, H. Hillborg, and S. Zhao. Effect of high aspect ratio filler on dielectric properties of polymer composites: a study on barium titanate fibers and graphene platelets. *IEEE Transactions on Dielectrics and Electrical Insulation*, 19(3):960–967, 2012.

[106] K. Horiuchi and P. Dutta. Electrokinetic flow control in microfluidic chips using a field-effect transistor. *Lab on a Chip*, 6(6):714–723, 2006.

[107] A. K. Price, K. M. Anderson, and C. T. Culbertson. Demonstration of an integrated electroactive polymer actuator on a microfluidic electrophoresis device. *Lab on a Chip*, 9(14):2076–2084, 2009.

[108] J. C. McDonald and G. M. Whitesides. Poly(dimethylsiloxane) as a material for fabricating microfluidic devices. *Accounts of Chemical Research*, 35(7):491–499, 2002.

[109] X. Z. Niu, S. L. Peng, L. Y. Liu, W. J. Wen, and P. Sheng. Characterizing and patterning of PDMS-Based conducting composites. *Advanced Materials*, 19(18):2682–2686, 2007.

[110] J. M. Engel, N. Chen, K. Ryu, S. Pandya, C. Tucker, Y. Yang, and C. Liu. Multi-layer embedment of conductive and non-conductive PDMS for all-elastomer MEMS. In *Solid State Sensors, Actuator, and Microsystems Workshop*, pages 316–319, Hilton Head, SC, USA, June 2006.

[111] S.P. Lacour, J. Jones, S. Wagner, T. Li, and Z. Suo. Stretchable interconnects for elastic electronic surfaces. *Proceedings of the IEEE*, 93(8):1459–1467, 2005.

[112] J. A. Rogers and Y. Huang. A curvy, stretchy future for electronics. *Proceedings of the National Academy of Sciences*, 106(27):10875–10876, 2009.

[113] E. Guth. Theory of filler reinforcement. *Journal of Applied Physics*, 16(1):20–25, 1945.

[114] S. P. Rwei, F.-H. Ku, and K.-C. Cheng. Dispersion of carbon black in a continuous phase: Electrical, rheological, and morphological studies. *Colloid & Polymer Science*, 280(12):1110–1115, 2002.

[115] H. Yamada, I. Manas-Zloczower, and D. L. Feke. Influence of matrix infiltration on the dispersion kinetics of carbon black agglomerates. *Powder technology*, 92(2):163–169, 1997.

[116] J. E. Mark. Some unusual elastomers and experiments on rubberlike elasticity. *Progress in Polymer Science*, 28(8):1205–1221, 2003.

[117] F. Hamouda, H. Sahaf, S. Held, G. Barbillon, P. Gogol, E. Moyen, A. Aassime, J. Moreau, M. Canva, J.-M. Lourtioz, M. Hanbcken, and B. Bartenlian. Large area nanopatterning by combined anodic aluminum oxide and soft UVNIL technologies for applications in biology. *Microelectronic Engineering*, 88(8):2444–2446, 2011.

[118] N. Koo, M. Bender, U. Plachetka, A. Fuchs, T. Wahlbrink, J. Bolten, and H. Kurz. Improved mold fabrication for the definition of high quality nanopatterns by soft UV-Nanoimprint lithography using diluted PDMS material. *Microelectronic Engineering*, 84(5-8):904–908, 2007.

[119] H. Kang, J. Lee, J. Park, and H. H. Lee. An improved method of preparing composite poly(dimethylsiloxane) moulds. *Nanotechnology*, 17(1):197–200, 2006.

[120] L. Z. Rogovina and V. G. Vasilev. Diversity of polymer gels and the main factors determining the properties of gels and related solid polymers. *Polymer Science Series A*, 52(11):1171–1183, 2010.

[121] K. Urayama, K. Yokoyama, and S. Kohjiya. Low-temperature behavior of deswollen poly(dimethylsiloxane) networks. *Polymer*, 41(9):3273–3278, 2000.

[122] L. Wang, F. Ma, Q. Shi, H. Liu, and X. Wang. Study on compressive resistance creep and recovery of flexible pressure sensitive material based on carbon black filled silicone rubber composite. *Sensors and Actuators A: Physical*, 165(2):207–215, 2011.

[123] C. W. Lee. Effect of binary conductive agents in spinel LiMn2O4 cathodes of electrochemical performance of li-ion batteries. *Journal of Industrial and Engineering Chemistry*, 12(6):967–971, 2006.

[124] W. Y. Zhang, G. S. Ferguson, and S. Tatic-Lucic. Elastomer-supported cold welding for room temperature wafer-level bonding. In *IEEE Conference on Micro Electro Mechanical Systems*, pages 741–744, Maastricht, The Netherlands, January 2004.

[125] P. Lotz, M. Matysek, P. Lechner, M. Hamann, and H. F. Schlaak. Dielectric elastomer actuators using improved thin film processing and nanosized particles. In *Proceedings of SPIE, Electroactive Polymer Actuators and Devices*, volume 6927, page 692723, San Diego, California, USA, 2008.

[126] E. A. Waddell, S. Shreeves, H. Carrell, C. Perry, B. A. Reid, and J. McKee. Surface modification of sylgard 184 polydimethylsiloxane by 254 nm excimer radiation and characterization by contact angle goniometry, infrared spectroscopy, atomic force and scanning electron microscopy. *Applied Surface Science*, 254(17):5314–5318, 2008.

[127] Y. Okada and Y. Tokumaru. Precise determination of lattice parameter and thermal expansion coefficient of silicon between 300 and 1500 k. *Journal of Applied Physics*, 56(2):314–320, 1984.

[128] A. Govindaraju, A. Chakraborty, and C. Luo. Reinforcement of PDMS masters using SU-8 truss structures. *Journal of Micromechanics and Microengineering*, 15(6):1303, 2005.

[129] T. Maleki, G. Chitnis, A. Panja, and B. Ziaie. Single-layer elastomeric out-of-plane actuator with asymmetric surface profile. In *Solid State Sensors, Actuator, and Microsystems Workshop*, pages 408–411, Hilton Head Island, SC, USA, June 2010.

[130] T. Maleki, G. Chitnis, and B. Ziaie. A batch-fabricated laser-micromachined PDMS actuator with stamped carbon grease electrodes. *Journal of Micromechanics and Microengineering*, 21(2):027002, 2011.

[131] J. J. Loverich, I. Kanno, and H. Kotera. Concepts for a new class of all-polymer micropumps. *Lab on a Chip*, 6(9):1147–1154, 2006.

[132] B. F. Sorensen. Thermally induced delamination of symmetrically graded multilayers. *Journal of the American Ceramic Society*, 85(4):858–864, 2002.

[133] H. Cong and T. Pan. Photopatternable conductive PDMS materials for microfabrication. *Advanced Functional Materials*, 18(13):1912–1921, 2008.

[134] C.-X. Liu and J.-W. Choi. Patterning conductive PDMS nanocomposite in an elastomer using microcontact printing. *Journal of Micromechanics and Microengineering*, 19(8):085019, 2009.

[135] J. M. Maloney, D. S. Schreiber, and D. L. DeVoe. Large-force electrothermal linear micromotors. *Journal of Micromechanics and Microengineering*, 14(2):226–234, 2004.

[136] C.-S. Huang, Y.-T. Cheng, J. Chung, and W. Hsu. Investigation of ni-based thermal bimaterial structure for sensor and actuator application. *Sensors and Actuators A: Physical*, 149(2):298–304, 2009.

[137] J. M. Richards, G. H. Wostenholm, B. Yates, M. I. Darby, and L. N. Phillips. Thermal properties of carbon-filled silicone rubbers for use in thermal expansion moulding. *Journal of Materials Science*, 25(1):721–724, 1990.

[138] W. G. Young and R. G. Budynas. *Roarks Formulas for Stress and Strain*. McGraw Hill, New York, 2002.

[139] R. Saha and W. D. Nix. Effects of the substrate on the determination of thin film mechanical properties by nanoindentation. *Acta Materialia*, 50(1):23–38, 2002.

[140] A. O'Halloran, F. O'Malley, and P. McHugh. A review on dielectric elastomer actuators, technology, applications, and challenges. *Journal of Applied Physics*, 104(7):071101, 2008.

[141] R. Shankar, T. K. Ghosh, and R. J. Spontak. Dielectric elastomers as next-generation polymeric actuators. *Soft Matter*, 3(9):1116–1129, 2007.

[142] L. Lampani and P. Gaudenzi. 3D finite element analysis of multilayer dielectric elastomer actuators with metallic compliant electrodes for space applications. *Journal of Intelligent Material Systems and Structures*, 21:621–632, 2010.

[143] F. Carpi, A. Khanicheh, C. Mavroidis, and D. De Rossi. MRI compatibility of silicone-made contractile dielectric elastomer actuators. *IEEE/ASME Transactions on Mechatronics*, 13(3):370–374, 2008.

[144] B. Balakrisnan, S. Patil, and E. Smela. Patterning PDMS using a combination of wet and dry etching. *Journal of Micromechanics and Microengineering*, 19(4):047002, 2009.

[145] S. Michel, X. Q. Zhang, M. Wissler, C. Lowe, and G. Kovacs. A comparison between silicone and acrylic elastomers as dielectric materials in electroactive polymer actuators. *Polymer International*, 59(3):391–399, 2010.

[146] C.-P. Chang, C.-D. Liu, S.-W. Huang, D.-Y. Chao, and S.-N. Lee. Synthesis and characterization of high dielectric constant polyaniline/polyurethane blends. *Synthetic Metals*, 142(1-3):275–281, 2004.

[147] R. Pelrine. High-speed electrically actuated elastomers with strain greater than 100%. *Science*, 287(5454):836–839, 2000.

[148] B. Balakrisnan and E. Smela. Challenges in the microfabrication of dielectric elastomer actuators. In Y. Bar-Cohen, editor, *Proceedings of SPIE*, volume 7642, page 76420K, San Diego, CA, USA, 2010.

[149] G. Kofod. The static actuation of dielectric elastomer actuators: how does prestretch improve actuation? *Journal of Physics D: Applied Physics*, 41(21):111, 2008.

[150] MRTV 9 high tear mold making RTV silicone data sheet. Data sheet, Insulcast, February 2004.

[151] D. L. DeVoe and A. P. Pisano. Modeling and optimal design of piezoelectric cantilever microactuators. *Journal of Microelectromechanical Systems*, 6(3):266–270, 1997.

[152] R. J. Full and M. S. Tu. Mechanics of a rapid running insect: two-, four- and six-legged locomotion. *The Journal of Experimental Biology*, 156:215–231, 1991.

[153] T. Seidl and R. Wehner. Walking on inclines: how do desert ants monitor slope and step length. *Frontiers in Zoology*, 5(1):8, 2008.

[154] H. C. Bennet-Clark and E. C. A. Lucey. The jump of the flea: a study of the energetics and a model of the mechanism. *The Journal of Experimental Biology*, 47:59–76, 1967.

[155] M. Burrows. Froghopper insects leap to new heights. *Nature*, 424:509, 2003.

[156] P. Dario, R. Valleggi, M. C. Carrozza, M. C. Montesi, and M. Cocco. Microactuators for microrobots: a critical survey. *Journal of Micromechanics and Microengineering*, 2(3):141–157, 1992.

[157] W. S. N. Trimmer. Microrobots and micromechanical systems. *Sensors and Actuators*, 19(3):267–287, 1989.

[158] R. Yeh, E. J. J. Kruglick, and K. S. J. Pister. Surface-micromachined components for articulated microrobots. *Journal of Microelectromechanical Systems*, 5(1):10–17, 1996.

[159] E. Y. Erdem, Y.-M. Chen, M. Mohebbi, J. W. Suh, G. T. A Kovacs, R. B. Darling, and K. F. Bohringer. Thermally actuated omnidirectional walking microrobot. *Journal of Microelectromechanical Systems*, 19(3):433–442, 2010.

[160] H. C. Bennet-Clark. Energy storage in jumping insects. In H. R. Hepburn, editor, *The Insect Integument*, pages 421–443. Elsevier Scientific Publishing Company, Amsterdam, 1976.

[161] S. Kim. iSprawl: design and tuning for high-speed autonomous open-loop running. *The International Journal of Robotics Research*, 25(9):903–912, 2006.

[162] U. Saranli, M. Buehler, and D. E. Koditschek. RHex: a simple and highly mobile hexapod robot. *International Journal of Robotics Research*, 20(7):616–631, 2001.

[163] S. Bergbreiter. Effective and efficient locomotion for millimeter-sized microrobots. In *IEEE International Conference on Intelligent Robots and Systems*, pages 4030–4035, Nice, France, September 2008.

[164] P. Fiorini and J. Burdick. The development of hopping capabilities for small robots. *Autonomous Robots*, 14(23):239–254, 2003.

[165] W. Nachtigall. Some aspects of reynolds number effects in animals. *Mathematical Methods in the Applied Sciences*, 24(17-18):1401–1408, 2001.

[166] S. Bergbreiter. *Autonomous Jumping Microrobots*. Ph.D., University of California, Berkeley, December 2007.

[167] H. C. Bennet-Clark and G. M. Alder. The effect of air resistance on the jumping performance of insects. *The Journal of Experimental Biology*, 82:105–121, 1979.

[168] D. J. Bell, T. J. Lu, N. A. Fleck, and S. M. Spearing. MEMS actuators and sensors: observations on their performance and selection for purpose. *Journal of Micromechanics and Microengineering*, 15(7):S153–S164, 2005.

[169] W. A. Churaman, L. J. Currano, C. J. Morris, J. E. Rajkowski, and S. Bergbreiter. The first launch of an autonomous thrust-driven microrobot using nanoporous energetic silicon. *Journal of Microelectromechanical Systems*, 21(1):198–205, 2012.

[170] W. Lindsay, D. Teasdale, V. Milanovic, K. S. J Pister, and C. Fernandez-Pello. Thrust and electrical power from solid propellant microrockets. In *IEEE International Conference on Micro Electro Mechanical Systems*, pages 606–610, Interlaken, Switzerland, January 2001.

[171] M. Kovac, M. Fuchs, A. Guignard, J. C. Zufferey, and D. Floreano. A miniature 7g jumping robot. In *IEEE International Conference on Robotics and Automation*, pages 373–378, Pasadena, CA, USA, May 2008.

[172] H. Tsukagoshi, M. Sasaki, A. Kitagawa, and T. Tanaka. Design of a higher jumping rescue robot with the optimized pneumatic drive. In *IEEE International Conference on Robotics and Automation*, pages 1276–1283, Barcelona, Spain, April 2005.

[173] J. German. Hop to it: Sandia hoppers leapfrog conventional wisdom about robot mobility. http://www.sandia.gov/media/NewsRel/NR2000/hoppers.htm, June 2012.

[174] S. A. Stoeter and N. Papanikolopoulos. Kinematic motion model for jumping scout robots. *IEEE Transactions on Robotics*, 22(2):397–402, 2006.

[175] M. Karpelson, G. Y. Wei, and R. J. Wood. A review of actuation and power electronics options for flapping-wing robotic insects. In *IEEE International Conference on Robotics and Automation*, pages 779–786, Pasadena, CA, USA, May 2008.

[176] K. Hoffman and R. J. Wood. Myriapod-like ambulation of a segmented microrobot. *Autonomous Robots*, 31(1):103–114, 2011.

[177] R. Yeh, S. Hollar, and K. S. J. Pister. Single mask, large force, and large displacement electrostatic linear inchworm motors. *Journal of Microelectromechanical Systems*, 11(4):330–336, 2002.

[178] I. Penskiy, A. P. Gerratt, and S. Bergbreiter. Efficient electrostatic inchworm motors with simple control and high force density. In *International Conference on Solid-State Sensors, Actuators, and Microsystems (Transducers)*, pages 2438–2441, Beijing, China, June 2011.

[179] J. Burdick and P. Fiorini. Minimalist jumping robots for celestial exploration. *The International Journal of Robotics Research*, 22(78):653–674, 2003.

[180] P. Braunig and M. Burrows. Neurons controlling jumping in froghopper insects. *The Journal of Neurolophysiology*, 507(1):1065–1075, 2008.

[181] M. Burrows. Morphology and action of the hind leg joints controlling jumping in froghopper insect. *Journal of Experimental Biology*, 209:4622–4637, 2006.

[182] M. A. Erismis, H. P. Neves, R. Puers, and C. Van Hoof. A low-voltage large-displacement large-force inchworm actuator. *Journal of Microelectromechanical Systems*, 17(6):1294–1301, 2008.

[183] E. Sarajlic, C. Yamahata, E. Berenschot, N. Tas, H. Fujita, and G. Krijnen. High-performance shuffle motor fabricated by vertical trench isolation technology. *Micromachines*, 1(2):48–67, 2010.

[184] M. P. de Boer, D. L. Luck, W. R. Ashurst, R. Maboudian, A. D. Corwin, J. A. Walraven, and J. M Redmond. High performance surface micromachined inchworm actuator. *Journal of Microelectromechanical Systems*, 13(1):63–74, 2004.

[185] M. Kovac, M. Schlegel, J.-C. Zufferey, and D. Floreano. A miniature jumping robot with self-recovery capabilities. In *IEEE/RSJ International Conference on Intelligent Robots and Systems*, pages 583–588, St. Louis, MO, USA, October 2009.

[186] M. Noh, S.-W. Kim, S. An, J.-S. Koh, and K.-J. Cho. Flea-inspired catapult mechanism for miniature jumping robots. *IEEE Transactions on Robotics*, 28(5):1007–1018, 2012.

[187] M. Kovac, W. Hraiz, O. Fauria, J.-C. Zufferey, and D. Floreano. The EPFL jumpglider: A hybrid jumping and gliding robot with rigid or folding wings. In *IEEE International Conference on Robotics and Biomimetics*, pages 1503–1508, Phuket, Thailand, December 2011.

[188] I. Penskiy and S. Bergbreiter. Optimized electrostatic inchworm motors using a flexible driving arm. *Journal of Micromechanics and Microengineering*, 23(1):015018, 2013.

[189] J. Li, Q. X. Zhang, A. Q. Liu, W. L. Goh, and J. Ahn. Technique for preventing stiction and notching effect on silicon-on-insulator microstructure. *Journal of Vacuum Science & Technology B: Microelectronics and Nanometer Structures*, 21(6):2530–2539, 2003.